Swansea University E-Theses

Non-zero temperature charmonium potentials from the lattice.

Evans, P. Wynne M

How to cite:

Evans, P. Wynne M (2014) *Non-zero temperature charmonium potentials from the lattice..* thesis, Swansea University.
http://cronfa.swan.ac.uk/Record/cronfa42456

Use policy:

This item is brought to you by Swansea University. Any person downloading material is agreeing to abide by the terms of the repository licence: copies of full text items may be used or reproduced in any format or medium, without prior permission for personal research or study, educational or non-commercial purposes only. The copyright for any work remains with the original author unless otherwise specified. The full-text must not be sold in any format or medium without the formal permission of the copyright holder. Permission for multiple reproductions should be obtained from the original author.

Authors are personally responsible for adhering to copyright and publisher restrictions when uploading content to the repository.

Please link to the metadata record in the Swansea University repository, Cronfa (link given in the citation reference above.)

http://www.swansea.ac.uk/library/researchsupport/ris-support/

Swansea University
Prifysgol Abertawe

Non-Zero Temperature Charmonium Potentials
from the Lattice

P. Wynne M. Evans

Submitted to Swansea University in fulfilment
of the requirements for the degree of Doctor of Philosophy

2014

ProQuest Number: 10798164

All rights reserved

INFORMATION TO ALL USERS
The quality of this reproduction is dependent upon the quality of the copy submitted.

In the unlikely event that the author did not send a complete manuscript
and there are missing pages, these will be noted. Also, if material had to be removed,
a note will indicate the deletion.

ProQuest 10798164

Published by ProQuest LLC (2018). Copyright of the Dissertation is held by the Author.

All rights reserved.
This work is protected against unauthorized copying under Title 17, United States Code
Microform Edition © ProQuest LLC.

ProQuest LLC.
789 East Eisenhower Parkway
P.O. Box 1346
Ann Arbor, MI 48106 – 1346

SWANSEA
LIBRARY
UNIVERSITY

Abstract

A reliable calculation of the charmonium potential at non-zero temperature from first principles is required as part of a wider effort to understand the phase transition of hadronic matter to quark-gluon plasma at high temperature. The interquark potential inside hot matter produced in heavy ion collisions can not be measured directly. Therefore the precise role of the interquark potential in quark-gluon plasma formation can currently only be determined through a reliable theoretical calculation. In this thesis charmonium potentials are obtained from dynamical lattice simulations of quantum chromodynamics by analysing correlators using two different approaches: i) conventional fitting — correlators are fitted in the conventional manner familiar from hadron spectroscopy on the lattice; ii) the HAL QCD time-dependent method — a novel technique borrowed from nuclear physics is used to derive an expression for the potential directly in terms of the correlators.

Recent lattice QCD studies relevant to the charmonium potential fall into two categories: i) non-zero temperature studies of the static quark potential; ii) zero temperature studies with physical charm masses. The results presented in this thesis are novel because they are from a study of the charmonium potential using *physical* charm masses at *non-zero* temperature.

The charmonium potential obtained from conventional fitting is found to be temperature dependent, as the temperature increases, the potential flattens. However the method suffers from certain reliability issues. The time-dependent method is found to be more suitable than conventional fitting for studying the interquark potential at high temperature. Using the time-dependent method the charmonium potential between $0.76\mathrm{T_C}$ and $1.09\mathrm{T_C}$ is found to be temperature dependent. The result is reliable and shows the potential flattening as the temperature increases, which is consistent with the expectation that at high temperature the interquark potential becomes colour-Debye screened. Extracting the potential from temperatures higher than $1.09\mathrm{T_C}$ would have led to unreliable results, but this limit is specific to the configurations used and not the method itself. The study shows that if configurations are generated with the time-dependent method in mind, then it can be used to extract the charmonium potential at temperatures higher than $1.09\mathrm{T_C}$.

Declarations

This work has not previously been accepted and is not being concurrently submitted for any degree.

Under the supervision of Prof. Chris Allton I have produced this thesis through my endeavours alone. Sources are acknowledged explicitly by references linking to an appended bibliography.

I give consent for my thesis to be available for photocopying and inter-library loan, and for the title and summary to be made available to outside organizations.

Signed: ....

Date: ....26th.....September.....2014..

Contents

1 Introduction 1

2 Hot Matter 3

2.1 QCD . . . 3
2.2 States of Matter in QCD . . . 7
2.3 Theoretical Approaches to QCD . . . 11
2.4 Relativistic Heavy Ion Collisions . . . 12
2.5 Heavy Quarkonium Suppression . . . 17
2.6 Summary . . . 18

3 Lattice QCD 19

3.1 Lattice Gauge Theory . . . 19
3.2 Monte Carlo Importance Sampling . . . 19
3.3 Formalism . . . 20
3.4 Hadron Spectroscopy . . . 24
3.5 Quenched vs. Dynamical Simulations . . . 26
3.6 Quark Sources . . . 28
3.7 Smearing . . . 29
3.8 Gauge Fixing . . . 30
3.9 Non-Zero Temperature . . . 31
3.10 Anisotropic Lattices . . . 33

4 Conventional Fitting Approach 35

4.1 Nambu-Bethe-Salpeter Wave Functions . . . 35
4.2 Reverse-Engineering the Potential . . . 36
4.3 S-Waves . . . 38
4.4 $N_f = 2$ Simulation Details . . . 39
4.5 Results . . . 41

4.6 Conclusions 53

5 HAL QCD Time-Dependent Approach **57**
5.1 HAL QCD Time-Dependent Method 57
5.2 Accounting for the Backward-Mover 59
5.3 Momentum Space Propagators 60
5.4 $N_f = 2$ Results 62
5.5 $N_f = 2 + 1$ Simulation Details 73
5.6 $N_f = 2 + 1$ Results 75
5.7 Conclusions 90

6 Conclusion **93**

A $N_f = 2$ Spin-Independent Time-Slice Potentials **97**

B $N_f = 2 + 1$ Spin-Independent Time-Slice Potentials **101**

C $N_f = 2 + 1$ Spin-Independent Potential Data **107**

Acknowledgements

I would like to thank: first and foremost my supervisor, Prof. Chris Allton, for teaching, supporting and guiding me throughout my Ph.D. studies; Prof. Simon Hands, Prof. Gert Aarts, and Prof. Biagio Lucini, for their approachability and teaching; my collaborators, Dr. Jonivar Skullerud and Dr. Pietro Giudice, for always answering my questions; Dr. Maurizio Piai, for abating my doubts and fears; the STFC, for providing financial support; the Welsh Livery Guild, for presenting me with an academic travel scholarship; Balint Joó and Robert Edwards, for hosting my academic visit to Jefferson Lab; Bielefeld University Theoretical HEP Group, for giving me the opportunity to experience another interesting department; HPC Wales, UKQCD, and DiRAC, for providing computing resources; and last but not least everyone who spent time on the 5th and 6th floors of Vivian Tower between 2010 and 2014, for providing a stimulating environment in which to study.

List of Figures

2.1 QCD vs. QED Coupling Strength 6
2.2 QCD Phase Diagram 8
2.3 Critical Behaviour in QCD 8
2.4 Temperature vs. Age of the Universe 10
2.5 Heavy Ion Collision 14
2.6 Elliptical Flow 14

3.1 Lattice Formalism 21
3.2 Meson Correlator 25
3.3 Polyakov Loop Order Parameter 33

4.1 Schematic Diagram of $\mathcal{P}^{(2)}_{ss'}$ 40
4.2 Gaussian Smearing Parameter Comparison - n_σ Scan 42
4.3 Gaussian Smearing Parameter Comparison - σ Scan 43
4.4 $1.05T_{\mathrm{C}}$ Extended-Extended Correlators 43
4.5 $1.05T_{\mathrm{C}}$ Local-Extended Correlators 44
4.6 Eight-Parameter Fit of $1.05T_{\mathrm{C}}$ Extended-Extended Correlators 45
4.7 $1.05T_{\mathrm{C}}$ Local-Local Effective Mass Plot 47
4.8 $1.05T_{\mathrm{C}}$ Pseudoscalar and Vector Wave Functions 48
4.9 Pseudoscalar Wave Function 0.42–$2.09T_{\mathrm{C}}$ 49
4.10 Vector Wave Function 0.42–$2.09T_{\mathrm{C}}$ 49
4.11 Pseudoscalar Wave Function 0.42–$2.09T_{\mathrm{C}}$ 50
4.12 Vector Wave Function 0.42–$2.09T_{\mathrm{C}}$ 50
4.13 Pseudoscalar Wave Function 0.42–$2.09T_{\mathrm{C}}$ 51
4.14 Vector Wave Function 0.42–$2.09T_{\mathrm{C}}$ 51
4.15 Spin-Independent Potential 0.42–$2.09T_{\mathrm{C}}$ 52
4.16 Shifted Spin-Independent Potentials 0.42–$2.09T_{\mathrm{C}}$ 53
4.17 Spin-Dependent Potentials 0.42–$2.09T_{\mathrm{C}}$ 54

4.18 Shifted Spin-Dependent Potentials 0.42–2.09T_C 54

5.1 1.05T_C Pseudoscalar Time-Slice Potential without Substitute Temporal Term 63
5.2 1.05T_C Pseudoscalar Time-Slice Spatial Derivative Term 64
5.3 1.05T_C Pseudoscalar Time-Slice Temporal Derivative Term 64
5.4 1.05T_C Pseudoscalar Time-Slice Substitute Temporal Term 65
5.5 1.05T_C Pseudoscalar Time-Slice Potential 65
5.6 1.05T_C Vector Time-Slice Potential 66
5.7 1.05T_C Spin-Independent Time-Slice Potential 66
5.8 $N_f = 2$ Spin-Independent Potential 0.42–1.68T_C 69
5.9 $N_f = 2$ Shifted Spin-Independent Potential 0.42–1.68T_C 69
5.10 $N_f = 2$ Spin-Independent Potential with Systematic Error 0.42–1.68T_C 70
5.11 $N_f = 2$ Spin-Dependent Potential 0.42–1.68T_C 71
5.12 $N_f = 2$ Shifted Spin-Dependent Potential 0.42–1.68T_C 71
5.13 $N_f = 2$ Spin-Dependent Potential with Systematic Error 0.42–1.68T_C 72
5.14 Spin-Independent Potential - $N_f = 2$ Comparison 72
5.15 0.76T_C On-Axis Local-Extended Correlators 75
5.16 0.76T_C Face-Diagonal Local-Extended Correlators 76
5.17 0.76T_C Body-Diagonal Local-Extended Correlators 76
5.18 0.76T_C Pseudoscalar Potential $\tau = 15 - 19$ 78
5.19 0.76T_C Pseudoscalar Spatial Derivative Term $\tau = 15 - 19$ 78
5.20 0.76T_C Substitute Temporal Term $\tau = 15 - 19$ 79
5.21 Volume Effect Study 80
5.22 Volume Effect Study - Zoom 81
5.23 0.76T_C Pseudoscalar Time-Slice Potential 81
5.24 0.76T_C Vector Time-Slice Potential 82
5.25 0.76T_C Spin-Independent Time-Slice Potential 83
5.26 $N_f = 2 + 1$ Spin-Independent Potential '0'–1.09T_C 83
5.27 $N_f = 2 + 1$ Shifted Spin-Independent Potential '0'–1.09T_C 86
5.28 $N_f = 2+1$ Spin-Independent Potential with Systematic Error '0'–1.09T_C 86
5.29 $N_f = 2 + 1$ Spin-Dependent Potential '0'–1.09T_C 87
5.30 $N_f = 2 + 1$ Shifted Spin-Dependent Potential '0'–1.09T_C 88
5.31 $N_f = 2 + 1$ Spin-Dependent Potential with Systematic Error '0'–1.09T_C 88
5.32 Spin-Independent Potential - Time-Dependent Comparison 89
5.33 Spin-Independent Potential - Free Energy Comparison 90

A.1 $0.42T_C$ Spin-Independent Time-Slice Potential 98
A.2 $1.05T_C$ Spin-Independent Time-Slice Potential 98
A.3 $1.20T_C$ Spin-Independent Time-Slice Potential 99
A.4 $1.40T_C$ Spin-Independent Time-Slice Potential 99
A.5 $1.68T_C$ Spin-Independent Time-Slice Potential 100
A.6 $2.09T_C$ Spin-Independent Time-Slice Potential 100

B.1 Zero Temperature Spin-Independent Time-Slice Potential 102
B.2 $0.76T_C$ Spin-Independent Time-Slice Potential 102
B.3 $0.84T_C$ Spin-Independent Time-Slice Potential 103
B.4 $0.95T_C$ Spin-Independent Time-Slice Potential 103
B.5 $1.09T_C$ Spin-Independent Time-Slice Potential 104
B.6 $1.27T_C$ Spin-Independent Time-Slice Potential 104
B.7 $1.52T_C$ Spin-Independent Time-Slice Potential 105
B.8 $1.90T_C$ Spin-Independent Time-Slice Potential 105

List of Tables

4.1 J^{PC} Values in the Continuum and Representations of Spin under the Cubic Group 38
4.2 $N_f = 2$ Ensemble Details 41
4.3 Extended-Extended Pseudoscalar Fit Data 46
4.4 Extended-Extended Vector Fit Data 46

5.1 $N_f = 2$ Fitting Ranges 67
5.2 $N_f = 2 + 1$ Ensemble Details 74
5.3 $N_f = 2 + 1$ Fitting Ranges 82
5.4 String Tensions from $N_f = 2 + 1$ Spin-Independent Potentials 85

C.1 $N_f = 2 + 1$ Spin-Independent Potential Data 107

Chapter 1

Introduction

A reliable calculation of the charmonium potential at non-zero temperature from first-principles is required as part of a wider effort to understand the phase transition of hadronic matter to quark-gluon plasma (QGP) at high temperature. The QGP phase of quantum chromodynamics (QCD) has been studied extensively in heavy ion collisions and theoretical calculations. However a complete understanding of this phase is still some distance away. Experiments are hindered by uncertainties in the phenomenology of the QGP such as the equation of state, transport properties, and spectral features of hadrons. These quantities are required to model the pocket of QGP fleetingly produced in heavy ion collisions, as it expands and cools back into the hadronic phase. Without them event data collected by detectors can not be properly interpreted.

One of the quantities of interest is the interquark potential at temperatures above, below and throughout the cross-over region between the hadronic and QGP phases. Interest in the charmonium potential specifically was increased by a theoretical calculation suggesting J/ψ suppression could be used as a signal for QGP formation in heavy ion collisions. In [1] it is proposed that colour-Debye screening leads to a temperature dependent interquark potential and that this plays a pivotal role in QGP formation. However more recent studies of charmonium production using statistical [2, 3] and transport [4, 5] models, as well as a calculation of the imaginary part of the interquark potential [6], suggest that colour-Debye screening may not be the only important mechanism.

The interquark potential inside a pocket of QGP can not be measured experimentally. Consequently a reliable theoretical calculation of the interquark potential at non-zero temperature is the only way to determine the precise role of the interquark potential in QGP formation. Theoretical work on the interquark potential at high temperature includes early models [7] and perturbative QCD calculations [8–10], but due to the persistence of strong coupling effects at the deconfinement temperature a fully non-perturbative method is strictly essential. In this thesis Lattice QCD is the non-perturbative tool of choice. Recent relevant lattice QCD studies of the interquark potential fall into two categories: (i) non-zero temperature studies of the static quark potential [11–21] and (ii) zero temperature studies of the potential between quarks with finite masses [22,23]. The results presented in this thesis are from a study of the charmonium potential using *physical* charm quark masses at *non-zero* temperature, which is the first of its kind.

In this work the charmonium potential is obtained by analysing correlators using two different approaches. In Chapter 4 conventional fitting techniques are used to extract the charmonium wave function. Then in Chapter 5 a novel technique from nuclear physics is applied to the charmonium system. Both consider the non-relativistic limit to be appropriate for charmonium and employ the Schrödinger equation. To set the background for these studies we review, in Chapter 2, the salient features of QCD in the continuum, the phase transitions leading to QGP formation, and the heavy ion collisions being performed in the laboratory to learn more about hot matter. Then in Chapter 3 we introduce the lattice techniques key to obtaining the results. The thesis is concluded with Chapter 6 by summarising the results and discussing future avenues of research.

The publications: [24], [25], [26], [27] and [28], contain work presented in this thesis.

Chapter 2

Hot Matter

Experiment confirms that hadrons, such as the protons and neutrons of atomic nuclei, are composed of quarks. These constituent particles carry an additional degree of freedom to the electromagnetically and weakly interacting leptons, which is referred to as colour. Strong interactions, synonymous with colour dynamics, are mediated by colour-charged particles called gluons, which are responsible for binding quarks into hadrons — colour-neutral bound states composed of two ($q\bar{q}$) or three (qqq) quarks, mesons and baryons respectively. In high energy particle colliders, a large number of different hadrons can be produced. This 'particle zoo' was initially very confusing but is now explained by a single theory — QCD.

Independently as well as a part of the standard model of particle physics, QCD describes a wide range of experimentally observed interactions with great success. However a comprehensive understanding of strongly interacting matter can not be claimed until all the physical phenomena it exhibits, including its phase structure, are described in terms of the QCD Lagrangian.

2.1 QCD

QCD is a Yang-Mills theory with $SU(3)$ gauge group and six fermions, i.e. six quarks labelled, up (u), down (d), strange (s), charm (c), bottom (b) and top (t), also referred to as quark flavours. Its Lagrangian density is written,

$$\mathscr{L}_{\mathrm{QCD}} = \bar{q}^{i}_{f} \left(i \left(\gamma^{\mu} \mathcal{D}_{\mu} \right)^{ij} - m_{f} \delta^{ij} \right) q^{j}_{f} - \frac{1}{4} G^{a}_{\mu\nu} G^{\mu\nu}_{a}, \tag{2.1}$$

where $i = 1, 2, 3$, and $a = 1, \ldots, 8$, are colour indices, and f is the flavour index — these are often suppressed in subsequent equations to simplify the notation. The coloured quark and anti-quark fields, q_f and $\bar{q}_f$, transform in the fundamental representation and are coupled to the gluon fields, A^a_μ, which transform in the adjoint representation of $SU(3)$, through the gauge covariant derivative,

$$\mathcal{D}_\mu = \partial_\mu - ig\frac{\lambda_a}{2}A^a_\mu. \tag{2.2}$$

The Gell-Mann matrices, λ^a, are the generators of $SU(3)$ and satisfy,

$$[\lambda_a, \lambda_b] = f_{abc}\lambda_c, \tag{2.3}$$

where f_{abc} are the structure constants and g is the QCD coupling constant. The Dirac matrices, γ^μ, connect the spinor and vector representations of the Lorentz group, and $G^a_{\mu\nu}$ is the gluon field strength tensor given by,

$$G^a_{\mu\nu} = \partial_\mu A^a_\nu - \partial_\nu A^a_\mu + gf^{abc}A^b_\mu A^c_\nu. \tag{2.4}$$

Finally, m_f denotes the quark masses.

In addition to the inherent local $SU(3)$ gauge symmetry, the QCD Lagrangian has several classical symmetries [29]. The space-time symmetries of the theory are: Poincaré, charge-conjugation, parity and time-reversal symmetry. Also, if the u, d and s masses are considered light, and the c, b and t masses very heavy, such that they decouple, then the theory is approximately invariant under the scale transformations,

$$x^\mu \to \lambda x^\mu, \qquad q(x) \to \lambda^{3/2}q(\lambda x), \qquad A^a_\mu(x) \to \lambda A^a_\mu(\lambda x), \tag{2.5}$$

where $\lambda \in \mathbb{R}$.

The global quark symmetries of the theory are:

- $U(1)_B$ baryon number symmetry, corresponding to invariance under transformations of the type, $q \to \mathrm{e}^{i\alpha}q$, $\alpha \in \mathbb{R}$.

- $SU(3)_V$ vector symmetry, if the u, d and s masses are considered approximately equal the theory possesses an approximate invariance under the transformations,

$$\begin{pmatrix} u \\ d \\ s \end{pmatrix} \to U \begin{pmatrix} u \\ d \\ s \end{pmatrix}, \tag{2.6}$$

where $U \in SU(3)_V$.

- $SU(3)_L \times SU(3)_R$ chiral symmetry, if u, d and s quarks are also considered approximately massless there is an approximate invariance under the transformations,

$$\begin{pmatrix} u^{L,R} \\ d^{L,R} \\ s^{L,R} \end{pmatrix} \to U_{L,R} \begin{pmatrix} u^{L,R} \\ d^{L,R} \\ s^{L,R} \end{pmatrix}, \tag{2.7}$$

where $q^{L,R} = [(1 \mp \gamma_5)/2]q$. This is an invariance of the quark kinetic terms,

$$\bar{q}i\not{D}q = \bar{q}^L i\not{D}q^L + \bar{q}^R i\not{D}q^R \tag{2.8}$$

but not of the quark mass terms,

$$m_q\bar{q}q \equiv m_q\bar{q}^L q^R + m_q\bar{q}^R q^L, \tag{2.9}$$

where $U_{L,R} \in SU(3)_{L,R}$.

- $U(1)_A$ symmetry corresponding to the invariance,

$$q^L \to \mathrm{e}^{i\alpha}q^L, \qquad q^R \to \mathrm{e}^{-i\alpha}q^R. \tag{2.10}$$

There is also a pseudo global quark symmetry — $SU(3)_A$. $SU(3)_V$ is the subgroup of $SU(3)_L \times SU(3)_R$ corresponding to the set of transformations with $U_L = U_R$. The set of transformations orthogonal to these with $U_L = U_R^\dagger$, are labelled $SU(3)_A$ and referred to as the $SU(3)$ axial symmetry, even though they do not form a true group.

In the quantum theory the QCD vacuum becomes a polarizable medium. Consequently the effective charge measured for a particular coupling value is a function of the energy scale, μ, at which the measurement is made, meaning the approximate scale invariance of the classical theory is broken. To make a direct comparison with the fine structure constant of QED, it is conventional to consider an alternative definition of the QCD coupling,

$$\alpha_s(\mu) = \frac{g^2(\mu)}{4\pi}. \tag{2.11}$$

The relationship between α_s and μ is summarized by the β-function, which for the

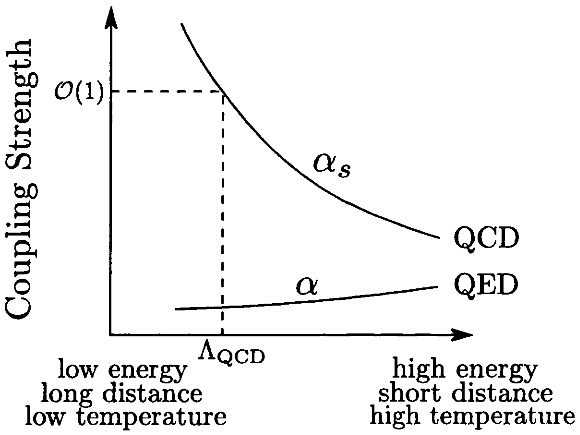

Figure 2.1: In contrast to QED, QCD is strongly coupled at low energies. This means non-perturbative methods are essential to study the low energy behaviour of QCD. Below a certain energy scale, $\Lambda_{\rm QCD}$, bound states of quarks form.

QCD coupling constant at three loops (in the $\overline{\rm MS}$ scheme) is,

$$\mu\frac{\partial\alpha_s}{\partial\mu} = 2\beta(\alpha_s) = -\frac{\beta_0}{2\pi}\alpha_s^2 - \frac{\beta_1}{4\pi^2}\alpha_s^3 - \frac{\beta_2}{64\pi^3}\alpha_s^4 - ..., \tag{2.12}$$

where,

$$\beta_0 = 11 - \frac{2}{3}N_f, \quad \beta_1 = 51 - \frac{19}{3}N_f, \quad \beta_2 = 2857 - \frac{5033}{9}N_f + \frac{325}{27}N_f^2, \tag{2.13}$$

and N_f is the number of active quark flavours.

The salient feature of the QCD β-function is its negative sign, which can be traced to the contribution from the self-interaction of the gluons, and thus the non-Abelian nature of the gauge group. Consequently the effective coupling becomes weaker at higher energies, or in other words, at high energies the theory exhibits asymptotic freedom [30]. At low energies the effective coupling becomes strong resulting in the confinement of colour charges. Figure 2.1 illustrates the behaviour of the coupling with energy. Since the QCD coupling runs with energy a corresponding dimensionful quantity, Λ_{QCD}, can be defined. In the $\overline{MS}$ scheme at an energy scale of M_Z (Z-boson mass) there are five active quark flavours (u, d, s, c, b) and $\Lambda_{QCD} \approx 217$MeV [31]. At low energies comparable to the masses of the lightest baryons, there are only three active quark flavours (u, d, s) and $\Lambda_{QCD} \approx 350$MeV. This value sets the scale at which the coupling becomes large and non-perturbative effects become important. It is also relative to this scale that the u, d and s quarks are considered light and why the chiral properties of the c, b and t quarks are not considered.

In the QCD vacuum, flavour chiral symmetry breaking occurs,

$$SU(3)_L \times SU(3)_R \to SU(3)_V, \tag{2.14}$$

for which the chiral condensate, $\langle \bar{q}q \rangle$, serves as an order parameter. The corresponding Goldstone bosons are the eight pseudoscalar mesons of the quark model [32–34]. The masses of these mesons can be obtained from chiral perturbation theory.

2.2 States of Matter in QCD

Hadrons require a volume of approximately, $V_h = (4\pi/3)r_h^3$ to exist, where the typical radius of a hadron, r_h, is about 1fm. Consequently, there is an upper limit to the density hadronic matter can take,

$$n_c \approx 1/V_h \approx 0.24 \text{ fm}^{-3}, \tag{2.15}$$

which is roughly 50% higher than the density found in nuclei under normal conditions. Furthermore this leads to a maximum temperature for hadronic matter [35]. Using natural units ($k_\mathrm{B} = 1$),

$$T_c \approx 1/r_h \approx 0.2 \text{ GeV}. \tag{2.16}$$

These arguments reveal that strongly interacting matter has a $T - \mu_B$ phase diagram, where T is the temperature and μ_B is the baryon number density, and that above a certain limiting curve in the $T - \mu_B$ plane hadronic matter can not exist. We are interested in using QCD to quantitatively investigate the fate of hadronic matter under extreme conditions, but can already make some qualitative remarks.

According to QCD, below the limiting curve in the $T - \mu_B$ plane hadrons are colour-neutral bound states of quarks, hence above the limiting curve we expect deconfinement into a medium consisting of coloured constituents — QGP [36]. We can picture the approximate phase diagram of QCD shown in Figure 2.2 by imagining the two distinct ways in which QGP can be formed:

i) Holding the density at zero and increasing the temperature produces quark-anti-quark pairs from the vacuum in greater and greater numbers until the

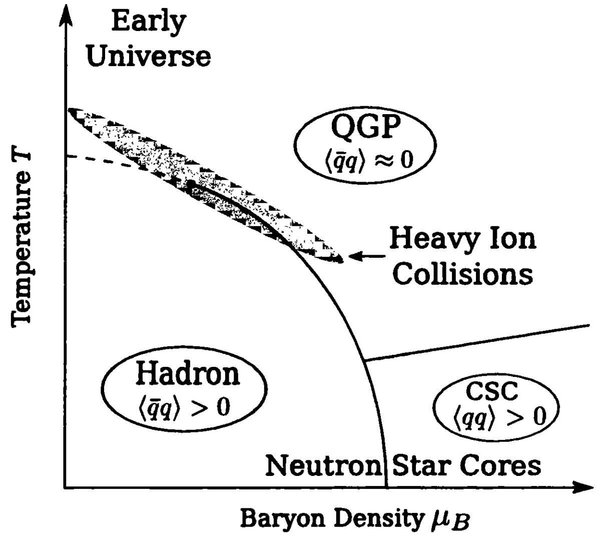
Early Universe
Temperature T
QGP
$\langle \bar{q}q \rangle \approx 0$
Heavy Ion Collisions
Hadron
$\langle \bar{q}q \rangle > 0$
CSC
$\langle qq \rangle > 0$
Neutron Star Cores
Baryon Density μ_B

Figure 2.2: A sketch of the QCD phase diagram. At low temperature and density, QCD is confining. Under extreme pressure and/or density QGP forms. At high density and low temperature a colour-superconducting (CSC) phase is expected. At high temperature and low density the transition to QGP, marked by a dash, represents the cross-over region; heavy ion collisions are probing roughly this region of phase space.

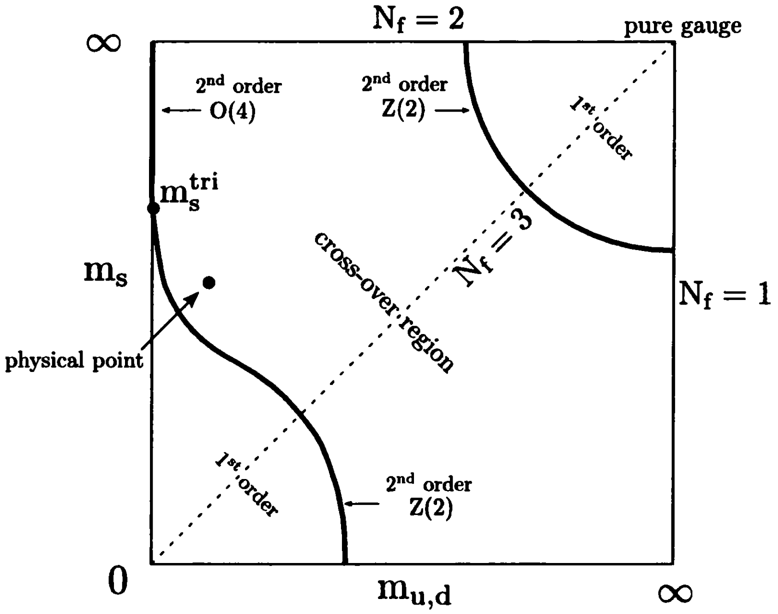
$N_f = 2$
pure gauge
∞
2^{nd} order
O(4)
2^{nd} order
Z(2)
1^{st} order
m_s^{tri}
cross-over region
$N_f = 3$
m_s
$N_f = 1$
physical point
1^{st} order
2^{nd} order
Z(2)
0
$m_{u,d}$
∞

Figure 2.3: Critical behaviour in QCD [37].

number density of hadrons is equal to the inverse of the typical hadron volume. At which point hadrons begin to overlap and the system dissolves into one of free quarks and gluons. We expect QGP formed in this manner to have an equal number of quarks and anti-quarks since it is formed by intense pair creation. We conclude the chiral condensate $\langle \bar{q}q \rangle$ can be used as an order parameter for this type of transition.

ii) Holding the temperature at zero and increasing the number density of hadronic matter results in QGP formation once n_c is reached, again at the point hadrons begin to overlap the relevant degrees of freedom become those of quarks and gluons not hadrons. At zero temperature only baryonic matter is present, this means the critical density is expected to be roughly the inverse of the typical baryon volume. Furthermore the QGP produced will be dominated by quarks suggesting $\langle qq \rangle$ is the relevant order parameter in a fixed gauge.

The nature of the phase transition to QGP has been given much attention. In the confined phase hadrons behave as if they are comprised of light quarks with constituent mass, $m_Q \approx 300\text{MeV}$. Conceptually we can think of the quarks as being 'dressed' with gluons at low temperature. As the temperature increases the coupling becomes weaker, the gluon dressing detaches and $m_Q \to m_q$, where m_q is the bare quark mass. For the up and down quarks $m_q \approx 0$, this suggests (approximate) chiral symmetry restoration corresponds to deconfinement and vice versa. Based on this reasoning chiral symmetry restoration and deconfinement are assumed to coincide at high temperature and vanishing baryon density. However at least one study suggests that they may occur at different critical temperatures [38]. Figure 2.3 maps the order of the QCD phase transition at $\mu_B = 0$ for different light quark masses, $m_{u,d,s}$:

- For $m_q \to \infty$ for all quark flavours pure $SU(3)$ gauge theory is recovered and deconfinement is marked by a first order phase transition corresponding to spontaneous Z_3 breaking [39,40].

- In the limit $m_q \to 0$ for all quark flavours a first order phase transition corresponding to chiral symmetry restoration is found [40,41].

- For m_q taking a value intermediate to the infinite and zero mass limits, there is no genuine phase transition only a cross-over region [40].

- For $m_{u,d} = 0$ and $m_s > m_s^{\text{tri}}$ the transition is of second order and assumed to be in the $O(4)$ universality class [41]. The second order limits of the first order regions appear to be in the Z_2 universality class [42]. At m_s^{tri} the two different continuous transitions meet with the first order transition [40, 43].

The important point to draw from Figure 2.3 and the studies from which it was formed is that the physical point corresponding to small u, d masses and larger s mass lies in the cross-over region. The implication for the interquark potential is that a sharp change corresponding to the critical temperature of a genuine phase transition is not expected.

The order of the QCD phase transition can also be investigated by analysing the Cosmic Microwave Background (CMB) radiation. For example if the universe underwent a genuine first order phase transition, domains of one phase would have formed within another. Although the QCD phase transition occurred much earlier in the history of the universe than many important phenomena, see Figure 2.4, evidence of domain walls should still be detectable in the CMB. A first order QCD phase transition would have resulted in a large amount of energy being released in the form of latent heat and major cosmological consequences.

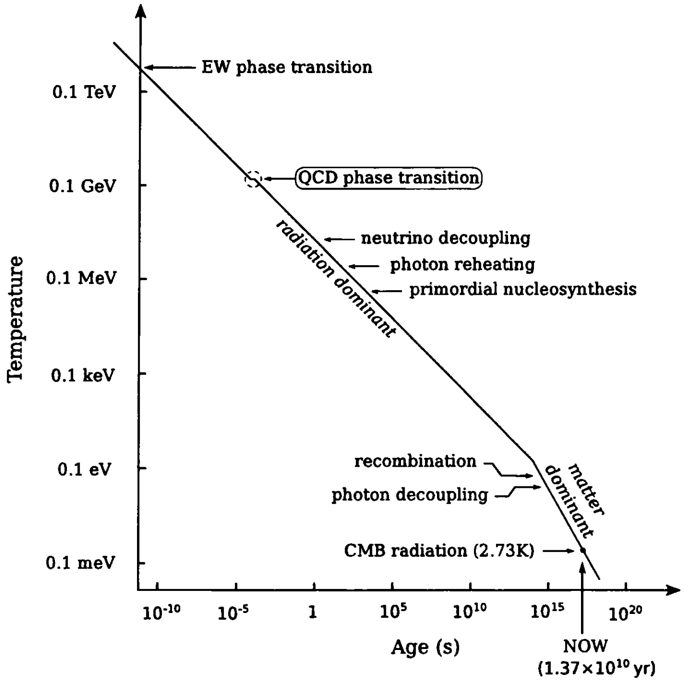

Figure 2.4: A plot showing the temperature versus age of the Universe, including the various phase transitions it is thought to have undergone [44].

The phase structure of QCD at high density and low temperature may be very rich. At high density where the coupling is weak and quark matter is abundant, the quark-quark interaction in certain colour channels is attractive leading to the formation of Cooper pairs. In analogy with BCS theory [45] the breaking of the local colour $SU(3)$ symmetry by the Cooper pair condensates results in a superconducting phase. The interesting feature of superconductivity in cold dense QCD is that, in addition to their Dirac degrees of freedom, quarks have colour and flavour meaning many different patterns of pairing are possible and hence a panoply of different superconducting phases is possible [46].

2.3 Theoretical Approaches to QCD

Mapping the phase diagram of QCD is of great scientific interest. The area has received continuous attention since the discovery of the strong interaction. However to date no single theoretical approach has been satisfactorily applied to all regions of the QCD phase diagram. The strongly coupled nature of QCD at energies below and around $\Lambda_{\rm QCD}$ means perturbation theory can not be employed to study phenomena such as deconfinement and QGP precisely, as a result several alternative approaches have been developed.

Potential models have been used to describe hadrons composed of charm and bottom quarks. If the motion of the valence quarks is much slower than the typical frequency of the gluon exchange between them, then a potential approach is justified. An example is the Cornell potential developed for charmonium [47–49],

$$V_{q\bar{q}} = -\frac{\kappa}{r} + \frac{r}{a^2}. \tag{2.17}$$

where κ is the Coulomb parameter and a^{-2} is proportional to the string tension. Inserting this potential into the Schrödinger equation approximates the charmonium spectrum remarkably well, but it is difficult to extend this approach to include relativistic effects since it is inherently non-relativistic.

The method of QCD sum rules [50,51] is an approach to QCD in which hadrons are represented by their interpolating quark currents. Short and long distance gluon interactions are separated within the framework of the operator product expansion (OPE) to give the correlation function of the quark currents. The method has been used to calculate hadron masses, couplings and electromagnetic properties with reasonable accuracy and can also be extended to non-zero temperature and density. However the method is limited by approximations in the OPE.

Gauge-gravity duality [52–55] has been used to investigate the phase structure of strongly coupled theories. The duality has a weak-strong nature and an extensive dictionary has been developed between quantities in the gravity theory and observables in the gauge theory. By performing calculations in the weak coupling regime of the gravity theory, where calculations are feasible, information on observables in the strongly coupled regime of the gauge theory can be attained. This approach has been used to show such theories possess first order and higher order phase transitions [56, 57]. The fundamental issue is that the gravity duals investigated so far are known not to be the dual of QCD. Furthermore, as Figure 2.3 demonstrates, the nature of the QCD phase transition has a strong dependence on the masses of the three lightest quarks requiring a deeper understanding between the gravity dual parameters and the gauge theory masses.

Lattice QCD, formulated in Section 3, has arguably provided the most significant non-perturbative results for QCD. However with regards to studying the QCD phase diagram it currently suffers from a severe limitation. To investigate non-zero density a chemical potential is introduced into the lattice action. The Euclidean path integral must then be performed over an exponential term with an imaginary exponent. The oscillatory nature of this term causes the value of observables to fluctuate wildly, and the method is said to suffer from a 'sign problem'. Promising steps are being taken towards solving the sign problem for lattice QCD [58–61], but a solution has not yet been reached. In this thesis we are hence taking the path of least resistance — lattice QCD at high temperature and zero chemical potential is readily computable.

2.4 Relativistic Heavy Ion Collisions

Interest in high temperature QCD began to grow about three decades ago mainly due to the idea that ultra relativistic nucleus-nucleus collisions would produce pockets of QGP which survive long enough to test the predictions of QCD. Over the last two decades experimentalists have successfully probed QCD by performing heavy ion collisions with centre of mass energies ranging from giga- to tera-electronvolts (GeV-TeV). In these collisions, heavy atoms are stripped of their electrons, accelerated to high energies and collided with a heavy target or opposing beam. Whether QGP is formed in these collisions is mainly a function of the centre of mass energy of collisions. Very high energies probe the high temperature low baryon density region of the QCD phase diagram, while moderate energies probe lower temperatures and larger baryon density.

A pocket of QGP formed in a collision has the following time evolution [44]:

i) Immediately after collision there is a short pre-equilibrium phase, which is a period of immense entropy production, the hadrons interact, multiply and the relevant degrees of freedom become those of quarks and gluons rather than hadrons.

ii) The medium reaches local thermal equilibrium, soon after the system of free quarks and gluons begins to expand.

iii) Under expansion the medium cools, below a certain temperature, T_{C}, confinement sets in and hadronization occurs.

iv) As the medium cools further inelastic collisions cease, this is known as chemical freeze-out.

v) The particles present at chemical freeze-out continue to interact until the system expands to the point of kinetic freeze-out, whereafter the collision reactants are overwhelmingly likely to interact next with the detector rather than each other.

The non-equilibrium non-Abelian system in i) is difficult to model, as a result this period is poorly understood. However the most interesting physics occurs during ii) and iii). If it is considered a perfect liquid, then relativistic hydrodynamics can be used to model the evolution of the QGP pocket since the only information required is the local energy density and pressure, along with the conservation of the energy-momentum tensor and baryon number. If it can not be approximated as a perfect liquid extra information is needed such as the viscosity and heat conductivity [44].

Another important aspect of collisions is the centrality. Figure 2.5 is a schematic diagram showing the geometry of a heavy ion collision. The degree to which colliding nuclei overlap (or are central) on collision is parameterized by the impact parameter, b. When $b > 2R$, 'distant' collisions due to electromagnetic forces occur, which can cause the nuclei to break up, but do not result in the formation of a strongly interacting thermal medium. For $b < 2R$ peripheral collisions lead to a sudden rise in inelastic reactions due to the strong force. Central collisions occur when $b = 0$. The centrality of collisions can not be measured directly but is directly proportional to the multiplicity, which itself is proportional to the ratio of participants and spectators. The Glauber model is used widely to analyse nuclear reaction cross-sections. It can be used to determine the number of participant nucleons and hence the centrality of collisions [62].

The centrality of collisions can be correlated with certain emission patterns. Peripheral collisions result in an almond shaped participant region. The analysis

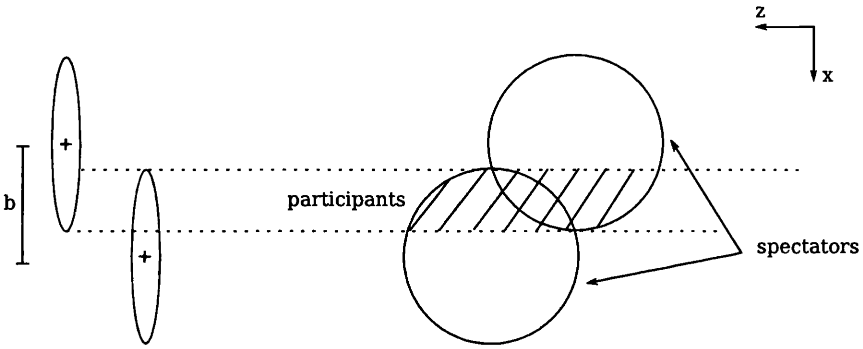

Figure 2.5: Schematic diagram of a heavy ion collision. The impact parameter, b, parameterizes the centrality of a collision. The radius of the nuclcon is Lorentz contracted in the direction of travel, giving the nuclei a pancake shape on collision. Nucleons outside the collision zone are called spectators, those inside participants.

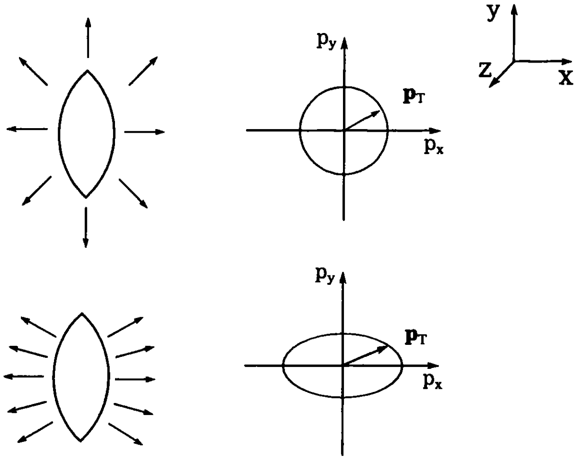

Figure 2.6: The transverse momentum, $\mathbf{p}_\mathrm{T}$, is the component of momentum detected perpendicular to the particle beams. The top set of diagrams illustrates the scenario in which the size of the system, R, is much larger than the mean-free-path of particles, l, the resulting pressure gradient and $\mathbf{p}_\mathrm{T}$ distribution is approximately isotropic. The bottom set of diagrams illustrates the scenario in which l is comparable to R, leading to a pressure gradient and $\mathbf{p}_T$ distribution that are anisotropic.

of these types of collision has been particularly instrumental in determining the liquid-like rather than gas-like nature of QGP. The almond shape of the participant region means the emission pattern of particles emerging from the cooling thermal medium is influenced by the ratio of the mean-free-path of particles, l, and the size of system, R. If $l \ll R$ the pressure gradient is steep and anisotropic with a profile dictated by the shape and orientation of the participant region, see Figure 2.6. The anisotropic pressure gradient gives rise to a collective flow of particles which results in an emission pattern characterized by an elliptical azimuthal distribution [44]. This phenomenon is referred to as elliptical flow. If l is not much less than R the pressure gradient is moderate in all directions and the emission pattern is isotropic.

Other than elliptical flow there are several methods that can be used to study a sample of hot dense strongly interacting matter:

- hadron radiation
- electromagnetic radiation
- jet quenching
- heavy quarkonium suppression

Hadron radiation refers to the emission of hadrons comprised of light quarks (u, d, s) from the surface that defines the boundary between the hot matter of the participant region and the surrounding vacuum. If QGP is formed then the temperature of this surface is equal to the deconfinement temperature and is independent of how hot the medium initially was or continues to be. Consequently studying soft hadron production in heavy ion collisions provides information about the hadronization process but not QGP.

Electromagnetic radiation refers to photons and dileptons (e^+e^- or $\mu^+\mu^-$) emitted from the medium of hot strongly interacting matter through quark and gluon interactions and quark–anti-quark annihilation. Once formed the photons and leptons leave the medium without any further interaction since they do not interact strongly. As a result they can provide information about any point in the medium including those where QGP is present. However the utility of photon and dilepton production in heavy ion collisions with regards to studying QGP is hindered by the fact that production occurs throughout the collision and at all points — the task is to characterize the electromagnetic radiation typical of QGP.

Jet quenching refers to the inference of a missing particle shower during the back-to-back scattering of two high energy quarks in a heavy ion collision. In a proton-proton collision such a scattering is detected in the form of two jets — the decay products of the high energy quarks — with trajectories in opposite directions. In a heavy ion collision the same interaction occurs except one jet trajectory is away from the hot medium and consequently observed, while the other is into the medium and undetectable once it is lost in the the mêlée of particles.

Heavy quarkonium suppression is particularly relevant to this thesis, as such it is discussed in detail in Section 2.5.

Heavy ion collisions were first performed at Brookhaven National Laboratory (BNL) near New York, and the European Centre for Nuclear Research (CERN) near Geneva in 1986. In these experiments light nuclei such as oxygen and sulphur were fired at fixed heavy nuclei such as gold or uranium. Evidence of J/ψ suppression was found in these early experiments [63], which paved the way for future upgrades. By 1995 lead-lead and gold-gold fixed target collisions were being performed by BNL-AGS and CERN-SPS with centre of mass energies of 5GeV and 20GeV respectively. Between 1995 and 2000 [64] the NA50 collaboration responsible for investigating J/ψ yields from the CERN-SPS experiment repeatedly found evidence of J/ψ suppression increasing with the centrality of collisions [65]. The first dedicated heavy ion collider, the Relativistic Heavy Ion Collider (RHIC), was constructed at BNL and went online in 2000. A large amount of data relevant to high temperature QCD has been collected by RHIC. Prudent analysis has provided interesting results for elliptical flow, jet quenching, colour glass condensate saturation, particle ratios and many other aspects [66–69]. In 2010 RHIC physicists confirmed that temperatures of 345 MeV had been achieved in gold ion collisions, and that at these temperatures hadronic matter became deconfined, forming a QGP. For the most part this result was expected, however, the viscosity of the QGP was more similar to that of a liquid rather than a gas, contrary to expectation [66,67]. The second operational heavy ion collider is the Large Hadron Collider (LHC) at CERN. The LHC is better known for being a proton-proton collider but for one month a year it performs heavy ion collisions. ALICE is the specialist detector constructed to collect event data from lead-lead and proton-lead collisions, but important results have also been captured by CMS and ATLAS. In 2011 the ALICE collaboration published results from lead-lead collisions [70–74]. They presented measurements for the size of the QGP system created in lead-lead collisions at a centre of mass energy of 2.76 TeV. They also confirmed that hot QCD matter created in lead-lead collisions behaves like a liquid described well by hydrodynamics. Later J/ψ suppression was detected and studied in more detail [75] as well as jet quenching [76, 77]. Furthermore heavy quarkonium suppression was confirmed by the CMS collaboration as a general feature of heavy ion collisions, with Υ suppression observed in bottomonium yields [78]. The QGP pockets created at the LHC are larger and hotter than those created at RHIC. The energy of collisions at both sites will increase in the future. As the energy increases heavy quarks are produced more frequently both in the initial collision and the resulting thermal medium. As a result heavy quark processes and quantities such as the charmonium potential will become even more relevant to QGP phenomenology. There are plans to build a heavy ion collider to investigate higher densities of QGP. The Facility for Antiproton and Ion Research (FAIR) collider, to be sited at GSI in Germany, will have larger luminosity than RHIC and the LHC.

2.5 Heavy Quarkonium Suppression

Quarkonia are mesons made from a quark and its anti-particle. e.g. $c\bar{c}, b\bar{b}$. The heavy quarkonia are of particular interest because charmonium and bottomonium states have large binding energies and correspondingly small binding radii, r_{Q}. The ground states J/ψ and Υ have binding energies of roughly 0.6 GeV and 1.2 GeV, with binding radii of 0.2fm and 0.1fm respectively. These binding radii make charmonium and bottomonium states susceptible to suppression at temperatures where QGP is expected to exist.

According to QCD, QGP consists of free colour-charged quarks and gluons. By analogy with Debye screening in an electromagnetic plasma, free colour-charges are expected to screen each other, an effect referred to as colour-Debye screening. According to this interpretation, the interquark potential in a QGP will be modified from a potential built from a Coulomb and linear term, like the Cornell potential in (2.17), to a colour-Debye screened potential,

$$V_{q\bar{q}} = -\frac{\kappa}{r} + \frac{r}{a^2} \to -\frac{1}{r}\mathrm{e}^{-r/r_{\mathrm{D}}(T)}. \tag{2.18}$$

The Debye radius, r_{D}, parameterizes the density of colour charges. As the temperature increases, r_{D} decreases. When $r_{\mathrm{D}} \gg r_{\mathrm{Q}}$ a bound state is not affected by the medium. However once $r_{\mathrm{D}} \ll r_{\mathrm{Q}}$ the bound state dissociates.

Heavy quarkonium suppression was first proposed as a QGP signal in the context of J/ψ suppression [1]. Quantitative calculations suggested a temperature of approximately 300MeV is high enough to suppress the creation of charmonium. In the potential picture this corresponds to $r_{\mathrm{D}}(300\mathrm{MeV}) < r_{J/\psi}$. Higher excited states of charmonium are less tightly bound with correspondingly larger binding radii: χ_c(1P) - 0.3fm, ψ'(2S) - 0.4fm [40], but still significantly smaller than the radii of light hadrons. Based on the temperature dependence of r_{D} we conclude the different charmonium states dissociate at different temperatures, offering a way to determine the temperature of QGP samples via analysis of the charmonium spectrum. An analogous analysis is possible for bottomonium states.

Experimentally J/ψ suppression is observed as a decrease in dilepton radiation at energies corresponding to the J/ψ mass. The decrease seen in nucleus-nucleus collisions is measured relative to proton-proton or proton-nucleus collisions. In practice the observation of J/ψ suppression is not straightforward. Measurements are complicated by the process of recombination, which refers to the binding of charm quarks produced by hard processes in the initial collision — free due to the thermal medium — with charm quarks produced thermally at a later stage in the collision. At high energies J/ψ recombination can mask or even overcome suppression to yield a J/ψ enhancement.

2.6 Summary

Experiment confirms that at high temperature hadrons deconfine into a medium of free quarks and gluons. This quark-gluon plasma behaves almost like a perfect liquid and can be described well using hydrodynamic equations. The heavy ion collisions which probe QCD at high temperature are set to move firmly into the TeV scale. At these energies hard processes and heavy quark production are important. Consequently a reliable calculation of the charmonium potential will be required to interpret event data.

Lattice QCD is the only fully non-perturbative and model-independent approach to QCD. Therefore it is the best tool available for studying high temperature zero density QCD, and as such the best approach to calculating the charmonium potential. The proceeding chapter reviews the main lattice techniques used in this work.

Chapter 3

Lattice QCD

Formulating QCD as a lattice gauge theory permits phenomena which are analytically intractable due to their non-perturbative nature, such as confinement and quark-gluon plasma formation, to be investigated using numerical methods.

3.1 Lattice Gauge Theory

Lattice gauge theories are formulated in Euclidean space-time on a hypercubic lattice of spacing a. The formulation of gauge theories in discrete rather than continuous space-time introduces a momentum cut-off at order $1/a$, equipping lattice gauge theories with a built-in UV regularizer. The finite size of the hypercubic lattice provides a complementary IR regularizer. Consequently, lattice gauge theories are mathematically well-defined.

By considering only a finite number of lattice points arranged in a hypercube, and imposing periodic boundary conditions, the system is reduced to a finite number of degrees of freedom. This allows the system to be simulated in a finite time by a computer. Whether the system is simulated exactly or approximately depends on the number of lattice points considered. At a certain point, exact simulation takes an impractically large amount of computer time and Monte Carlo importance sampling must be employed.

3.2 Monte Carlo Importance Sampling

The expectation value of an observable, O, in QCD is equal to the path integral over the measure, $\mathscr{D}[q, \bar{q}, A]$, representing all possible gluon and and quark field configurations,

$$\langle O\rangle = \frac{1}{Z}\int \mathscr{D}[q,\bar{q},A]e^{iS_{\mathrm{QCD}}[q,\bar{q},A]}O[q,\bar{q},A], \tag{3.1}$$

with,

$$S_{\mathrm{QCD}}[q,\bar{q},A] = \int d^4x\ \mathscr{L}_{\mathrm{QCD}}, \tag{3.2}$$

and,

$$Z = \int \mathscr{D}[q,\bar{q},A]e^{iS_{\mathrm{QCD}}[q,\bar{q},A]}, \tag{3.3}$$

where S_{QCD} is the QCD action, $\mathscr{L}_{\mathrm{QCD}}$ is defined in (2.1), the metric signature of d^4x is that of Minkowski space, and A, q, and $\bar{q}$ are the gluon, quark and anti-quark fields respectively.

To perform the path integral over all possible field configurations quickly becomes too time-consuming for lattices with more than a few sites in each dimension. We are left with no choice but to approximate the integral. This is done using importance sampling. To use this we Wick rotate to Euclidean space-time, $t \to -i\tau$, so the exponent of (3.1) becomes positive definite,

$$e^{iS_{\mathrm{QCD}}} \to e^{-S_{\mathrm{LQCD}}} \in \{0,1\}, \tag{3.4}$$

allowing it to be interpreted as a probability measure. Given this, observables can be calculated by replacing the right-hand side of (3.1) with the average value of the observable taken over an ensemble of configurations sampled with probability $e^{-S_{\mathrm{LQCD}}}$,

$$\langle O\rangle = \frac{1}{N}\sum_{U_n} O[U_n], \tag{3.5}$$

where N is the number of configurations, U_n, in the ensemble. Great care must be taken to ensure that the finite number of configurations selected to form an ensemble is a true representation of the complete configuration space defined by the measure — $\mathscr{D}[q,\bar{q},A]$.

3.3 Formalism

To study QCD on the lattice we work with a Euclidean metric and discretize space-time over a finite number points arranged in a hypercubic lattice, Λ, with spacing a,

$$\Lambda = \{x \in \mathbb{R}^4 \mid x_{1,2,3}/a = 0,1,2,\dots,N_s-1,\ ;\ \tau/a = 0,1,2,\dots,N_\tau-1\}. \tag{3.6}$$

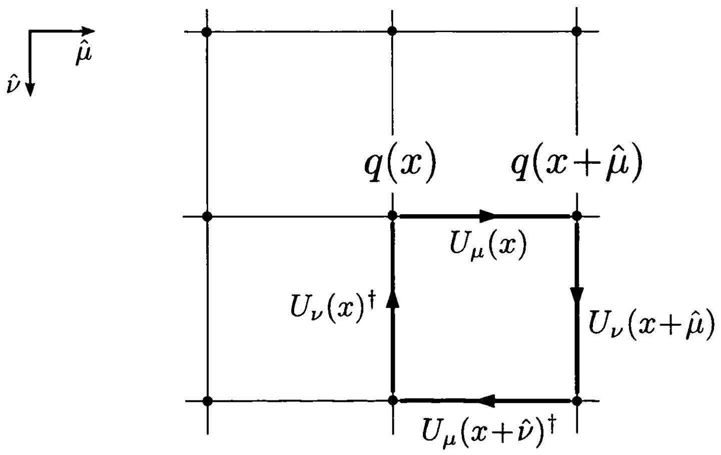

Figure 3.1: A schematic diagram depicting the typical formalism of lattice gauge theories. The fermions, q, reside on the lattice sites, while the link variables, U_μ, connect neighbouring sites with orientation μ.

A quark field, $q^i_\alpha(x)$, is associated with the lattice sites, as shown in Figure 3.1, but there appears without colour, i, and Dirac, α, indices to simplify the notation. The next step is to discretize $\mathscr{L}_{\mathrm{QCD}}$ shown in (2.1). To maintain gauge-invariance on the lattice the gauge field degrees of freedom are represented using the link variable,

$$U_\mu(x) = e^{iaA_\mu(x)}, \tag{3.7}$$

which connects the sites x and $x+\mu$, as seen in Figure 3.1. For QCD the link variables are elements of the $SU(3)$ group, in contrast to the continuum gauge fields, A of (3.1), and the lattice gauge fields, $A_\mu(x)$ of (3.7), which are elements of the $\mathfrak{su}(3)$ Lie algebra. The link variable has a counterpart in the continuum: the path-ordered exponential integral of the gauge fields, A, along some curve between x and y is the gauge transporter,

$$G(x,y) = P\exp\left(i\int_x^y A\cdot ds\right). \tag{3.8}$$

$G(x,y)$ is known as a Wilson line, or Wilson loop if the path, C_{xy}, is closed. Under a gauge transformation Ω, $G(x,y)$ and $U_\mu(x)$ transform in the same way,

$$U_\mu \to \Omega(x)U_\mu(x)\Omega^\dagger(x+\mu), \qquad G(x,y) \to \Omega(x)G(x,y)\Omega^\dagger(y). \tag{3.9}$$

As a result the link variable can be seen as a lattice version of the gauge transporter between x and $x+\hat{\mu}$. Crucially traces of path-ordered link products that form a closed loop are gauge-invariant. The smallest possible closed loop is the 'plaquette',

$$U_{\mu\nu}(x) = U_\mu(x) U_\nu(x+\hat{\mu}) U_\mu(x+\hat{\nu})^\dagger U_\nu(x)^\dagger, \tag{3.10}$$

shown in Figure 3.1. We can use the plaquette to discretize the the gluonic part of $\mathscr{L}_{\mathrm{QCD}}$. In the continuum limit, $a \to 0$, it can be shown [79],

$$\frac{\beta}{3} \sum_{x\in\Lambda} \sum_{\mu<\nu} \mathrm{Re}\mathrm{Tr}[\mathbb{1} - U_{\mu\nu}(x)] = \frac{a^4}{2g^2} \sum_{x} \sum_{\mu<\nu} \mathrm{Tr}(G_{\mu\nu}G^{\mu\nu}) + \mathcal{O}(a^2). \tag{3.11}$$

The left-hand side of (3.11) is the simplest gluonic action with the correct continuum limit,

$$S_{\mathrm{G}}[U] = \frac{\beta}{3} \sum_{x\in\Lambda} \sum_{\mu<\nu} \mathrm{Re}\mathrm{Tr}[\mathbb{1} - U_{\mu\nu}(x)], \tag{3.12}$$

where $\beta = 6/g^2$.

The link variable is also key to discretizing the fermionic part of $\mathscr{L}_{\mathrm{QCD}}$. The mass term is local and can thus be discretized immediately since $\bar{q}(x)q(x)$ is gauge-invariant on the lattice equally as it is in the continuum. In contrast the covariant derivative requires link insertions where non-local terms arise,

$$\mathcal{D}_\mu q(x) \longrightarrow \frac{U_\mu(x) q(x+\hat{\mu}) - U_{-\mu}(x) q(x-\hat{\mu})}{2a}, \tag{3.13}$$

since terms of the form $\bar{q}(x)U_\mu(x)q(x+\hat{\mu})$ are gauge-invariant but those of the form $\bar{q}(x)q(x+\hat{\mu})$ are not. The simplest discretized fermion action is written,

$$S_{\mathrm{F}}[q,\bar{q},U] = a^4 \sum_{x\in\Lambda} \bar{q}(x) \left(\sum_{\mu=1}^{4} \gamma_\mu \frac{U_\mu(x) q(x+\hat{\mu}) - U_{-\mu}(x) q(x-\hat{\mu})}{2a} + m q(x) \right), \tag{3.14}$$

or equivalently,

$$S_{\mathrm{F}}[q,\bar{q},U] = a^4 \sum_{x,y\in\Lambda} \sum_{i,j,\alpha,\beta} \bar{q}(x)^i_\alpha \; D(x|y)^{ij}_{\alpha\beta} \; q(y)^j_\beta, \tag{3.15}$$

where we have defined the Dirac operator,

$$D(x|y)^{ij}_{\alpha\beta} = \sum_{\mu=1}^{4} (\gamma_\mu)_{\alpha\beta} \frac{U_\mu(x)^{ij}\delta_{x+\hat{\mu},y} - U_{-\mu}(x)^{ij}\delta_{x-\hat{\mu},y}}{2a} + m\delta_{\alpha\beta}\delta_{ij}\delta_{xy}. \tag{3.16}$$

The full discretized action is,

$$S_{\mathrm{LQCD}}[q, \bar{q}, U] = S_{\mathrm{F}} + S_{\mathrm{G}}. \tag{3.17}$$

However, as (3.14) stands, S_{F} suffers from a serious flaw. To expose this it is useful to take the Fourier transform of the Dirac operator,

$$\tilde{D}(p|q) = \frac{1}{|\Lambda|} \sum_{x,y\in\Lambda} e^{-iap\cdot x} D(x|y) e^{iaq\cdot y}, \tag{3.18}$$

and analyse $\tilde{D}(p|q)$ in the massless case,

$$\tilde{D}(p|q) = \delta(p-q)\ \frac{i}{a} \sum_{\mu=1}^{4} \gamma_\mu \sin(p_\mu a). \tag{3.19}$$

When $p_\mu = 0$, (3.19) vanishes, corresponding to a particle. But it also vanishes when $p_\mu = \pi/a$, indicating the presence of fifteen additional unwanted particles known as 'doublers', one for each corner of the hypercube, $p_\mu a/\pi \in [0,1]$. This problem is solved by adding the Wilson term [80],

$$\frac{\mathbb{1}}{a} \sum_{\mu=1}^{4} (1 - \cos(p_\mu a)), \tag{3.20}$$

to (3.18). This extra term vanishes when $p_\mu = 0$. However for each component with $p_\mu = \pi/a$ it acts like an extra mass term by providing an additional contribution of $2/a$ to the mass of the doublers. In the continuum limit, $a \to 0$, the doublers become very heavy, decouple from the theory and leave only the physical pole, $p_\mu = 0$. This completes the Wilson formalism, which is the most basic action that can be used in lattice QCD simulations. More complicated actions can be constructed that reduce discretization errors. The process of constructing such actions is known as 'improvement'.

3.4 Hadron Spectroscopy

Lattice QCD can currently reproduce experimentally observed hadron spectra with errors down to the percent level or less, calculations have improved so much that the next steps are to include QED and u-d mass splitting effects. Also, in some channels many more states are observed in lattice simulations than in experiment [81], in fact certain resonances have even been predicted using lattice QCD, for example the mass of the B_c meson was calculated theoretically before being confirmed by experiment [82].

To introduce the conventional method of extracting hadron masses from lattice QCD simulations, we express the Euclidean time-slice correlator of two operators, $\hat{O}_1$ and $\hat{O}_2$, in a system with Hamiltonian $\hat{H}$, as a path integral over the interpolators O_1 and O_2,

$$\frac{1}{Z}\,\mathrm{Tr}\left[e^{-(\beta-\tau)\hat{H}}\hat{O}_2 e^{-\tau\hat{H}}\hat{O}_1\right] = \frac{1}{Z}\int \mathscr{D}[\phi]e^{-S_{\mathrm{LQCD}}[\phi]}O_2[\phi(.,\tau)]O_1[\phi(.,0)], \qquad (3.21)$$

where $\beta = a_\tau N_\tau$ (not to be confused with the QCD coupling), $Z = \mathrm{Tr}[\mathrm{e}^{-a_\tau N_\tau \hat{H}}]$, $[\phi] \equiv [q, \bar{q}, U]$ and S_{LQCD} is defined in (3.17). The right-hand side of (3.21) can be evaluated numerically on the lattice, while from the left-hand side we can derive an expression with which we fit the data to extract hadron spectra:

$$\begin{aligned}
\langle O_2(\tau)O_1(0)\rangle &= \frac{1}{Z}\,\mathrm{Tr}\left[e^{-(\beta-\tau)\hat{H}}\hat{O}_2 e^{-\tau\hat{H}}\hat{O}_1\right] && (3.22)\\
&= \frac{1}{Z}\sum_n \langle n|e^{-\beta H}e^{\tau H}\hat{O}_2 e^{-\tau H}\hat{O}_1|n\rangle && (3.23)\\
&= \frac{1}{Z}\sum_{n,m} e^{-\beta E_n}\langle n|e^{\tau H}\hat{O}_2 e^{-\tau H}|m\rangle\langle m|\hat{O}_1|n\rangle && (3.24)\\
&= \frac{1}{Z}\sum_{n,m} e^{-\beta E_n}e^{\tau(E_n-E_m)}\langle n|\hat{O}_2|m\rangle\langle m|\hat{O}_1|n\rangle && (3.25)\\
&= \frac{1}{Z}\sum_{n,m} e^{(\tau-\beta)E_n}e^{-\tau E_m}\langle n|\hat{O}_2|m\rangle\langle m|\hat{O}_1|n\rangle. && (3.26)
\end{aligned}$$

Sending $\beta \to \infty$ we obtain the zero temperature limit and only the $|n\rangle = |\Omega\rangle$ term remains to give,

$$\langle O_2(\tau)O_1(0)))\rangle = \frac{1}{Z}\sum_m e^{-\tau E_m}\langle\Omega|\hat{O}_2|m\rangle\langle m|\hat{O}_1|\Omega\rangle, \qquad (3.27)$$

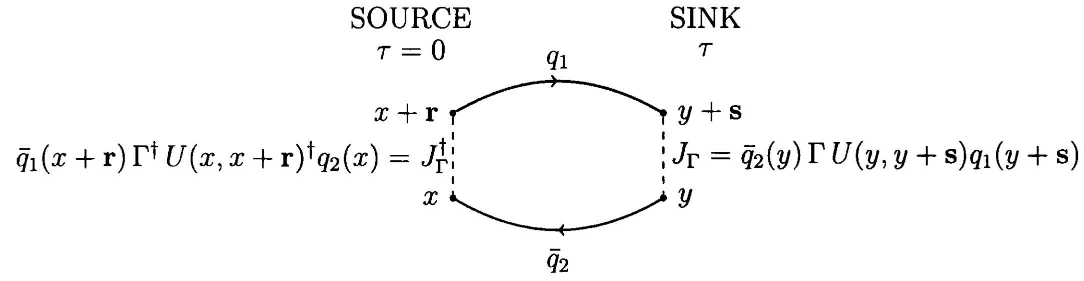
SOURCE
$\tau = 0$
SINK
τ
q_1
$x + \mathbf{r}$
$y + \mathbf{s}$
$\bar{q}_1(x+\mathbf{r})\,\Gamma^\dagger\, U(x, x+\mathbf{r})^\dagger q_2(x) = J_\Gamma^\dagger$
$J_\Gamma = \bar{q}_2(y)\,\Gamma\, U(y, y+\mathbf{s}) q_1(y+\mathbf{s})$
x
y
$\bar{q}_2$

Figure 3.2: The generic form of a meson correlator. q and $\bar{q}$ are fermion fields. $U(x, x+\mathbf{r})$ is the product of gauge links from x to $x+\mathbf{r}$ included to ensure object is gauge invariant and Γ is a product of gamma matrices that dictates the Lorentz transformation properties of the state.

where $|\Omega\rangle$ denotes the QCD vacuum state. This expression can be further simplified by considering large τ where only the ground state, E_0, survives:

$$\lim_{\tau \to \text{large}} \langle O_2(\tau) O_1(0) \rangle = \frac{1}{Z} \langle \Omega | \hat{O}_2 | 0 \rangle \langle 0 | \hat{O}_1 | \Omega \rangle e^{-\tau E_0}. \tag{3.28}$$

where $|0\rangle$ represent the charmonium ground state.

It is straight forward to apply (3.28) to a meson comprised of the quarks q_1 and $\bar{q}_2$. The meson correlator (see Figure 3.2) is,

$$C_\Gamma^{\mathbf{x},\mathbf{y},\mathbf{r},\mathbf{s}}(\tau) = \langle J(\mathbf{y}, \tau; \mathbf{s}) J^\dagger(\mathbf{x}, 0; \mathbf{r}) \rangle = \frac{1}{Z} \langle \Omega | \hat{J}(\mathbf{y}; \mathbf{s}) | 0 \rangle \langle 0 | \hat{J}^\dagger(\mathbf{x}; \mathbf{r}) | \Omega \rangle e^{-\tau E_0}. \tag{3.29}$$

where,

$$J_\Gamma^\dagger(\mathbf{x}, 0; \mathbf{r}) = \bar{q}_1(x+\mathbf{r}) \Gamma^\dagger U(x, x+\mathbf{r})^\dagger q_2(x), \tag{3.30}$$

$$J_\Gamma(\mathbf{y}, \tau; \mathbf{s}) = \bar{q}_2(y) \Gamma U(y, y+\mathbf{s}) q_1(y+\mathbf{s}), \tag{3.31}$$

are the creation and annihilation interpolators respectively. The meson state can be given definite spatial momentum by summing over all possible sink coordinates,

$$C_\Gamma^{\mathbf{x},\mathbf{q},\mathbf{r},\mathbf{s}}(\tau) = \frac{1}{\sqrt{|\Lambda_3|}} \sum_{\mathbf{y} \in \Lambda_3} \mathrm{e}^{-ia\mathbf{y}\mathbf{q}} \langle J(\mathbf{y}, \tau; \mathbf{s}) J^\dagger(\mathbf{x}, 0; \mathbf{r}) \rangle. \tag{3.32}$$

If we project the sink to zero momentum by setting $\mathbf{q} = 0$, then $E_0 = m_0$, and we can fit the time-slice correlator obtained using numerical methods to extract the meson ground state mass. Baryon masses can be extracted in exactly the same manner by utilizing a 'diquark' interpolator. For example, the local interpolator for the nucleon is,

$$O_N(x) = \epsilon_{\mathrm{abc}} u(x)_a \left(u(x)_n^T C\gamma_5 d(x)\right)_c, \tag{3.33}$$

where the term in parentheses is the diquark.

Figure 3.2 depicts a generic meson correlator. It can be likened to a Feynman diagram that illustrates the creation of a quark and anti-quark at space-time coordinates, $(\mathbf{x}, 0)$ and $(\mathbf{x}+\mathbf{r}, 0)$, and their annihilation at, $(\mathbf{y}, \tau)$ and $(\mathbf{y}+\mathbf{s}, \tau)$, respectively. When $\mathbf{q} = \mathbf{r} = \mathbf{s} = \mathbf{0}$, we can see from (3.32) that the correlator we obtain from numerical simulations, $C_\Gamma(\tau)$, will take the basic form,

$$C_\Gamma(\tau) = A_\Gamma \mathrm{e}^{-m_0 \tau}. \tag{3.34}$$

Using (3.34) as a fitting function, a two-parameter fit of $C_\Gamma(\tau)$ at large τ gives values for A_Γ and m_0. To ensure that the correlator is only fitted in the range corresponding to large τ, effective mass plots are studied. The effective mass is defined as,

$$m_{\mathrm{eff}}(\tau) = \ln\left[\frac{C_\Gamma(\tau)}{C_\Gamma(\tau+1)}\right]. \tag{3.35}$$

The range of τ where m_{eff} plateaus corresponds to the range of τ where the ground state has been isolated and (3.34) is valid.

3.5 Quenched vs. Dynamical Simulations

The action, S_{LQCD}, is bi-linear in the fermion fields q and $\bar{q}$. This allows the fermionic degrees of freedom to be integrated out. Using the right-hand side of (3.21) we can write,

$$\langle O \rangle = \frac{1}{Z} \int \mathscr{D}[U] \mathrm{e}^{-S_{\mathrm{G}}[U]} \tilde{O}[U] \prod_{f_s} \det D_{f_s}[U], \tag{3.36}$$

where,

$$Z = \int \mathscr{D}[U] \mathrm{e}^{-S_{\mathrm{G}}[U]} \prod_{f_s} \det D_{f_s}[U], \tag{3.37}$$

and $\tilde{O}[U]$ is the operator for which the fermionic degrees of freedom have been integrated out. The fermionic part of the path integral has reduced to a product of fermion matrix (Dirac operator) determinants, one for each of the sea quark flavours, f_s. A concrete example relevant to this work is the quarkonium correlator, which we can write in terms of the propagators,

$$\begin{aligned}\langle J(\mathbf{y},\tau;\mathbf{s})J^{\dagger}(\mathbf{x},0;\mathbf{r})\rangle &= \langle\, \mathrm{Tr}\left[\bar{q}(y)\Gamma U(y,y{+}\mathbf{s})q(y{+}\mathbf{s})\bar{q}(x{+}\mathbf{r})\Gamma^{\dagger}U(x,x{+}\mathbf{r})^{\dagger}q(x)\right]\rangle, \qquad (3.38)\\ &= -\langle\, \mathrm{Tr}\left[q(x)\bar{q}(y)\Gamma U(y,y{+}\mathbf{s})q(y{+}\mathbf{s})\bar{q}(x{+}\mathbf{r})\Gamma^{\dagger}U(x,x{+}\mathbf{r})^{\dagger}\right]\rangle, \qquad (3.39)\end{aligned}$$

where cycling the fermion fields, as Grassmann variables, introduces a minus sign. We can now contract the two 2-pt functions that comprise the quarkonium correlator using Wick's theorem to obtain,

$$\langle J(\mathbf{y},\tau;\mathbf{s})J^{\dagger}(\mathbf{x},0;\mathbf{r})\rangle = -\langle\, \mathrm{Tr}\left[D^{-1}(x|y)\Gamma U(y,y{+}\mathbf{s})D^{-1}(y{+}\mathbf{s}|x{+}\mathbf{r})\Gamma^{\dagger}U(x,x{+}\mathbf{r})^{\dagger}\right]\rangle, \qquad (3.40)$$

where $D^{-1}(x|y)$ is the inverse of the Dirac operator in (3.16), or equivalently the quark propagator from space-time point y to x. If we now consider the case where we have two mass degenerate quark flavours (u) and a heavier quark flavour (s) in the sea, then the Euclidean path integral according to (3.36) for the quarkonium correlator is,

$$\begin{aligned}\langle J(\mathbf{y},\tau;\mathbf{s})J^{\dagger}(\mathbf{x},0;\mathbf{r})\rangle &= -\frac{1}{Z}\int \mathscr{D}[U]\mathrm{e}^{-S_{\mathrm{G}}[U]}(\det D_u[U])^2 \det D_s[U] \qquad (3.41)\\ &\times \mathrm{Tr}\left[D^{-1}(x|y)\Gamma U(y,y{+}\mathbf{s})D^{-1}(y{+}\mathbf{s}|x{+}\mathbf{r})\Gamma^{\dagger}U(x,x{+}\mathbf{r})^{\dagger}\right], \qquad (3.42)\end{aligned}$$

where,

$$Z = \int \mathscr{D}[U]\mathrm{e}^{-S_{\mathrm{G}}[U]}(\det D_u[U])^2 \det D_s[U]. \qquad (3.43)$$

Monte Carlo importance sampling has to be performed with the corresponding Boltzmann weight — $Z^{-1}\exp[-S_{\mathrm{G}}[U]](\det D_u)^2\det D_s$. The simplest approach to performing a complete numerical simulation of QCD is to set the fermion matrix determinants to unity. This is equivalent to neglecting the vacuum loops of quarks and referred to as the quenched approximation. Otherwise, to include the effect of quark degrees of freedom on the vacuum, the fermion matrix determinants must be evaluated for each configuration, which requires a significant amount of computer time. The fermion matrices have 3(colour) × 4(spinor) × $N_s^3 N_\tau$ rows and columns. Hence for all but the smallest lattices the computational cost of calculating the determinant is very high, which means quenched simulations remain an important option. Nevertheless it is now common for realistic simulations of full QCD with 2+1 flavours of sea quark to be performed. Rational Hybrid Monte Carlo (RHMC) importance sampling is a popular method for simulating odd numbers of dynamical fermions [83]. Although, even RHMC does not involve calculating the fermion determinant explicitly, instead clever algorithms are used to approximate the fermion determinant contribution to a high degree of precision.

3.6 Quark Sources

Whether quenched or dynamical configurations are generated, quark propagators need to be calculated in order to compute the expectation value of meson correlators. The all-to-all quark propagator is a matrix as large as the fermion matrix but it is not necessary to compute it in its entirety. Instead we can consider the point-to-all propagator defined as the propagator from a fixed site, x', to any site of the lattice [79],

$$D^{-1}(y|x')^{ji}_{\beta\alpha} = \sum_{x,\alpha,i} D^{-1}(y|x)^{ji}_{\beta\alpha} S_0(x',x)^i_\alpha, \tag{3.44}$$

where the point source centred on x',

$$S_0(x',x)^i_\alpha = \delta_{x',x}, \tag{3.45}$$

is introduced. Using a fixed source is equivalent to considering a particular column of the fermion matrix. This column contains spinor and colour structure corresponding to the twelve possible combinations of i and α, consequently twelve inversions of the reduced fermion matrix, which contains only the particular column, must be performed to build the point-to-all propagator, $D^{-1}(y|x')^{ji}_{\beta\alpha}$. Inverting the fermion matrix to obtain propagators is computationally expensive. In the case of a meson comprised of mass degenerate quarks the cost can be practically halved using γ_5-

hermiticity,

$$\gamma_5 D^{-1}(y|x')\gamma_5 = D^{-1}(x'|y)^\dagger. \tag{3.46}$$

3.7 Smearing

Smearing procedures are used to improve the signal-to-noise ratio of correlators by suppressing the dependence of operators on high momentum field modes [84]. In any particular simulation a smearing procedure can be applied to the quark field, link field, or both. In each case a redefinition of the field at a given point as some weighted average of neighbouring values is involved.

Any operator with the correct quantum numbers contributes to the corresponding physical state but some may be more important than others. In most cases the overlap of the operator with the physical state can be greatly improved by giving the field interpolator a more realistic form. The general form of a smeared quark field is,

$$\bar{q}_s(x') \equiv \sum_x S(x', x)\bar{q}(x), \tag{3.47}$$

where S is the smearing function. Smearing the quark field interpolators of $J^\dagger$ in (3.30) for the derivations in Section 3.4 results in smeared propagators. This is achieved by substituting S for S_0 in (3.44). For example, the smearing function to obtain a Gaussian smeared propagator is,

$$S(x', x) = \left(1 + \frac{\sigma}{n_\sigma}\Delta_\mu\right)^{n_\sigma}, \tag{3.48}$$

where,

$$\Delta_\mu = \frac{U_\mu(x')\delta_{x'+\hat{\mu},x} - 2\delta_{x',x} + U_{-\mu}(x')\delta_{x'-\hat{\mu},x}}{a^2}, \tag{3.49}$$

is the lattice gauge-covariant Laplace operator. The two tunable parameters are the smearing radius, σ, and the number of smearing iterations, n_σ. Using a smearing function with a Gaussian form is an effective way of suppressing the high momentum modes. In addition a Gaussian in coordinate space remains a Gaussian in momentum space allowing the smeared quark field to be defined at a given site as a Gaussian-weighted average of the surrounding sites on the same time-slice [85].

The correlator signal can also be improved by smearing the link field, which is equivalent to removing the high momentum modes of the gauge fields. Violent short distance fluctuations can negatively affect the clarity of the signal over longer distances, which are typically of more interest. So long as the link variables are replaced by averages over short paths connecting the link's endpoints, the long distance behaviour of correlators in the continuum limit should not be affected.

In this work stout-link smearing [86] is employed. This method defines the smeared link after an iteration of the smearing algorithm as,

$$U'_\mu(x) = \mathrm{e}^{iQ_\mu(x)} U_\mu(x), \tag{3.50}$$

where,

$$Q_\mu(x) = \frac{i}{2}\left(\omega_\mu(x)^\dagger - \omega_\mu(x) - \frac{\mathbb{1}}{3}\,\mathrm{Tr}[\omega_\mu(x)^\dagger - \omega_\mu(x)]\right), \tag{3.51}$$

$$\omega_\mu(x) = \left(\sum_{\nu\neq\mu} \rho_{\mu\nu} C_{\mu\nu}(x)\right) U_\mu(x)^\dagger, \tag{3.52}$$

and the 'staples' are defined,

$$\begin{align} C_{\mu\nu}(x) = {} & U_\nu(x) U_\mu(x+\hat{\nu}) U_\nu(x+\hat{\mu})^\dagger \tag{3.53} \\ & + U_\nu(x-\hat{\nu})^\dagger U_\mu(x-\hat{\nu}) U_\nu(x-\hat{\nu}+\hat{\mu}). \tag{3.54} \end{align}$$

The tunable parameters are the real weight factors $\rho_{\mu\nu}$. Typically they are to set to a constant, $\rho_{\mu\nu} = \rho$. Another choice is to smear only the spatial links: $\rho_{\mu 4} = \rho_{4\mu} = 0$, $\rho_{nm} = \rho$ [79]. The major advantage of stout-link smearing over APE [87] or HYP [88] link smearing is that the smeared links $U'_\mu(x)$ are differentiable with respect to the link variables, which is particularly beneficial when the Hybrid Monte Carlo method for dynamical quarks is being employed.

3.8 Gauge Fixing

Correlators built from non-local operators are not intrinsically gauge-invariant. There are two approaches that can be employed to ensure the correct expectation value is obtained: (i) include path-ordered products of link variables that with the quark propagators form a closed loop (ii) fix the gauge. The first approach requires the link products $U(x, x + \mathbf{r})$ and $U(y, y + \mathbf{s})$ included in Figure 3.2 and related derivations. This approach is easy to implement but fluctuations in the link products configuration by configuration can introduce extra noise into the correlator signal. The second approach requires each configuration to undergo a gauge-fixing procedure before the expectation value is measured. This procedure costs a more significant amount of computer time than including link products, but results in cleaner correlator signals. The Coulomb gauge, $\nabla \cdot \mathbf{A} = 0$, is particularly appropriate when interested in the time-slice behaviour of an observable. Other gauges, such as the Landau gauge, $\partial_\mu A_\mu(x) = 0$, and temporal gauge, $A_0(x) = 0$, are also used on the lattice.

3.9 Non-Zero Temperature

Comparing the partition function of (3.21) with that of a thermal system, $Z = \mathrm{Tr}[\mathrm{e}^{-\beta \hat{H}}]$, we can identify [37],

$$\beta = \frac{1}{k_B T} = a_\tau N_\tau, \tag{3.55}$$

where $a_\tau = a$ for isotropic lattices and k_B is set to unity when working with lattice results. In Section 3.4 we formally take the zero temperature limit $\beta \to 0$, but this can never fully be realized on a finite lattice. As a result lattice studies are always performed at non-zero temperature but those interested in zero temperature physics work with large enough $a_\tau N_\tau$ such that their calculations are performed well within the low temperature regime. In this work we calculate the charmonium potential over ensembles with the same a_τ but different N_τ to investigate its temperature dependence. Another way of investigating the temperature dependence of observables is to keep N_τ fixed and vary a_τ via the lattice coupling,

$$\beta = 6/g^2(a_\tau). \tag{3.56}$$

Note that the lattice coupling and inverse temperature are both represented by β. The relationship between a_τ and the coupling β is given by the renormalization group. When working with lattices with small or moderate $a_\tau N_\tau$ anti-periodic boundary conditions must be applied to quarks and periodic boundary conditions to the gauge fields.

To properly discuss the relevance of any change in the charmonium potential with temperature it is important to know the temperature range corresponding to the cross-over transition. The Polyakov loop,

$$L(\mathbf{x}) = \mathrm{Tr}\left[\prod_{j=0}^{N_\tau-1} U_0(\mathbf{x}, j)\right], \tag{3.57}$$

is defined as a product of temporal links, U_0, that form a closed loop at spatial position $\mathbf{x}$. The correlator of Polyakov loops at $\mathbf{x}$ and $\mathbf{y}$ is related to the free energy $F_{q\bar{q}}(|\mathbf{x}-\mathbf{y}|)$ of a static quark–anti-quark pair at temperature T,

$$\left\langle L(\mathbf{x})L(\mathbf{y})^\dagger\right\rangle = \mathrm{e}^{-a_\tau N_\tau F_{q\bar{q}}(|\mathbf{x}-\mathbf{y}|)} = \mathrm{e}^{-F_{q\bar{q}}(\mathbf{r})/T}, \tag{3.58}$$

where $\mathbf{r} = |\mathbf{x}-\mathbf{y}|$. At large distance the Polyakov loop correlator tends towards the product of the expectation values of the individual Polyakov loops,

$$\lim_{r\to\text{large}} \left\langle L(\mathbf{x})L(\mathbf{y})^\dagger\right\rangle \to \left\langle L(\mathbf{x})\right\rangle \left\langle L(\mathbf{y})^\dagger\right\rangle = \left|\langle L\rangle\right|^2. \tag{3.59}$$

The large distance behaviour of the free energy on the lattice can hence be obtained by computing the average value of the Polyakov loop over all sites,

$$L = \frac{1}{3}\sum_{\mathbf{x}} L(\mathbf{x}). \tag{3.60}$$

In the absence of dynamical fermions there is no string breaking and the free energy is expected to grow indefinitely with separation in the confined phase [79]. Therefore we can conclude,

$$\langle L\rangle = 0 \;\; \text{in confined phase,} \tag{3.61}$$

$$\langle L\rangle \neq 0 \;\; \text{in deconfined phase.} \tag{3.62}$$

Furthermore under a global Z_3 transformation the gauge sector of the lattice QCD Lagrangian is invariant but $L(x)$ transforms as,

$$L \to zL, \qquad z \in Z_3. \tag{3.63}$$

In quenched QCD this means the Polyakov loop is an exact order parameter that tests whether the state of the system shares or spontaneously breaks the symmetry of the Lagrangian. It can thus be used to determine the temperature of the cross-over transition. Lattice studies indicate the Polyakov loop behaves as shown in Figure

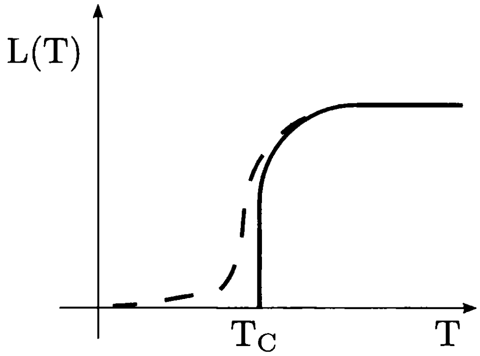

Figure 3.3: A schematic diagram of the Polyakov loop behaviour at non-zero temperature. Solid line: for pure gauge theory the Polyakov loop is an exact order parameter becoming non-zero and positive in the deconfined phase above the critical temperature, T_C. Dashed line: even when the quarks take finite masses the Polyakov loop still has near-critical behaviour.

3.3 as a function of temperature. The deconfinement temperature, T_C, is found to be approximately 270MeV in quenched simulations. If dynamical fermions are included in the simulation then the Polyakov loop is no longer a genuine order parameter, but lattice studies show that it still has near-critical behaviour, which corresponds to a rapid cross-over transition. The rapidity of the cross-over means it is still sensible to define a pseudo-critical temperature, T_C, in dynamical simulations — it is found to be approximately 154MeV [38,89,90].

In pure gauge theory the lightest states that can be created from the vacuum are glueball states which are significantly heavier than the pions present in dynamical QCD. We can see the decrease in T_C between quenched and dynamical simulations as a result of the relative increase in the density of colour charges in the latter, at any given temperature.

3.10 Anisotropic Lattices

Anisotropic lattices have different temporal and spatial lattice spacings, a_τ and a_s, respectively. The anisotropy is defined as $\xi = a_s/a_\tau$. Anisotropic lattices with $\xi > 1$ are advantageous for those interested in the time-slice behaviour of observables at non-zero temperature for two entwined reasons:

- The number of data points in the temporal dimension can be increased at a relatively low computational cost.
- The spatial volume can be kept fixed.

Correlators decrease exponentially at a rate proportional to the energy eigenstates of the Hamiltonian (see (3.34)). Consequently heavy quark correlators have a small magnitude at large τ. To resolve the correlator at large τ it is helpful, and often necessary, to have a large number of finely separated time-slice data points. Anisotropic lattices can be used to increase resolution in the temporal dimension, without the bind of an increasing spatial volume, by setting $\xi > 1$. With anisotropic lattices we are free to keep both a_s and N_s fixed, while reducing a_τ to a_s/ξ. If the number of data points in the temporal dimension is increased appropriately by a factor of ξ, then the lattice size is kept constant but the temporal resolution increased at relatively little computational cost.

In this work temperature dependence is investigated by varying the temporal extent of an anisotropic lattice, see (3.55). The advantage of being able to keep the spatial volume fixed is particularly important here because it means any changes in the potential are definitely not due to spatial volume effects. There are two minor disadvantages to this approach: i) The temperature can only be varied in discrete steps, ii) The number of points in the temporal dimension changes from ensemble to ensemble (temperature to temperature), which means care must be taken to ensure spurious results are not obtained during the fitting of correlators — the number of data points available to fitting algorithms can change the results they provide.

An alternative method of investigating temperature dependence is to vary a_τ while keeping N_τ fixed, and thus set the temperature according to (3.56). The advantage of this would be the ability to vary the temperature contiguously, however to rule out spatial volume effects during the investigation a_s would be have to be kept fixed. As a result varying the temperature would correspond to varying the anisotropy, which would be impractical because each anisotropy value requires a very time-consuming tuning procedure.

Chapter 4

Conventional Fitting Approach

In this chapter conventional fitting methods, typically used for hadron spectroscopy on the lattice, are employed to extract the charmonium wave function, which is subsequently used to reverse-engineer the charmonium potential from the Schrödinger equation at a number of temperature values.

4.1 Nambu-Bethe-Salpeter Wave Functions

If our sole interest was in computing charmonium masses at zero-temperature, the techniques introduced in Section 3.4 would be sufficient to obtain sensible values for ground state masses, e.g. m_{η_c}, $m_{J/\psi}$, though much more sophisticated hadron spectroscopy techniques are used nowadays, for example the variational method [91, 92]. Also the value of A_Γ from (3.34) would not be exposed to any further interpretation. In our case we are interested in identifying A_Γ with the product of the wave functions at the source and sink.

The relativistic equation for a two particle bound state is the (Nambu-)Bethe-Salpeter equation [93]. The NBS equation describes bound states in a quantum field theory in a relativistically covariant formalism. Consequently charmonium states are solutions of the NBS equation. Analytically solving the NBS equation to obtain solutions corresponding to charmonium states is not straightforward, though some progress has been made [94, 95]. In this work we treat the charmonium system non-relativistically, in this limit the NBS equation reduces to the Schrödinger equation and we argue that the charm quark, specifically the constituent charm quark, is heavy enough for this approximation to be valid. In the literature it is common to refer to the matrix elements, $\langle 0|J^\dagger(\mathbf{x};\mathbf{r})|\Omega\rangle$ and $\langle \Omega|J(\mathbf{y};\mathbf{s})|0\rangle$, of (3.29) as NBS wave functions. In this work we simply refer to them as wave functions, noting that the amplitudes are just the overlap of charm and anti-charm states — with the correct quantum numbers — with the ground state of charmonium:

$$\langle 0|J^\dagger(\mathbf{x};\mathbf{r})|\Omega\rangle = \psi^*_\Gamma(\mathbf{r}), \tag{4.1}$$

$$\langle \Omega|J(\mathbf{y};\mathbf{s})|0\rangle = \psi_\Gamma(\mathbf{r}), \tag{4.2}$$

where $|\Omega\rangle$ and $|0\rangle$ represent the QCD vacuum and charmonium ground state respectively, and Γ represents the relevant γ-matrix monomial. The relationships, (4.1) and (4.2), are not explicitly gauge-invariant. To ensure gauge-invariance the gauge must either be fixed, or gauge-links must be included where non-local operators appear.

4.2 Reverse-Engineering the Potential

To reverse-engineer the potential using the Schrödinger equation we must first obtain the wave function as a function of the quark separation, $\mathbf{r}$. To do so we must analyse correlators computed with at least one extended interpolator. Looking at (3.32) and Figure 3.2, the following three source-sink arrangements of the quarks can be imagined:

- *Local-local*: $\mathbf{r} = \mathbf{s} = \mathbf{0}$, give clean signals that can be fitted to perform meson spectroscopy but they do not provide any information on observables with an extended nature, such as the interquark potential.

- *Local-extended / extended-local*: $\mathbf{r} = \mathbf{0}$ and $\mathbf{s} \neq \mathbf{0}$, or $\mathbf{r} \neq \mathbf{0}$ and $\mathbf{s} = \mathbf{0}$. Extended-local correlators are undesirable because it is statistically advantageous to have the extended operator at the sink, where a sum over spatial lattice points is performed to fix the momentum. For this reason, local-extended meson correlators are always used when interested in using a correlator with either the source or sink extended but not both.

- *Extended-extended*: $\mathbf{r} = \mathbf{s} \neq \mathbf{0}$, suffer from statistical noise more severely than local-extended correlators but the product of the matrix elements is guaranteed to be positive-definite for all excited states, which can aid analysis. We do not consider the $\mathbf{r} \neq \mathbf{s} \neq \mathbf{0}$ case.

A two-parameter fit of a local-local correlator using (3.34) as the fitting function yields the 'wave function product',

$$A_\Gamma^{LL} = \langle\Omega|J(\mathbf{y};\mathbf{0})|0\rangle\langle 0|J^\dagger(\mathbf{x};\mathbf{0})|\Omega\rangle = \psi_\Gamma(\mathbf{0})\psi_\Gamma^*(\mathbf{0}) \tag{4.3}$$

The expressions equivalent to (4.3) for local-extended and extended-extended correlators are,

$$A_\Gamma^{LE}(\mathbf{r}) = \psi_\Gamma(\mathbf{r})\psi_\Gamma^*(\mathbf{0}) \quad \text{and} \quad A_\Gamma^{EE}(\mathbf{r}) = \psi_\Gamma(\mathbf{r})\psi_\Gamma^*(\mathbf{r}), \tag{4.4}$$

respectively. By analysing correlators corresponding to different quark separations, the wave function as a function of $\mathbf{r}$ can built using,

$$\Psi_\Gamma(\mathbf{r}) = \frac{A_\Gamma^{LE}(\mathbf{r})}{\sqrt{A_\Gamma^{LL}}} \quad \text{or} \quad \Psi_\Gamma(\mathbf{r}) = \sqrt{A_\Gamma^{EE}(\mathbf{r})}, \tag{4.5}$$

for either the local-extended or extended-extended case, respectively.

In possession of a method to obtain the wave function as a function of quark separation we can now calculate the potential. As discussed in Section 4.1 the charmonium wave function is assumed to obey the Schrödinger equation,

$$\left(-\frac{\nabla^2}{2\mu} + V_\Gamma(\mathbf{r})\right)\Psi_\Gamma(\mathbf{r}) = E_\Gamma\Psi_\Gamma(\mathbf{r}). \tag{4.6}$$

where μ and E_Γ are the reduced mass and energy of the charmonium system and Γ indicates the Lorentz transformation properties of the state being considered. Rearranging (4.6) for the charmonium potential gives,

$$V_\Gamma(\mathbf{r}) = \frac{1}{2\mu}\frac{\nabla^2\Psi_\Gamma(\mathbf{r})}{\Psi_\Gamma(\mathbf{r})} + E_\Gamma. \tag{4.7}$$

So in addition to the wave function $\Psi_\Gamma(\mathbf{r})$, we require μ and E_Γ to reverse-engineer the charmonium potential. The reduced mass is,

$$\mu = \frac{m_c m_{\bar{c}}}{m_c + m_{\bar{c}}} = \frac{m_c}{2}, \tag{4.8}$$

and in this work, as in [96], the charm quark mass is defined as $m_c = M_V/2$, where M_V is the mass of the vector channel ground state. Therefore the reduced mass is simply, $\mu = M_V/4$, with M_V to be determined by analysing vector effective mass plots, see (3.35). The energy of the charmonium state is also obtained from plotting the effective mass, because for zero momentum states the contribution of E_Γ is equal

Γ	J^{PC}	Channel	Resonance
1	0^{++}	a_0	$^3P_0(\chi_{c0})$
γ_i	1^{--}	ρ	$^3S_1(J/\psi)$
γ_5	0^{-+}	π	$^1S_0(\eta_c)$
$\gamma_i\gamma_j$	1^{+-}	b_1	$^1P_1(h_c)$
$\gamma_5\gamma_i$	1^{++}	a_1	$^3P_1(\chi_{c1})$

J	Representation
0	A_1
1	T_1
2	ET_2
3	$A_2T_1T_2$
4	$A_1ET_1T_2$

Table 4.1: Left: γ-matrix insertions and their corresponding J^{PC} values in the continuum. Right: Representations of spin under the cubic group, O_h.

to the mass of the state. With the reduced mass and energy of the charmonium system, the final step towards obtaining the potential is to use the finite difference operator,

$$\frac{\delta_{r',r+a} - 2\delta_{r',r} + \delta_{r',r-a}}{a^2} + \frac{\delta_{r',r+a} - \delta_{r',r-a}}{na^2}, \tag{4.9}$$

to evaluate the second derivative,

$$\nabla^2 \equiv \frac{1}{r^2}\frac{\partial}{\partial r}\left(r^2\frac{\partial}{\partial r}\right) = \frac{\partial^2}{\partial r^2} + \frac{2}{r}\frac{\partial}{\partial r}, \tag{4.10}$$

of (4.7), where we are depending on the approximate rotational symmetry of the lattice.

Repeating the method outlined above on ensembles which differ only by the extent of their temporal direction, we can investigate the temperature dependence of the potential. However, we must remember we are using an equation, (3.27), which is only rigorously valid at zero-temperature to study non-zero temperature effects, and we must bear this in mind when drawing conclusions from the results.

4.3 S-Waves

Lorentz transformation properties play a significant role in determining the spectrum of states. A quark bi-linear in QCD, $\bar{q}\Gamma q$, where Γ is one of the sixteen independent γ-matrix combinations, has the J^{PC} values listed in Table 4.1(left) in the continuum. Parity and charge conjugation operations do not change when moving to the lattice but the representations of spin are constrained by the exclusive cubic symmetry of the spatial volume. A state with spin J has $2J+1$ spin components that are degenerate in mass and form a $2J+1$ dimensional representation in the continuum. On the lattice there exist only 1, 2 and 3-dimensional representations.

The 1-dimensional representations are labelled A_1 and A_2, the 2-dimensional is E and the 3-dimensional T_1 and T_2. The relationship of these representations to those of $SU(2)$ can be derived through the process of subduction. In this case the $SU(2)$ representations would be restricted to the rotations allowed by the cubic symmetry group, O_h [97,98]. Table 4.1 (right) shows the results of subduction up to $J = 4$. In the non-relativistic limit obtained by projecting the quark spinor with $1 + \gamma_4$, the sixteen continuum quark bi-linears reduce to four, which have the π and ρ quantum numbers only — as in the naive quark model [97]. The π and ρ channels are the most appropriate from which to extract the charmonium wave function since we are using the non-relativistic Schrödinger equation to obtain the charmonium potential.

The π and ρ resonances are S-wave states, taking into account only the non-zero leading order terms of the velocity expansion [99], the interquark potential between the quarks in these states can be expressed as,

$$V_\Gamma(\mathbf{r}) = V_\mathrm{C}(\mathbf{r}) + V_\mathrm{S}(\mathbf{r}) s_1 \cdot s_2, \tag{4.11}$$

where V_C is the spin-independent potential, V_S is the spin-dependent potential and $s_{1,2}$ are the quark spins. Using $s_1 \cdot s_2 = -3/4, 1/4$ for the pseudoscalar and vector channels respectively, $V_\mathrm{C}(\mathbf{r})$ and $V_\mathrm{S}(\mathbf{r})$ can be obtained from the following expressions,

$$V_\mathrm{C}(\mathbf{r}) = \frac{1}{4} V_\mathrm{PS} + \frac{3}{4} V_\mathrm{V}, \tag{4.12}$$

$$V_\mathrm{S}(\mathbf{r}) = V_\mathrm{V} - V_\mathrm{PS}. \tag{4.13}$$

4.4 $N_f=2$ Simulation Details

For measurement the ensembles listed in Table 4.2 were used. The gauge action used was the two-plaquette Symanzik-improved action of [100],

$$\begin{aligned} S_\mathrm{G}^\mathrm{SYM}[U] = {} & \frac{\beta}{\xi_g^0} \sum_{x,s<s'} \left\{ \frac{5(1+\omega)}{3u_s^4} \mathcal{P}_{ss'} - \frac{5\omega}{3u_s^8} \mathcal{P}^{(2)}_{ss'} - \frac{1}{12u_s^6} \mathcal{R}_{ss'} \right\} \\ & + \beta \xi_g^0 \sum_{x,s} \left\{ \frac{4}{3u_s^2 u_\tau^2} \mathcal{P}_{s\tau} - \frac{1}{12 u_s^4 u_\tau^2} \mathcal{R}_{s\tau} \right\}, \end{aligned} \tag{4.14}$$

where $\mathcal{P}$ is the plaquette, $\mathcal{R}$ is the 2×1 rectangular Wilson loop and $\mathcal{P}^{(2)}_{ss'}$ is constructed from two spatial plaquettes separated by a single temporal link, see Figure 4.1. u_s and u_τ are the mean spatial and temporal gauge link values respectively.

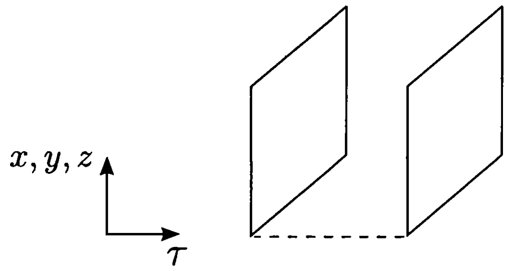

Figure 4.1: Schematic diagram of $\mathcal{P}^{(2)}_{ss'}$. The term is constructed from two spatial plaquettes separated by a single temporal link.

$S_{\mathrm{G}}^{\mathrm{SYM}}$ has leading discretization errors of $\mathcal{O}(a_s^3, a_\tau, \alpha_s a_s)$. The free parameter ω is chosen such that the approach to the QCD continuum is made on a trajectory far away from the critical point in the plane of fundamental-adjoint couplings.

The fermion action used was the fine Wilson, coarse Hamber-Wu action of [101],

$$\begin{aligned} S_{\mathrm{F}}^{\mathrm{fWcHW}}[U,q,\bar{q}] = \frac{1}{a_\tau}\Bigg\{ & \bar{q}(x)\left(\mu_r m a_\tau + \frac{18s}{\xi} + r\right) q(x) \\ & - \frac{1}{2u_\tau}\left[\bar{q}(x)(r-\gamma_0)U_\tau(x)q(x+\hat{\tau}) + \bar{q}(x)(r+\gamma_0)U_\tau^\dagger(x-\hat{\tau})q(x-\hat{\tau})\right] \\ & - \frac{1}{\xi_q}\sum_i \Big[\frac{1}{u_s}\bar{q}(x)(4s - \frac{2}{3}\mu_r\gamma_i)U_i(x)q(x+\hat{\imath}) \\ & + \frac{1}{u_s}\bar{q}(x)(4s + \frac{2}{3}\mu_r\gamma_i)U_i^\dagger(x-\hat{\imath})q(x-\hat{\imath}) \\ & - \frac{1}{u_s^2}\bar{q}(x)(s - \frac{1}{12}\mu_r\gamma_i)U_i(x)U_i(x+\hat{\imath})q(x+2\hat{\imath}) \\ & - \frac{1}{u_s^2}\bar{q}(x)(s + \frac{1}{12}\mu_r\gamma_i)U_i^\dagger(x-\hat{\imath})U_i^\dagger(x-2\hat{\imath})q(x-2\hat{\imath})\Big]\Bigg\} \end{aligned} \tag{4.15}$$

where u_s and u_τ are the mean-link improvement parameters. u_s is determined from the spatial plaquette and u_τ is set to unity. The fermion anisotropy ξ_q is given by the ratio of scales, $\xi = a_s/a_\tau$. This fermion action is classically improved to $\mathcal{O}(a_\tau, a_s^3)$. The chromoelectric term included in [101], is set to zero in this work. μ_r is set to unity, and s is set to 1/8. The fermion action is improved in the spatial dimension but not in the temporal one. The doublers in space and time are removed by the Wilson term.

Configurations with two light mass-degenerate quark flavors were sampled using the Hybrid Monte Carlo algorithm with time step anisotropy. The temporal and spatial lattice spacings were measured to be $a_s \simeq 0.162$fm and $a_\tau^{-1} \simeq 7.35$GeV [102,103] respectively, giving an anisotropy of $\xi = a_s/a_\tau \approx 6$. Crucially the ensembles correspond to a temperature range from the confined phase up to $2.09T_C$ where T_C is the deconfining transition. T_C was estimated from the point where the unrenormalized Polyakov loop starts to become non-zero, see Section 3.9. Charmonium correlators were calculated over the ensembles using Chroma [105], a software system developed specifically for lattice QCD. Gauge links were inserted within non-local operators to ensure gauge-invariance. The bare charm quark mass used was, $a_\tau m_c^0 = 0.0117$, with $m_\pi/m_\rho = 0.54$. The bare anisotropy for the charm quarks was $\xi_c^0 = 5.9$. The computations were performed on an IBM Bluegene/P hosted by Swansea University for the UKQCD collaboration.

N_s	N_τ	T(MeV)	T/T_c	N_{cfg}
12	80	90	0.42	250
12	32	230	1.05	1000
12	28	263	1.20	1000
12	24	306	1.40	500
12	20	368	1.68	1000
12	16	459	2.09	1000

Table 4.2: The table shows the lattice size, (N_s, N_τ), the corresponding temperature, T, in units of MeV and T_C, and the number of configurations in each ensemble, N_{cfg}. The bare (input) anisotropies used in the generation of the configurations were: $\xi_g^0 = 8.42$ for the gluons and $\xi_s^0 = 7.43$ for the sea quarks. The renormalized (measured) anisotropies were $\xi_g = 6.04$ and $\xi_s = 5.84$. The bare sea quark mass used was $a_\tau m_s^0 = -0.057$ [104].

4.5 Results

Local-extended and extended-extended charmonium correlators corresponding to all possible on-axes quark separations were obtained. Correlators corresponding to quark separations of the same magnitude were then averaged to give a set of seven correlators corresponding to the quark separations $r/a_s = 0, 1, 2, 3, 4, 5, 6$.

In the local-extended case correlators were computed with and without Gaussian smeared sources. To perform Gaussian smearing the smearing parameters n_σ and σ from (3.48) had to be tuned. To judge the effectiveness of a certain choice of smearing parameters effective mass plots were generated using (3.35). Plots in which the mass values at small τ were closest to those obtained for large τ were interpreted

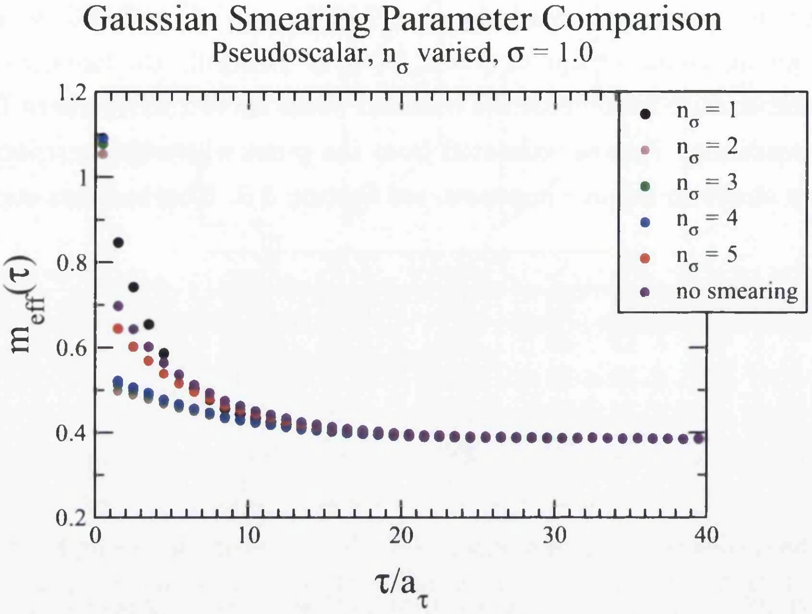

Figure 4.2: A study of the smearing effect seen when holding $\sigma = 1.0$ while varying n_σ. Based on this plot $n_\sigma = 2$ was chosen.

as the most effective. A complete study of the 2-dimensional parameter space was prohibitively time-consuming. Instead a scan through n_σ holding $\sigma = 1.0$ was first performed, shown in Figure 4.2. From this scan $n_\sigma = 2$ was found to be the most effective number of smearing iterations. A subsequent scan through σ while holding $n_\sigma = 2$, shown in Figure 4.3, found $\sigma = 1.0$ to be the most effective smearing width. The most effective smearing parameter choice was thus deemed to be $(n_\sigma = 2, \sigma = 1.0)$. It is possible a better choice exists somewhere in the (n_σ, σ) parameter space, however this is unlikely because aggressive smearing, i.e. larger n_σ or σ, appears to have a negative effect based on Figure 4.2 and Figure 4.3.

The sets of extended-extended and local-extended correlators from the $1.05T_C$ ensemble are shown in Figure 4.4 and Figure 4.5 respectively, to show the quality of the data. The local-extended correlators in Figure 4.5 are unsmeared; the Gaussian smeared data is very similar.

Initially the wave function was obtained by fitting each correlator separately using (3.34) as the form of the fitting function and (4.5) to isolate the wave function. Naively fitting each correlator separately provided reliable results for correlators corresponding to quark separations $r/a_s = 0, 1, 2, 3$, but was unsatisfactory for the largest three separations, for which fits yielded inconsistent mass values.

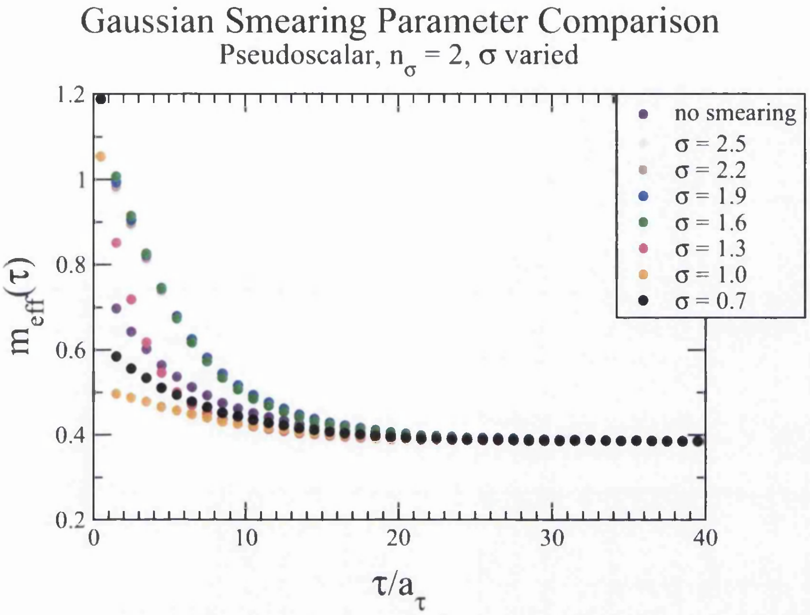

Figure 4.3: A study of the smearing effect seen when holding $n_\sigma = 2$ while varying σ. Based on this plot the $\sigma = 1.0$ was chosen.

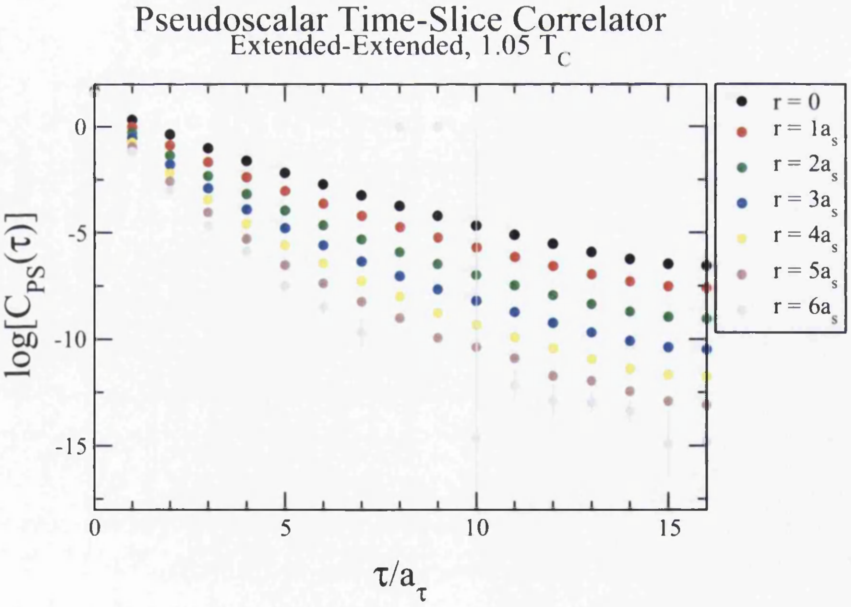

Figure 4.4: $1.05T_C$ extended-extended correlators. Extended-extended correlators always decay exponentially since every excited state contributes to the correlator with a positive sign.

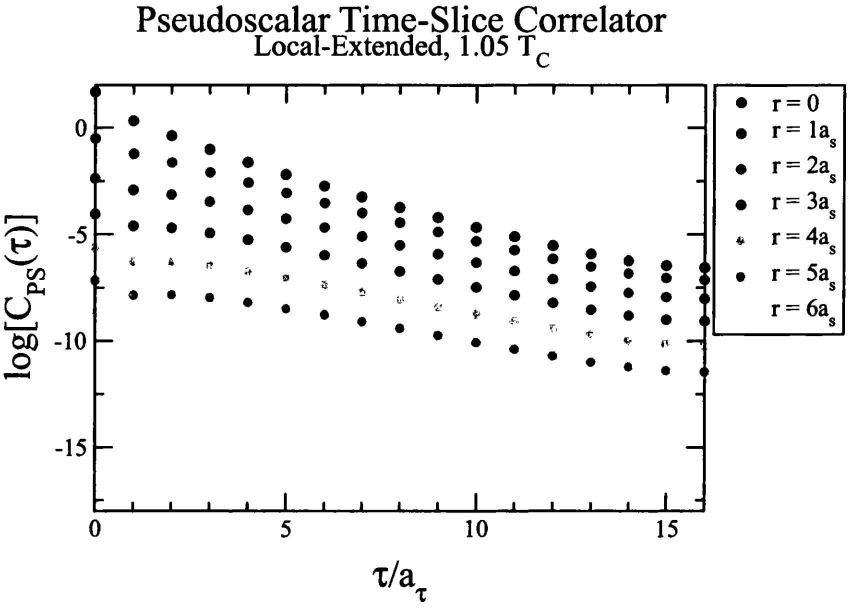

Figure 4.5: $1.05T_C$ local-extended correlators. Local-extended correlators do not always decay exponentially. At small τ the correlators have the opposite curvature to an exponentially decaying function, a sign that higher excited states with a negative wave function product are contributing to the correlator..

Consequently the wave function products, see (4.4), were deemed unreliable for $r/a_s = 4, 5, 6$.

To obtain reliable values for the wave function products corresponding to each quark separation, a simultaneous fit was performed on each set of correlators using an eight-parameter fitting function — one parameter for the mass and seven for the wave function products corresponding to each quark separation, $r/a_s = 0, 1, 2, 3, 4, 5, 6$. This method uses the smallest separations to anchor the mass parameter to a value very close to that obtained when the local-local correlator is fitted with a two-parameter fitting function. The eight-parameter fit yielded reliable results for all quark separations when applied to the extended-extended correlators. Figure 4.6 shows the output from the fitting procedure performed on the $1.05T_C$ extended-extended correlators. In this case a fitting range of $\tau = 10-16$ was chosen based on the plateau seen in the $1.05T_C$ effective mass plot shown in Figure 4.7. Fitting ranges for other ensembles were chosen by studying the corresponding effective mass plot in the same manner.

Fitting algorithms can converge to solutions equivalent to a local rather than global minimum of the χ^2. Therefore it is important to provide the fitting algo-

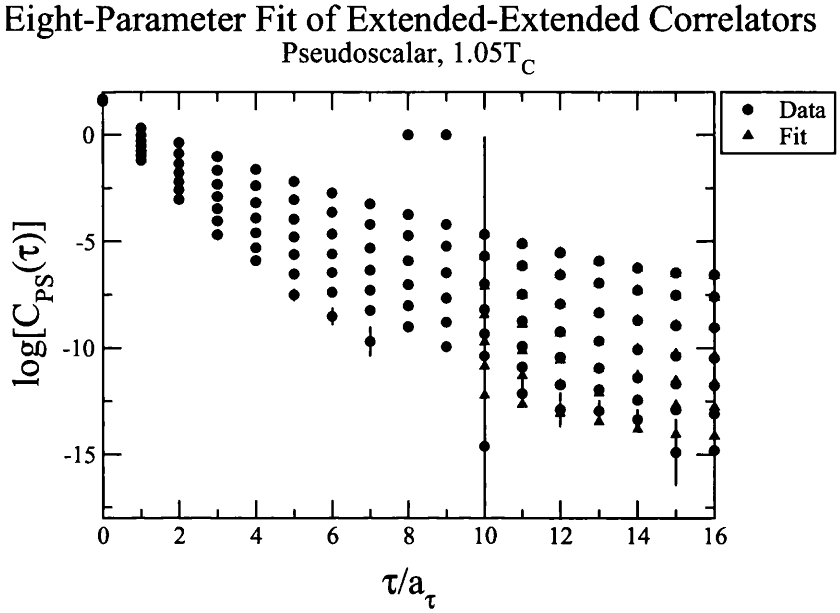

Figure 4.6: The eight-parameter simultaneous fit of the $1.05T_C$ extended-extended correlators, which was performed for $\tau = 10 - 16$.

rithms with a starting point in parameter space which is sensible, in this work this was provided by a linear fit. To further ensure values corresponding to the true global minimum of the parameter space were obtained, reliable fits were identified by comparing the results of three different fitting algorithms: the Minuit [106], Simplex [107] and Simulated Annealing [107] fitting algorithms.

Reliable fits were not obtained on the sets of local-extended correlators. Extended-extended correlators have symmetric source and sink operators, guaranteeing a positive-definite wave function product for every excited state, whereas local-extended correlators do not and the wave function product can be positive or negative for any excited state. Also in correlators from ensembles with $N_\tau < 80$ the ground state is not the only surviving state at largest available τ. Taking these points into consideration we can see why the fitting function is more likely to fail in the local-extended case than in the extended-extended case: in the extended-extended case contributions to the correlator from higher excited states are all positive, whereas in the local-extended case contributions can be positive or negative. In the fitting function there is a single positive term exponentially decaying with τ, this term can encapsulate the behaviour of a sum of positive terms exponentially decaying with τ more easily than a sum of positive and negative terms exponentially decaying with τ. Of

$T(T_C)$	0.42	1.05	1.20	1.40	1.68	2.09
M_{PS}	0.3907(4)	0.4345(4)	0.4438(5)	0.4633(9)	0.4914(10)	0.5395(11)
$\|\Psi(r=0)\|^2$	0.1014(14)	$7.30(11)\times10^{-2}$	$6.77(12)\times10^{-2}$	$6.3(2)\times10^{-2}$	$5.02(11)\times10^{-2}$	$3.56(8)\times10^{-2}$
$\|\Psi(r=1a_s)\|^2$	$3.55(4)\times10^{-2}$	$2.59(4)\times10^{-2}$	$2.43(4)\times10^{-2}$	$2.28(7)\times10^{-2}$	$1.86(4)\times10^{-2}$	$1.41(3)\times10^{-2}$
$\|\Psi(r=2a_s)\|^2$	$7.28(8)\times10^{-3}$	$6.47(9)\times10^{-3}$	$6.26(10)\times10^{-3}$	$6.2(2)\times10^{-3}$	$5.59(11)\times10^{-3}$	$4.95(10)\times10^{-3}$
$\|\Psi(r=3a_s)\|^2$	$1.18(3)\times10^{-3}$	$1.68(2)\times10^{-3}$	$1.78(3)\times10^{-3}$	$1.86(5)\times10^{-3}$	$1.85(4)\times10^{-3}$	$1.97(4)\times10^{-3}$
$\|\Psi(r=4a_s)\|^2$	$2.04(14)\times10^{-4}$	$4.73(14)\times10^{-4}$	$5.2(2)\times10^{-4}$	$6.0(2)\times10^{-4}$	$6.5(2)\times10^{-4}$	$8.3(2)\times10^{-4}$
$\|\Psi(r=5a_s)\|^2$	$3.8(11)\times10^{-5}$	$1.50(14)\times10^{-4}$	$1.6(2)\times10^{-4}$	$1.6(2)\times10^{-4}$	$2.7(2)\times10^{-4}$	$3.7(2)\times10^{-4}$
$\|\Psi(r=6a_s)\|^2$	$3.0(110)\times10^{-6}$	$4.0(20)\times10^{-5}$	$5.0(20)\times10^{-5}$	$4.0(40)\times10^{-5}$	$1.3(3)\times10^{-4}$	$1.5(3)\times10^{-4}$
$\langle r^2\rangle^{1/2}$ [fm]	0.3308(91)	0.4208(95)	0.4357(104)	0.4400(187)	0.5054(109)	0.5456(95)

Table 4.3: A table of the pseudoscalar wave function squared, for each separation, and mass obtained from simultaneous fits of extended-extended correlators, for each temperature.

$T(T_C)$	0.42	1.05	1.20	1.40	1.68	2.09
M_V	0.4092(4)	0.4584(4)	0.4664(4)	0.4850(7)	0.5090(7)	0.5526(8)
$\|\Psi(r=0\|^2$	$6.03(13)\times10^{-2}$	$4.36(9)\times10^{-2}$	$4.10(8)\times10^{-2}$	$3.86(13)\times10^{-2}$	$3.15(7)\times10^{-2}$	$2.37(5)\times10^{-2}$
$\|\Psi(r=1a_s)\|^2$	$2.73(6)\times10^{-2}$	$2.00(4)\times10^{-2}$	$1.89(4)\times10^{-2}$	$1.79(6)\times10^{-2}$	$1.50(3)\times10^{-2}$	$1.18(3)\times10^{-2}$
$\|\Psi(r=2a_s)\|^2$	$7.63(14)\times10^{-3}$	$6.61(13)\times10^{-3}$	$6.39(12)\times10^{-3}$	$6.3(2)\times10^{-3}$	$5.63(13)\times10^{-3}$	$4.97(11)\times10^{-3}$
$\|\Psi(r=3a_s)\|^2$	$1.56(4)\times10^{-3}$	$1.96(4)\times10^{-3}$	$2.04(4)\times10^{-3}$	$2.08(6)\times10^{-3}$	$2.00(4)\times10^{-3}$	$2.07(4)\times10^{-3}$
$\|\Psi(r=4a_s)\|^2$	$3.30(20)\times10^{-4}$	$5.8(2)\times10^{-4}$	$6.1(2)\times10^{-4}$	$6.9(3)\times10^{-4}$	$7.2(2)\times10^{-4}$	$8.7(2)\times10^{-4}$
$\|\Psi(r=5a_s)\|^2$	$8.0(20)\times10^{-5}$	$1.8(2)\times10^{-4}$	$1.9(2)\times10^{-4}$	$1.9(3)\times10^{-4}$	$2.9(2)\times10^{-4}$	$3.8(2)\times10^{-4}$
$\|\Psi(r=6a_s)\|^2$	$1.0(20)\times10^{-5}$	$5.0(30)\times10^{-5}$	$6.0(20)\times10^{-5}$	$5.0(40)\times10^{-5}$	$1.4(3)\times10^{-4}$	$1.6(3)\times10^{-4}$
$\langle r^2\rangle^{1/2}$ [fm]	0.3769(135)	0.4508(143)	0.4619(112)	0.4644(194)	0.5240(110)	0.5570(94)

Table 4.4: A table of the vector wave function squared, for each separation, and mass obtained from simultaneous fits of extended-extended correlators, for each temperature.

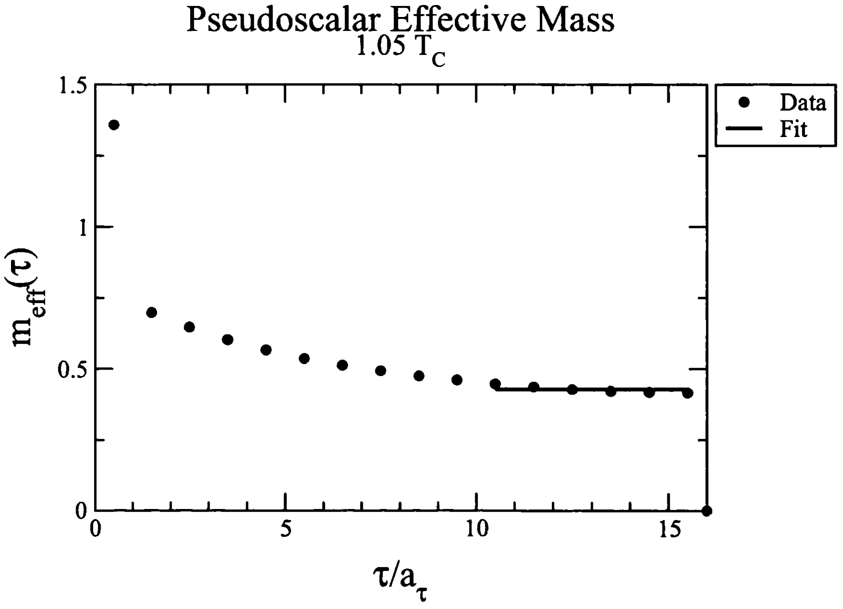

Figure 4.7: The $1.05T_C$ local-local effective mass plot. The fit to a constant was performed for $\tau = 10 - 16$.

course even though the fitting procedure is successful in the extended-extended case this does not mean the presence of higher excited states is not polluting the result.

Figure 4.8 shows the normalized pseudoscalar and vector wave functions squared, obtained from the $1.05T_C$ extended-extended correlators using an eight-parameter fit. In this case the pseudoscalar wave function appears more localized than the vector. This is also seen for other temperatures and can be shown clearly by calculating the root-mean-squared value of the quark separation,

$$\langle r^2 \rangle^{1/2} = \sqrt{4\pi \sum_r r^4 |\Psi(r)|^2}, \tag{4.16}$$

where $\Psi(r)$ is the normalized wave function. The wave function extends across all sites of the lattice volume, but we only obtained values for on-axis quark separations, this is why the factor of $4\pi r^2$ in (4.16) is necessary. The $\langle r^2 \rangle^{1/2}$ values for the pseudoscalar and vector channels are shown at the bottoms of Table 4.3 and Table 4.4 respectively. The $0.42T_C$ $\langle r^2 \rangle^{1/2}$ value obtained for the vector was 0.3769(135)fm, which roughly agrees with the value of 0.47fm obtained using the Cornell potential model [49], and the value of 0.2fm stated in [40] for the binding radius of J/ψ. A pseudoscalar wave function which is more localized than the vector conflicts with the basic intuition that since $M_{\eta_c} < M_{J/\psi}$ the binding radius of η_c should be greater than that of J/ψ. However the pseudoscalar and vector wave functions do not sit in the same potential. If V_{PS} and V_{V} have different forms then the $\langle r^2\rangle^{1/2}$ values can not be compared directly.

Figure 4.9 and Figure 4.10 show the pseudoscalar and vector wave function squared; Figure 4.11 and Figure 4.12 show the natural log of the pseudoscalar and vector wave function squared; and Figure 4.13 and Figure 4.14 show the pseudoscalar and vector $r^2|\psi(r)|^2$ values plotted for each available temperature respectively. As the temperature increases the wave functions become less localized. The $\langle r^2\rangle^{1/2}$ values, shown in Table 4.3 and Table 4.4, also increase with increasing temperature. These results are consistent with the expectation that at high temperature bound states dissociate. In these figures we are seeing the states 'melt'.

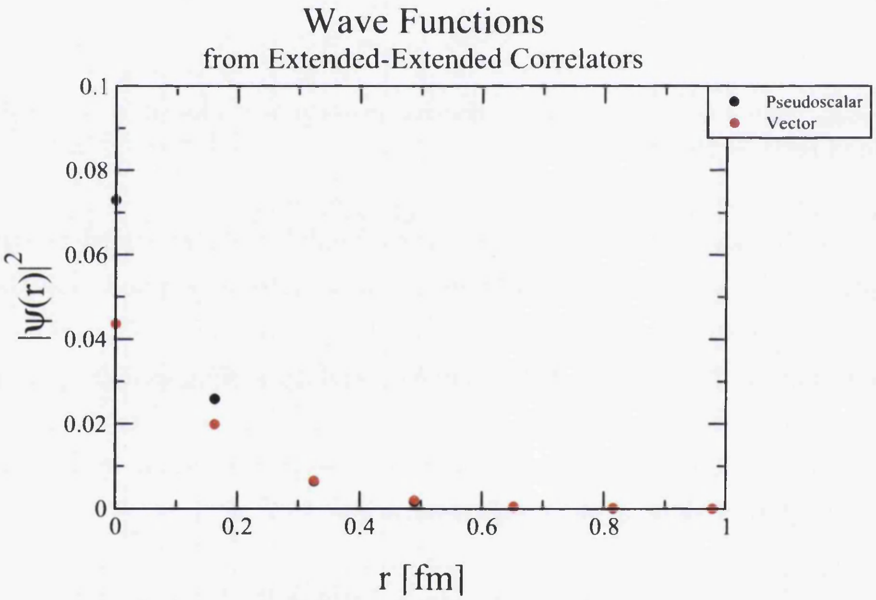

Figure 4.8: The $1.05T_{\text{C}}$ pseudoscalar and vector wave functions squared. Error bars are of the order 10^{-3}.

The pseudoscalar and vector potentials were obtained by evaluating (4.7) for the square root of the $|\psi(r)|^2$ data of Table 4.3 and Table 4.4. These were then combined using (4.12) to give the spin-independent potential, V_{C}. Figure 4.15 shows the spin-independent potential obtained for each temperature. The potentials emerge from the analysis at very different energy levels. The energy of the charmonium system for a particular state is taken equal to the mass of the state. For progressively higher temperatures the pseudoscalar and vector mass values obtained from fits

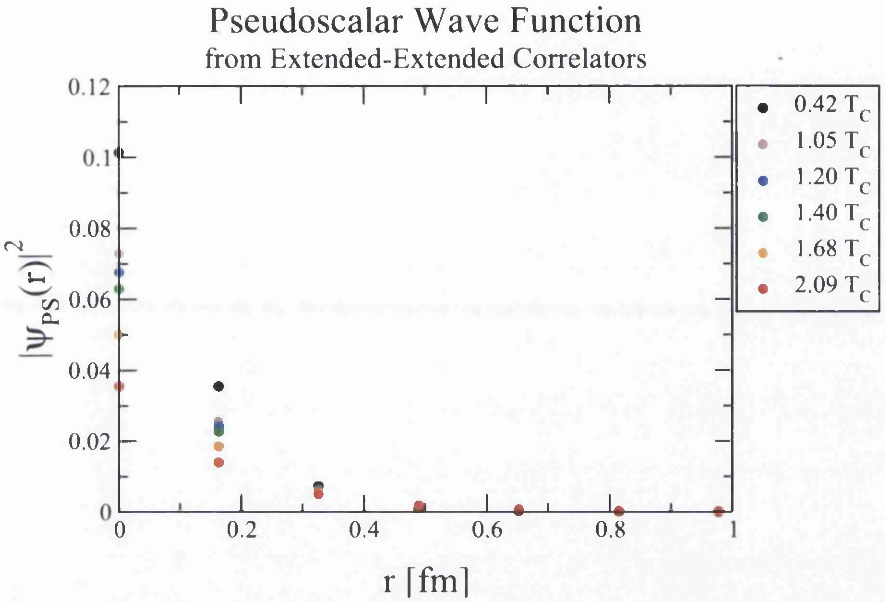

Figure 4.9: The pseudoscalar wave function squared from extended-extended correlators 0.42–2.09T_C. Error bars are of the order 10^{-3} for all temperatures.

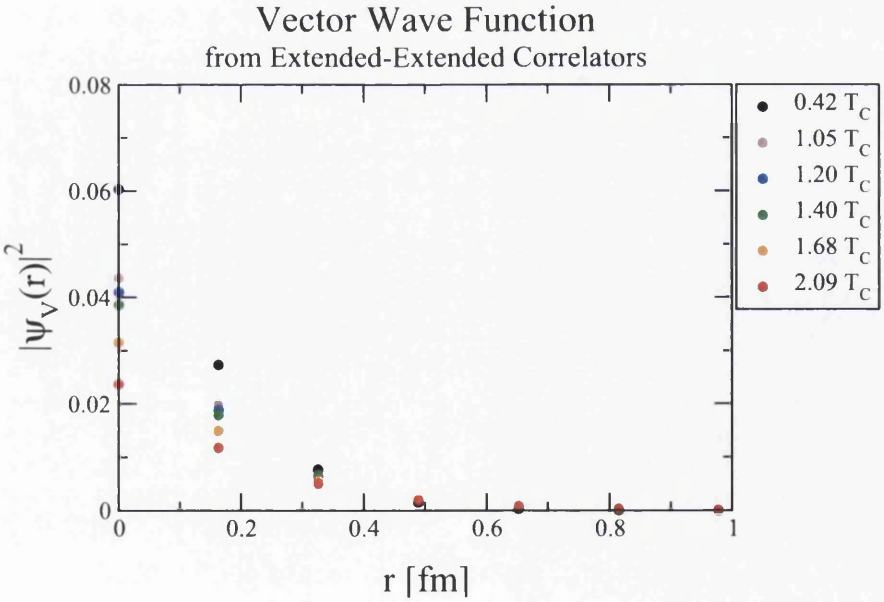

Figure 4.10: The vector wave function squared from extended-extended correlators 0.42–2.09T_C. Error bars are of the order 10^{-3} for all temperatures.

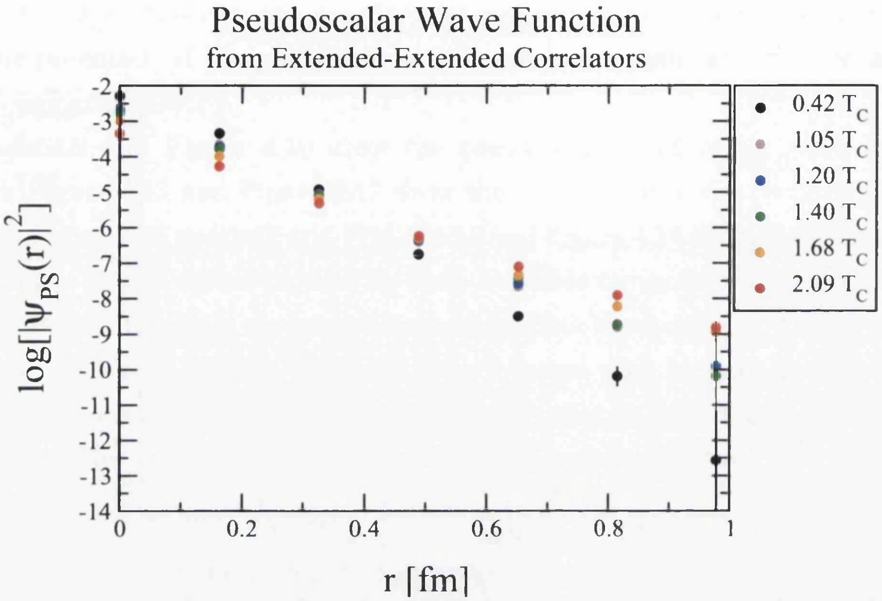

Figure 4.11: The log of the pseudoscalar wave function squared from extended-extended correlators 0.42–2.09T_C.

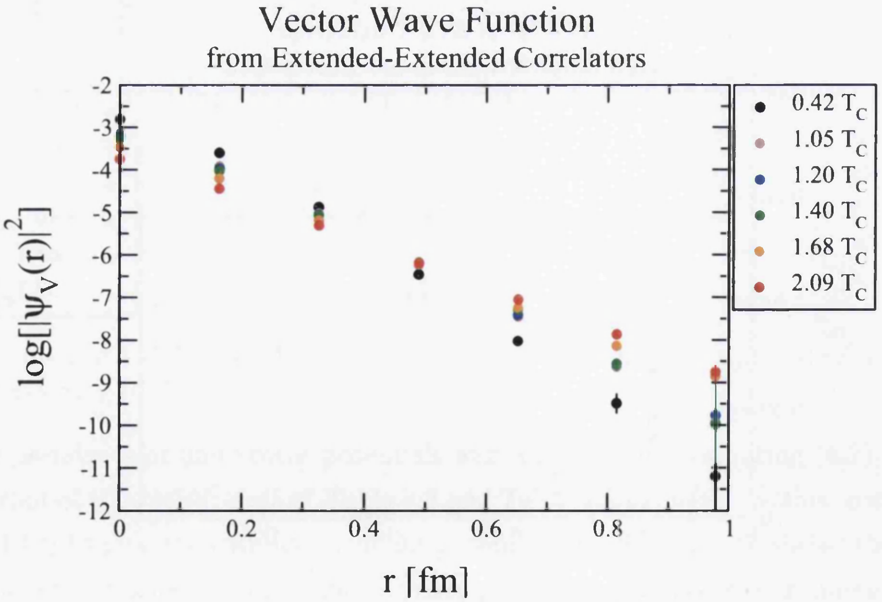

Figure 4.12: The log of the vector wave function squared from extended-extended correlators 0.42–2.09T_C.

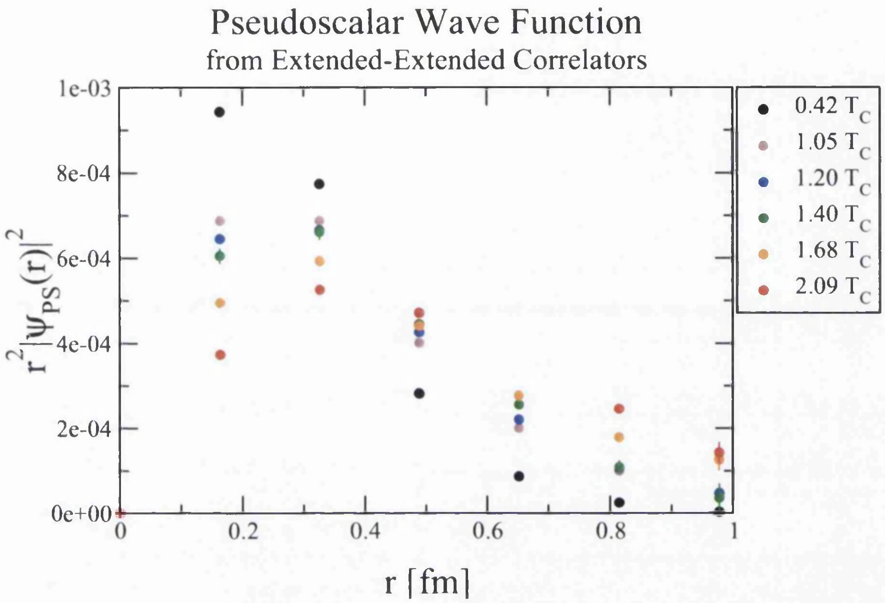

Figure 4.13: The pseudoscalar $r^2|\psi(r)|^2$ values from extended-extended correlators 0.42–2.09T_C.

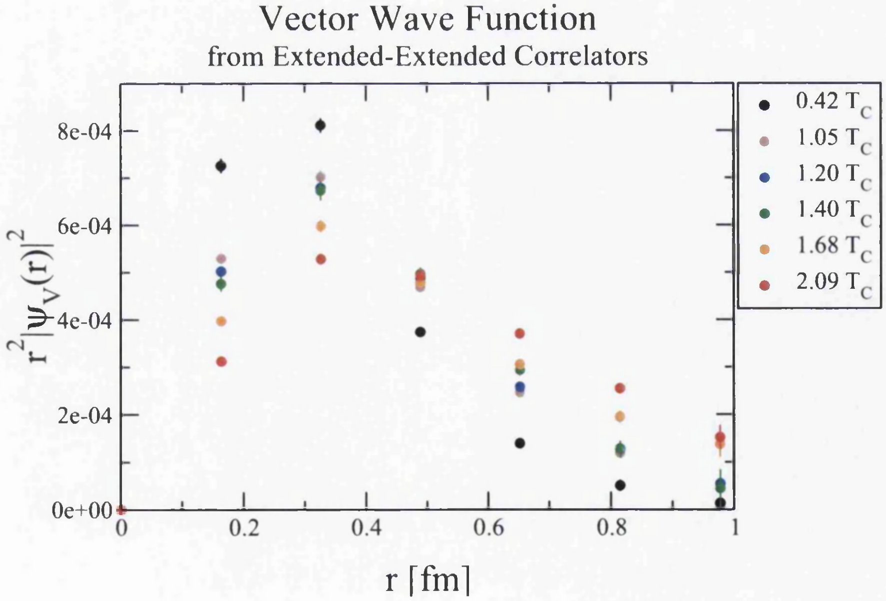

Figure 4.14: The vector $r^2|\psi(r)|^2$ values from extended-extended correlators 0.42–2.09T_C.

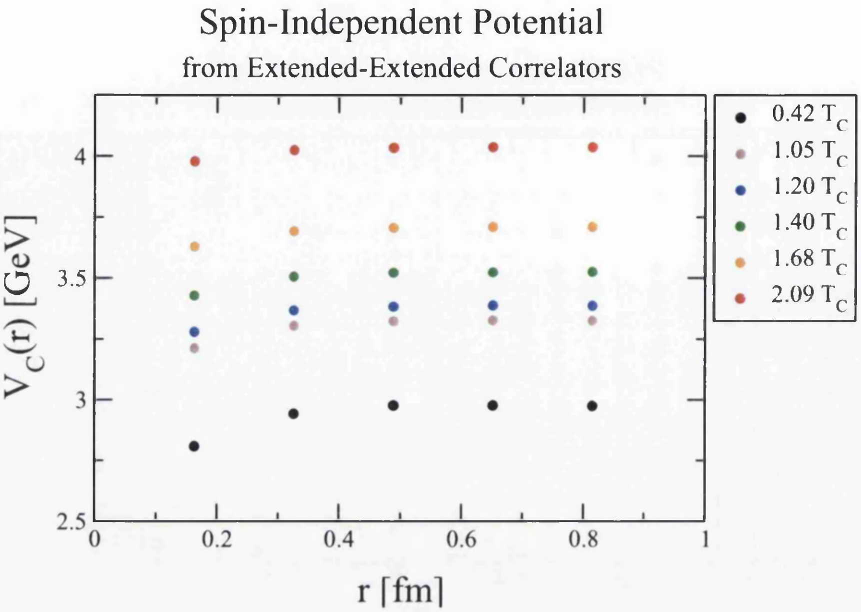

Figure 4.15: The spin-independent potential, $V_C(r)$, plotted for T=0.42–2.09T_C. Error bars are of the order 10^{-3} for all temperatures.

became larger and larger, see Table 4.3 and Table 4.4. As a result the potentials for higher temperatures are shifted up in energy since the energy of the system enters equation (4.7) as constant additive term. In Figure 4.16 the $r/a_s = 1$ data points are shifted vertically to coincide with the $r/a_s = 1$ data point of the $0.42T_C$ potential, to allow a comparison of the form of the potentials. The Cornell potential, see (2.17), is included for reference. The vertical position of the Cornell potential is arbitrary, but constant throughout this thesis. The spin-independent potential shows a clear temperature dependence. As the temperature increases the potential flattens in line with our expectation that the interquark potential becomes colour-Debye screened at high temperature. However in comparison with the Cornell curve the potentials do not have a well-defined 'Coulomb-plus-linear' form, which is cause for concern, especially for the $0.42T_C$ result because the method should be reliable at low temperature. Furthermore at large r the potentials decrease slightly, where at most we would expect the potential to be constant.

The spin-dependent potential, V_S, was calculated using (4.13). The unshifted and shifted spin-dependent potentials are plotted in Figure 4.17 and Figure 4.18 respectively. Once shifted we see the spin-dependent potentials are also temperature dependent. Though this is entirely expected given the spin-independent potential is

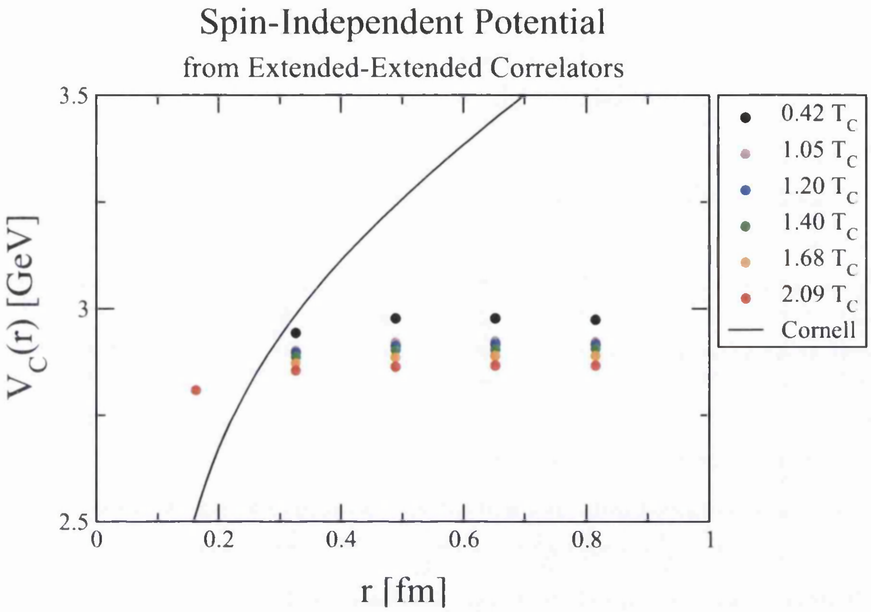

Figure 4.16: The spin-independent potential, $V_C(r)$, plotted for T=0.42–2.09T_C, shifted so that $V_C(r = 1a_s)$ coincides with that of the 0.42T_C curve in Figure 4.15. Error bars are of the order 10^{-2} for all temperatures. The Cornell potential is plotted using (2.17) with $\kappa = 0.52$ and $a = 2.34\text{GeV}^{-1}$.

temperature dependent and both V_S and V_C are built from linear combinations of the same pseudoscalar and vector potentials. i.e. they contain the same information. The spin-dependent potential appears to be repulsive for small r and then become slightly attractive for larger r, while the depth of the minimum decreases with increasing temperature.

4.6 Conclusions

Figure 4.16 provides evidence that the charmonium potential is temperature dependent. As the temperature increases the spin-independent potential flattens, but at large r the potential decreases slightly contrary to expectations. Also, the fact that the form of the 0.42T_C potential, in particular, is not Coulomb-plus-linear is evidence that the method is failing, at least at large r.

Difficulties were encountered when fitting the correlators. These difficulties were due to the correlators containing a contribution from higher excited states even at the largest available τ. In the local-extended case this made fits completely unreliable. In the extended-extended case fits were reliable but the contribution of

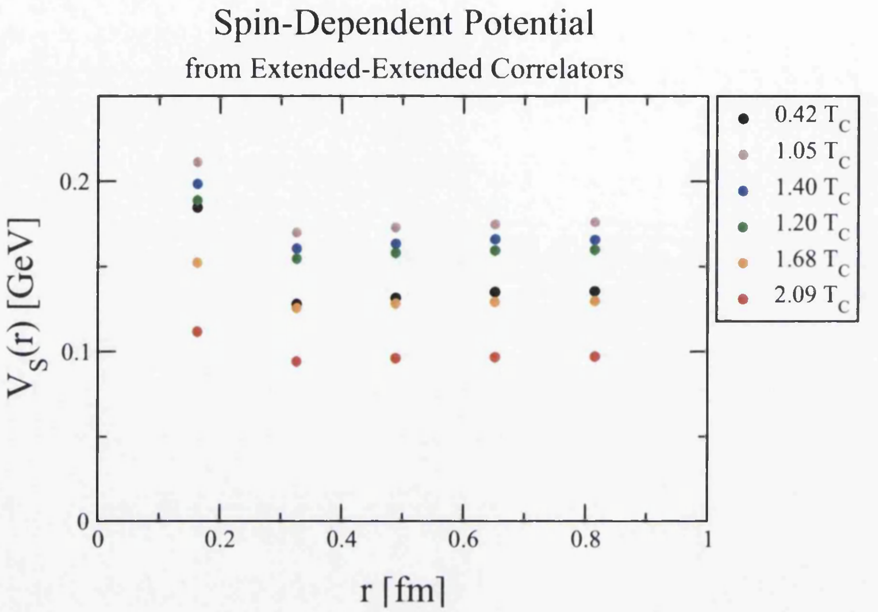

Figure 4.17: The spin-dependent potential, $V_S(r)$, plotted for T=0.42–2.09T_C. Error bars are of the order 10^{-3} for all temperatures.

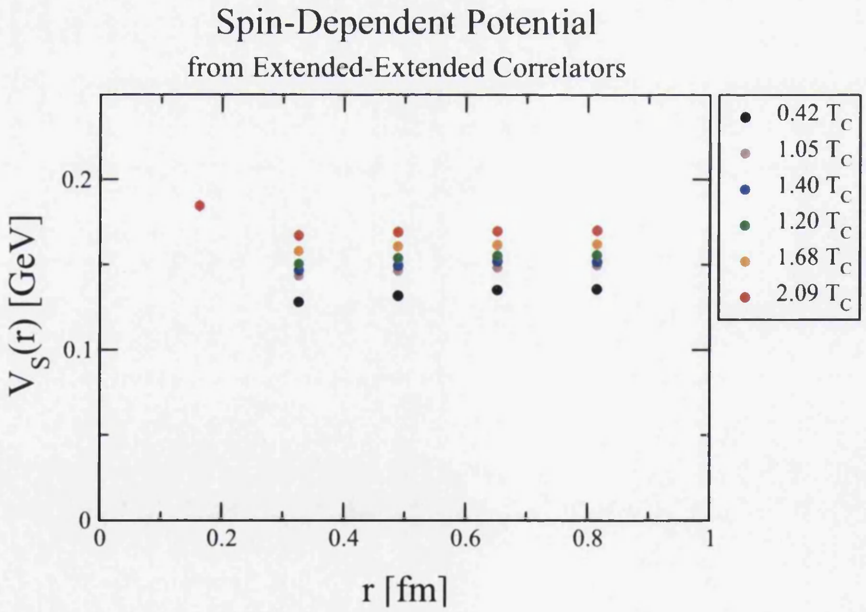

Figure 4.18: The spin-dependent potential, $V_S(r)$, plotted for T=0.42–2.09T_C, shifted so that $V_S(r = 1a_s)$ coincides with that of the 0.42T_C curve in Figure 4.17.

higher excited states to the correlators could not be taken into account, which is a typical problem encountered when working at high temperature. Several alternatives to the eight-parameter fitting function were tested. For example a sixteen-parameter fitting function was attempted with the aim of obtaining values for the ground state and first excited state masses and wave function products. Also attempted was the fixing of certain input parameters in more complicated fitting functions to values obtained from reliable fits to single correlators. None of the alternatives delivered more reliable results than the eight-parameter fit.

We conclude the presence of higher excited states is likely polluting the charmonium potential obtained using conventional fitting techniques. At large r this issue is compounded by the weak signal-to-noise ratio of the correlator. In the future we would like to obtain the charmonium potential for quark separations beyond 1fm. With this in mind it would be difficult to develop the conventional fitting method to calculate the charmonium potential over a larger range of quark separations at a decent resolution. To do this an $N_s/2$-parameter fit would have to be performed to get the ground state mass and wave function products. For $N_s > 12$ this method will only become less reliable. Moreover the contribution of higher excited states at large τ would remain unaccounted for. Consequently it is reasonable to claim the method is limited to extended-extended correlators computed on lattices with $N_s < 12$. In the following chapter we move away from conventional fitting to a method capable of extracting the potential from both moderate and large τ.

Chapter 5

HAL QCD Time-Dependent Approach

An alternative to conventional fitting is provided by the HAL QCD collaboration, which developed a method to obtain nucleon-nucleon potentials directly from correlators [108]. In this chapter, we apply the HAL QCD time-dependent method to the charmonium system to obtain the interquark potential at number of different temperature values.

5.1 HAL QCD Time-Dependent Method

The time-dependent method takes local-extended correlators as input, these are constructed from the creation and annihilation operators introduced in (3.30) and (3.31), which have the form,

$$J_\Gamma(x;\mathbf{r}) = \bar{q}(x)\,\Gamma\,U(x,x+\mathbf{r})\,q(x+\mathbf{r}), \tag{5.1}$$

where $\mathbf{r}$ is the displacement between the quark and anti-quark fields q and $\bar{q}$, x is the space-time point $(\mathbf{x},\tau)$ and Γ is a monomial of gamma matrices used to generate vector (J/ψ) or pseudoscalar (η_c) channels. $U(x,x+\mathbf{r})$ is the gauge connection between x and $x+\mathbf{r}$ required for gauge invariance.

From (3.32) the local-extended charmonium correlator is written,

$$C_\Gamma(\mathbf{r},\tau) = \sum_{\mathbf{x}} \langle J_\Gamma(\mathbf{x},\tau;\mathbf{r})\ J_\Gamma^\dagger(0;\mathbf{0})\rangle, \tag{5.2}$$

where we have neglected the volume term in the denominator of (3.32) since we will be interested in ratios of the correlator in which this term cancels, and the sum over the spatial coordinate at the sink, $\mathbf{x}$, projects the momentum of the state to zero.

From (3.27), (4.1) and (4.2) the local-extended correlator can also be expressed as a sum over the eigenstates of the Hamiltonian, E_j,

$$C_\Gamma(\mathbf{r},\tau) = \sum_j \frac{\psi_j^*(\mathbf{0})\psi_j(\mathbf{r})}{2E_j}\left(e^{-E_j\tau} + e^{-E_j(N_\tau-\tau)}\right), \tag{5.3}$$

where the sum is over the states j with the same Lorentz transformation properties as the operator J_Γ, N_τ is the number of lattice points in the temporal direction, and $\psi_j^*(\mathbf{0})$ and $\psi_j(\mathbf{r})$ are the wave functions at the source and sink as discussed in Section 4.1. We now consider only the forward-moving contribution to the correlator, the effect of ignoring the backward-moving contribution is discussed in Section 5.2,

$$C_\Gamma(\mathbf{r},\tau) = \sum_j \frac{\psi_j^*(\mathbf{0})\psi_j(\mathbf{r})}{2E_j}e^{-E_j\tau} = \sum_j \Psi_j(\mathbf{r})e^{-E_j\tau}, \tag{5.4}$$

where we have defined $\Psi_j(\mathbf{r}) = \psi_j^*(\mathbf{0})\psi_j(\mathbf{r})/2E_j$. The next step is to differentiate both sides with respect to τ,

$$\frac{\partial C_\Gamma(\mathbf{r},\tau)}{\partial\tau} = -\sum_j E_j\Psi_j(\mathbf{r})e^{-E_j\tau}. \tag{5.5}$$

Then, as was done in the conventional fitting approach, we note that $m_c \gg \Lambda_{\mathrm{QCD}}$, and assume $\Psi_j(\mathbf{r})$ obeys the Schrödinger equation,

$$\left(-\frac{\nabla^2}{2\mu} + V_\Gamma(\mathbf{r})\right)\Psi_j(\mathbf{r}) = E_j\Psi_j(\mathbf{r}). \tag{5.6}$$

Substituting $E_j\Psi_j(\mathbf{r})$ in (5.5) for the left-hand side of (5.6) we obtain,

$$\frac{\partial C_\Gamma(\mathbf{r},\tau)}{\partial\tau} = \sum_j \left(\frac{\nabla^2}{2\mu} - V_\Gamma(\mathbf{r})\right)\Psi_j(\mathbf{r})e^{-E_j\tau}. \tag{5.7}$$

We can now note that the terms in the brackets are independent of j and move the sum to the right to obtain,

$$\frac{\partial C_\Gamma(\mathbf{r},\tau)}{\partial\tau} = \left(\frac{\nabla^2}{2\mu} - V_\Gamma(\mathbf{r})\right)C_\Gamma(\mathbf{r},\tau). \tag{5.8}$$

Finally, this can be rearranged to yield the potential,

$$V_\Gamma(\mathbf{r}) = \frac{1}{C_\Gamma(\mathbf{r},\tau)}\left(\frac{\nabla^2}{2\mu} - \frac{\partial}{\partial\tau}\right) C_\Gamma(\mathbf{r},\tau). \tag{5.9}$$

Again, the reduced mass is defined as $\mu = M_V/4$, and (4.9) is used to evaluate the second derivative. The immediate advantage of (5.9) over the conventional fitting method is that the local-extended correlators can be used directly, circumventing the need to rely on unreliable fits for the wave function. As before, the temperature dependence of the potential can be studied by repeating the analysis on ensembles with different temporal extent. Also, it is important to highlight that $V_\Gamma(\mathbf{r})$ has an implicit τ dependence which must be averaged over.

5.2 Accounting for the Backward-Mover

To derive (5.9) the backward-mover was neglected in (5.4). On lattices with a small temporal extent this will become a problem because the correlator data actually has the form,

$$C_\Gamma(\mathbf{r},\tau) = \sum_j \Psi_j(\mathbf{r})\left(e^{-E_j\tau} + e^{-E_j(N_\tau-\tau)}\right). \tag{5.10}$$

Therefore at times around $N_\tau/2$ the forward and backward-moving contributions to the correlator will be equally important and (5.4) will not describe the data with sufficient precision.

At first glance one may suggest simply differentiating (5.10) twice with respect to τ,

$$\frac{\partial^2 C_\Gamma(\mathbf{r},\tau)}{\partial\tau^2} = \sum_j E_j^2 \Psi_j(\mathbf{r})\left(e^{-E_j\tau} + e^{-E_j(N_\tau-\tau)}\right), \tag{5.11}$$

$$= \sum_j \left(-\frac{\nabla^2}{2\mu} + V_\Gamma(\mathbf{r})\right)^2 \Psi_j(\mathbf{r})\left(e^{-E_j\tau} + e^{-E_j(N_\tau-\tau)}\right), \tag{5.12}$$

$$= \left(-\frac{\nabla^2}{2\mu} + V_\Gamma(\mathbf{r})\right)\left(-\frac{\nabla^2}{2\mu} + V_\Gamma(\mathbf{r})\right) C_\Gamma(\mathbf{r},\tau). \tag{5.13}$$

We are then faced with the task of rearranging (5.13) for the potential, but this approach quickly becomes prohibitively complicated due to the quadratic dependence on what is essentially the Hamiltonian operator.

Instead we seek to modify the temporal derivative term of (5.9),

$$\frac{1}{C_\Gamma(\mathbf{r},\tau)}\frac{\partial C_\Gamma(\mathbf{r},\tau)}{\partial\tau}=\frac{-\sum_j E_j\Psi_j(\mathbf{r})e^{-E_j\tau}}{\sum_j \Psi_j(\mathbf{r})e^{-E_j\tau}}=\frac{-(E_0\Psi_0(\mathbf{r})e^{-E_0\tau}+E_1\Psi_1(\mathbf{r})e^{-E_1\tau}+...)}{\Psi_0(\mathbf{r})e^{-E_0\tau}+\Psi_1(\mathbf{r})e^{-E_1\tau}+...}. \tag{5.14}$$

In the large τ limit,

$$\lim_{\tau\to\infty}\frac{1}{C_\Gamma(\mathbf{r},\tau)}\frac{\partial C_\Gamma(\mathbf{r},\tau)}{\partial\tau}=-E_0. \tag{5.15}$$

since $E_0 < E_1 < E_2 \dots$. Therefore to properly describe the correlator data we require a closed form expression in terms of the full correlator expressed in (5.10), which tends to $-E_0$ at large τ. Fortunately, such an expression exists [109]:

$$-\frac{1}{2}\log\left(\frac{C_\Gamma(\tau-1)+\sqrt{C_\Gamma(\tau-1)^2-C_\Gamma(N_\tau/2)^2}}{C_\Gamma(\tau+1)+\sqrt{C_\Gamma(\tau+1)^2-C_\Gamma(N_\tau/2)^2}}\right)=-E_0. \tag{5.16}$$

Replacing the left-hand side of (5.16) for the τ-derivative term in (5.9) we can account for the backward-mover,

$$\begin{aligned}V_\Gamma(\mathbf{r})=\frac{1}{C_\Gamma(\mathbf{r},\tau)}&\left(\frac{\nabla^2 C_\Gamma(\mathbf{r},\tau)}{2\mu}\right)\\&+\frac{1}{2}\log\left(\frac{C_\Gamma(\mathbf{r},\tau-1)+\sqrt{C_\Gamma(\mathbf{r},\tau-1)^2-C_\Gamma(\mathbf{r},N_\tau/2)^2}}{C_\Gamma(\mathbf{r},\tau+1)+\sqrt{C_\Gamma(\mathbf{r},\tau+1)^2-C_\Gamma(\mathbf{r},N_\tau/2)^2}}\right).\end{aligned} \tag{5.17}$$

5.3 Momentum Space Propagators

Local-extended correlators can be obtained more efficiently by working with the quark propagators in momentum rather than coordinate space [110]. For a meson consisting of two arbitrary quarks, q_1 and $\bar{q}_2$, the local-extended correlator can be written,

$$\begin{aligned}C_\Gamma(\mathbf{r},\tau)&=\sum_{\mathbf{x}}\langle 0|\bar{q}_2(\mathbf{x},\tau)\Gamma q_1(\mathbf{x}+\mathbf{r},\tau)\bar{q}_1(\mathbf{0},0)\Gamma^\dagger q_2(\mathbf{0},0)|0\rangle, &(5.18)\\&=-\sum_{\mathbf{x}}\mathrm{Tr}\left[D_{q_1}^{-1}(\mathbf{x}+\mathbf{r},\tau:\mathbf{0},0)\Gamma D_{\bar{q}_2}^{-1}(\mathbf{0},0:\mathbf{x},\tau)\Gamma^\dagger\right], &(5.19)\end{aligned}$$

where the notation for the quark propagators is $D^{-1}(\text{sink}:\text{source})$. Using the Fourier transforms of the quark propagators, which have the form,

$$D^{-1}(\mathbf{y}) = \frac{1}{V}\sum_{\mathbf{q}} \tilde{D}^{-1}(\mathbf{q})e^{i\mathbf{q}\cdot\mathbf{y}}, \tag{5.20}$$

it is possible to write the correlator in terms of $\tilde{D}^{-1}_{q_1}$ and $\tilde{D}^{-1}_{\bar{q}_2}$,

$$\begin{aligned}
C_\Gamma(\mathbf{r},\tau) &= -\sum_{\mathbf{x}} \mathrm{Tr}\left[D^{-1}_{q_1}(\mathbf{x}+\mathbf{r},\tau:\mathbf{0},0)\Gamma D^{-1}_{\bar{q}_2}(\mathbf{0},0:\mathbf{x},\tau)\Gamma^\dagger\right], && (5.21)\\
&= -\sum_{\mathbf{x}}\frac{1}{V^2}\sum_{\mathbf{p},\mathbf{q}} \mathrm{Tr}\left[\tilde{D}^{-1}_{q_1}(\mathbf{p})\Gamma\tilde{D}^{-1}_{\bar{q}_2}(\mathbf{q})\Gamma^\dagger\right] e^{i\mathbf{p}\cdot(\mathbf{x}+\mathbf{r})}e^{i\mathbf{q}\cdot\mathbf{x}}, && (5.22)\\
&= -\frac{1}{V}\sum_{\mathbf{p},\mathbf{q}} \mathrm{Tr}\left[\tilde{D}^{-1}_{q_1}(\mathbf{p})\Gamma\tilde{D}^{-1}_{\bar{q}_2}(\mathbf{q})\Gamma^\dagger\right] \delta_{\mathbf{p}+\mathbf{q},\mathbf{0}}e^{i\mathbf{p}\cdot\mathbf{r}}, && (5.23)\\
&= -\frac{1}{V}\sum_{\mathbf{p}} \mathrm{Tr}\left[\tilde{D}^{-1}_{q_1}(\mathbf{p})\Gamma\tilde{D}^{-1}_{\bar{q}_2}(-\mathbf{p})\Gamma^\dagger\right] e^{i\mathbf{p}\cdot\mathbf{r}}. && (5.24)
\end{aligned}$$

Now using the Fourier transform of the correlator,

$$C_\Gamma(\mathbf{r},\tau) = \frac{1}{V}\sum_{\mathbf{p}} \tilde{C}(\mathbf{p},\tau)e^{i\mathbf{p}\cdot\mathbf{r}}, \tag{5.25}$$

the following relation can be deduced,

$$\tilde{C}_\Gamma(\mathbf{p},\tau) = -\,\mathrm{Tr}\left[\tilde{D}^{-1}_{q_1}(\mathbf{p})\Gamma\tilde{D}^{-1}_{\bar{q}_2}(-\mathbf{p})\Gamma^\dagger\right]. \tag{5.26}$$

This implies that if $\tilde{C}_\Gamma(\mathbf{p},\tau)$ can be obtained, then $C_\Gamma(\mathbf{r},\tau)$ for any value of $\mathbf{r}$ can be computed in straight forward manner by multiplying the product of quark propagators in momentum space with the phase factor $e^{i\mathbf{p}\cdot\mathbf{r}}$. This is computationally more efficient than calculating $C(\mathbf{r},\tau)$ using propagators in coordinate space. In cases where the meson's constituent quarks are the anti-particles of each other, further reductions in cost can be made. The two Fourier transforms, one for each propagator,

$$\tilde{D}^{-1}_{q_1}(\mathbf{p}) = \sum_{x} D^{-1}_{q_1}(\mathbf{x})e^{-i\mathbf{p}\cdot\mathbf{x}} \tag{5.27}$$

$$\tilde{D}^{-1}_{\bar{q}_2}(-\mathbf{p}) = \sum_{x} D^{-1}_{\bar{q}_2}(\mathbf{x})e^{i\mathbf{p}\cdot\mathbf{x}} \tag{5.28}$$

do not both have to be performed. Due to periodic boundary conditions the following relationship holds,

$$-\tilde{D}^{-1}(-\mathbf{p}) = \tilde{D}^{-1}(\mathbf{p}), \tag{5.29}$$

using this expression in combination with γ^5-hermiticity, see (3.46), one propagator can be computed from the other. Furthermore correlators only need to be obtained for positive quark separations, $0 < \mathbf{r} < N_\tau/2$, because the real part of the phase factor $e^{i\mathbf{p}\cdot\mathbf{r}}$ is an even function of $\mathbf{r}$ for fixed $\mathbf{p}$,

$$e^{i\mathbf{p}\cdot\mathbf{r}} = \cos(\mathbf{p}\cdot\mathbf{r}) + i\sin(\mathbf{p}\cdot\mathbf{r}), \tag{5.30}$$

this means the phase factors $e^{i\mathbf{p}\cdot\mathbf{r}}$ and $e^{i\mathbf{p}\cdot(-\mathbf{r})}$ give the same real part of the correlator when (5.25) is applied. The imaginary part of the correlator is not used in the analysis, in any case if it is not identically zero on a configuration by configuration basis, then it can be shown that it is zero for the ensemble average.

The expression for the correlator in (5.18) is not manifestly gauge-invariant. As the propagators are being tied up in momentum space the easiest way to obtain gauge-invariant observables using this technique is to gauge fix rather than include gauge connections.

5.4 $N_f = 2$ Results

The time-dependent method was applied to local-extended correlators obtained from the $N_f = 2$ simulation outlined in Section 4.4. To maintain the gauge-invariance of the observable, link products were not included in quark bi-linears, instead configurations were fixed to the Coulomb gauge beforehand using Chroma. By applying (5.9) to sets of correlators like those shown in Figure 4.5, the pseudoscalar and vector time-slice potentials were obtained. Taken literally (5.9) suggests that the time-slice potentials should be independent of τ. The pseudoscalar time-slice potential at $1.05T_\mathrm{C}$ shown in Figure 5.1 demonstrates that in practice this is not the case. The time-slice potential plots can be split up into three τ ranges: i) for small τ the potential is unstable, here higher excited states and lattice artifacts are still present, the $\tau = 1$ data points do not adhere to the trend because they are calculated using the contact term $C_\Gamma(\mathbf{r} = \mathbf{0}, \tau = 0)$, these data points typically lie outside the axis range used in subsequent time-slice plots; ii) for moderate τ the potential is stable; iii) for large τ the potential data points decrease in unison. In Section 5.2 we anticipated that the backward-mover would become an issue for ensembles with

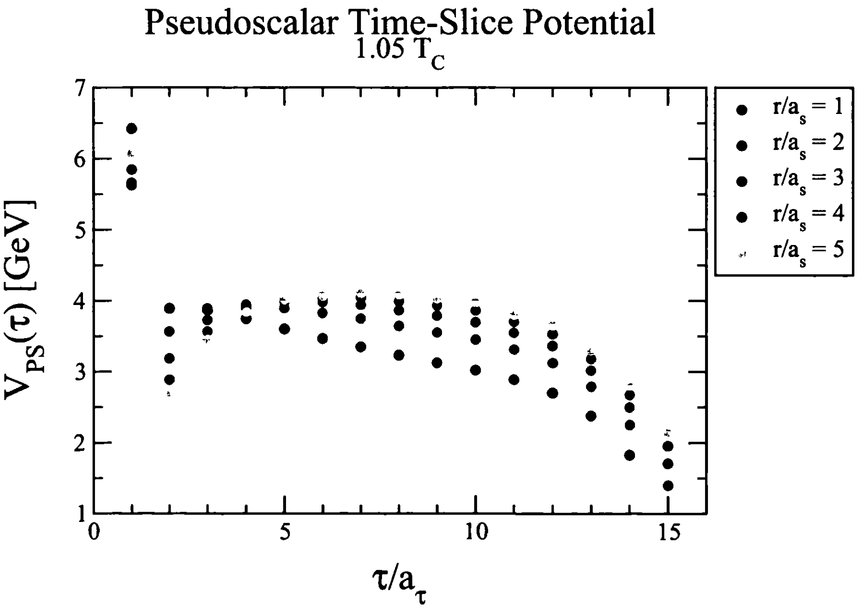

Figure 5.1: $1.05T_C$ ($N_\tau = 32$) pseudoscalar time-slice potential plotted as a function of τ for each quark separation r. Error bars are of the order 10^{-3}.

a small temporal extent. We can now show that it is necessary to use (5.17).

In Figure 5.2 and Figure 5.3 the individual contributions of the spatial and temporal derivative terms in (5.9) to the time-slice potential of Figure 5.1 are shown. At large τ the spatial derivative contribution is stable but the temporal derivative points increase in unison. In Figure 5.4 the term accounting for the backward-mover shown in (5.16) is plotted, comparing this with Figure 5.3 we confirm that the root cause of the large τ behaviour is the backward-mover. Also, as required the substitute temporal term, (5.16), tends towards the negative of the pseudoscalar mass, $\eta_c = 2.9804(1)$GeV [31], at large τ. In Figure 5.5 and Figure 5.6 the pseudoscalar and vector time-slice potentials are plotted using (5.17). In these plots the data points do not decrease in unison at large τ and we conclude that the backward-mover is being accounted for correctly. In all subsequent results (5.17) is used instead of (5.9).

Combining the pseudoscalar (Figure 5.5) and vector (Figure 5.6) time-slice potentials according to (4.12) the spin independent time-slice potential shown in Figure 5.7 is obtained for the $1.05T_C$ ensemble. In the same fashion spin-independent potentials were obtained for all the other ensembles listed in Table 4.2. These plots can be found in Appendix A. Since the spin-independent time-slice potentials fluc-

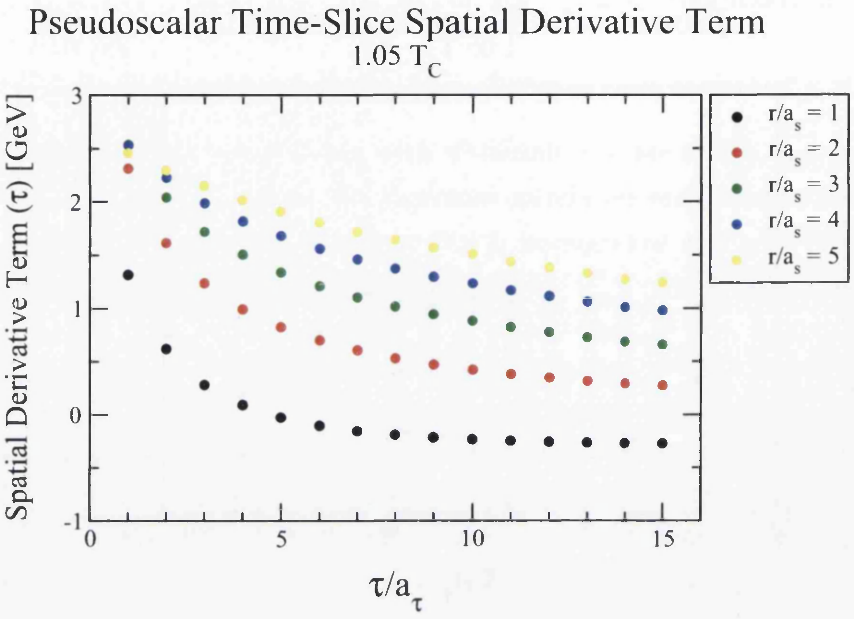

Figure 5.2: The $1.05T_{\mathrm{C}}$ pseudoscalar time-slice spatial derivative term, $(1/C_{\Gamma})(\nabla^2 C_{\Gamma}/2\mu)$, plotted as a function of τ for each quark separation r. Error bars are of the order 10^{-3}.

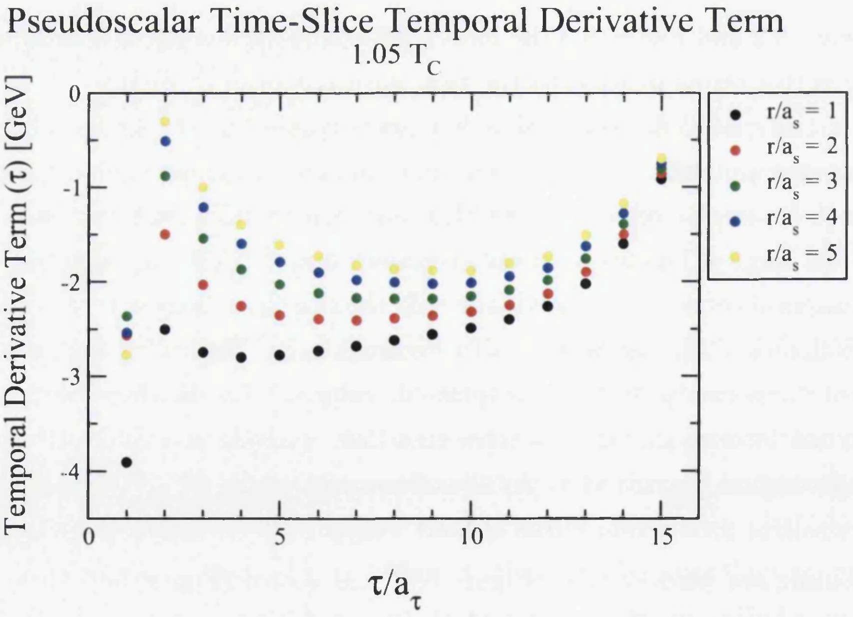

Figure 5.3: The $1.05T_{\mathrm{C}}$ pseudoscalar time-slice temporal derivative term, $(1/C_{\Gamma})(\partial C_{\Gamma}/\partial\tau)$, plotted as a function of τ for each quark separation r. Error bars are of the order 10^{-3}.

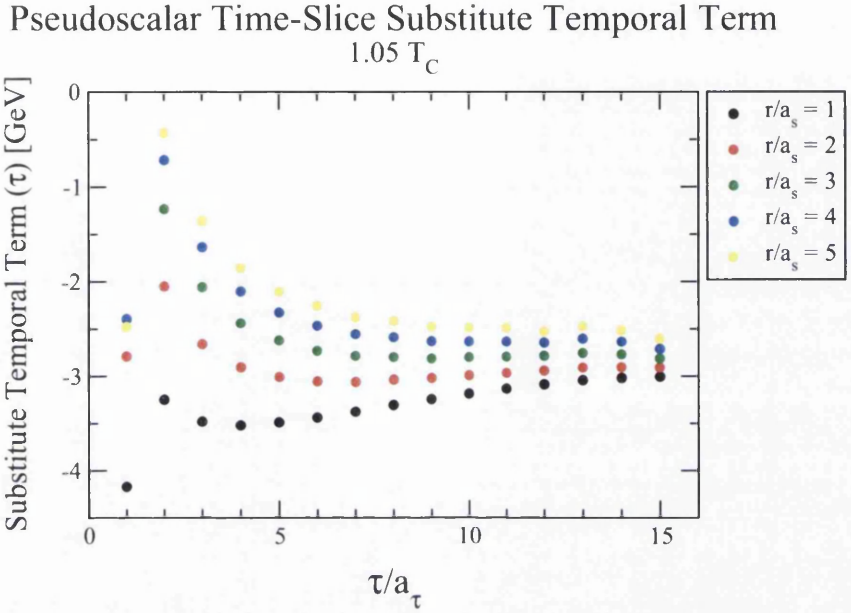

Figure 5.4: The $1.05T_C$ pseudoscalar time-slice substitute temporal term, see (5.16), plotted as a function of τ for each quark separation r. Error bars are of the order 10^{-3}.

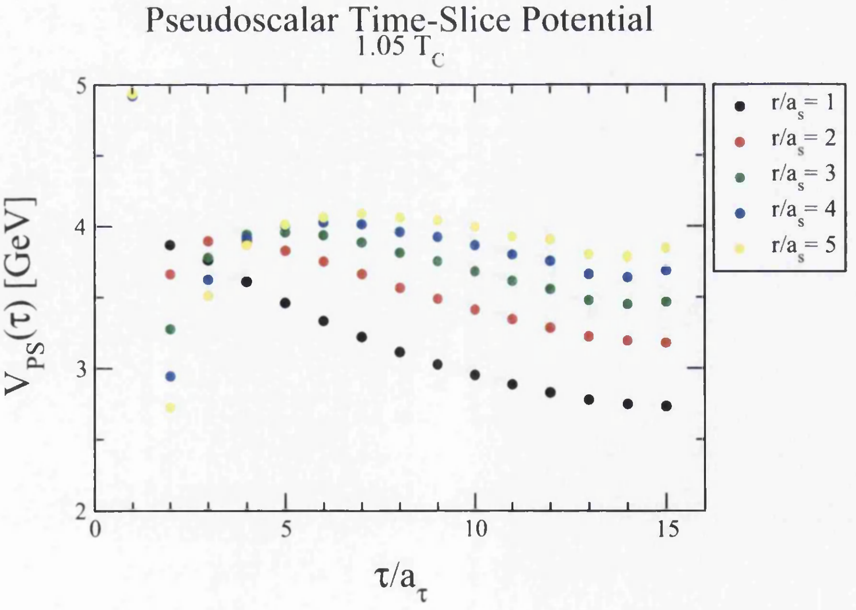

Figure 5.5: The $1.05T_C$ pseudoscalar time-slice potential plotted as a function of τ for each quark separation r, using (5.17). Error bars are of the order 10^{-3}.

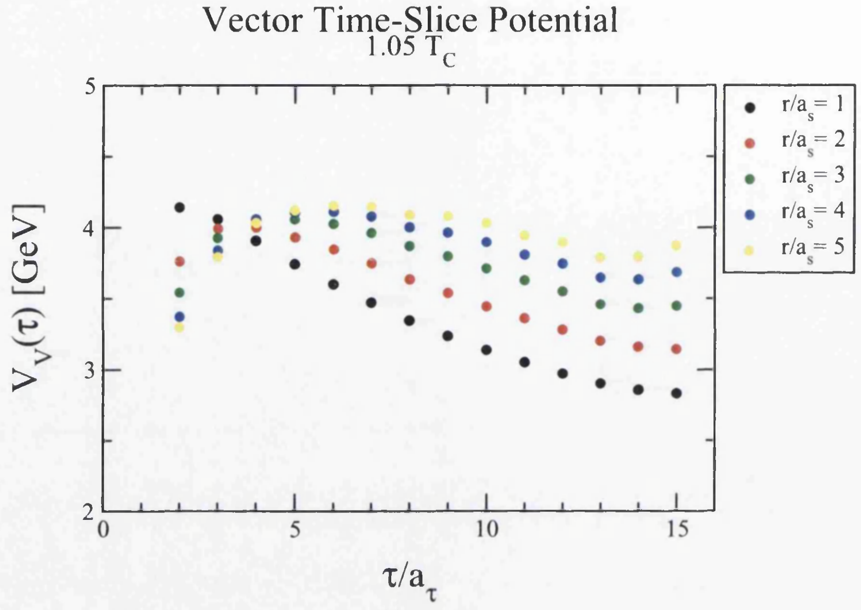

Figure 5.6: $1.05T_C$ vector time-slice potential plotted as a function of τ for each quark separation r, using (5.17). Error bars are of the order 10^{-3}.

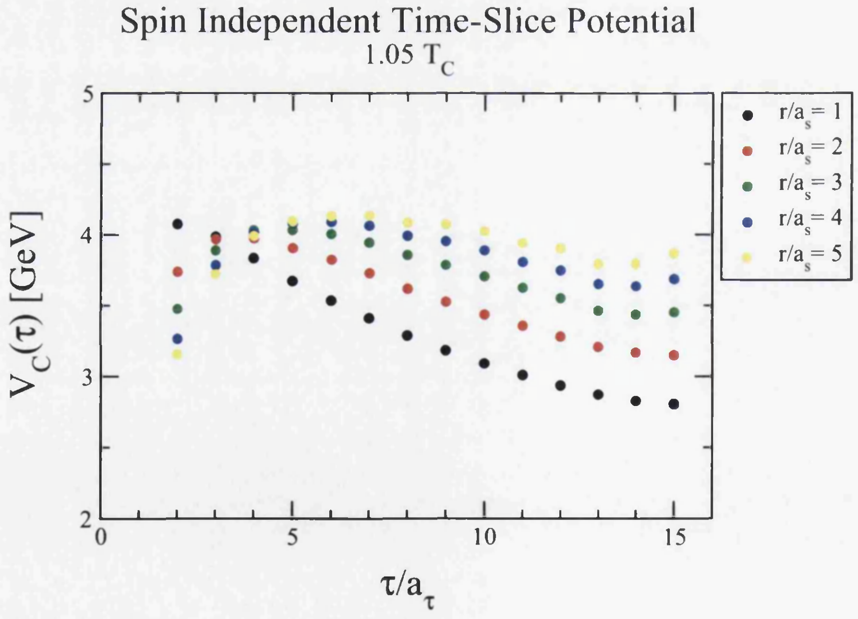

Figure 5.7: $1.05T_C$ spin-independent time-slice potential plotted as a function of τ for each quark separation r. Error bars are of the order 10^{-3}.

N_τ	T $[T_C]$	Central (Upper) Range	Lower Range
80	0.42	$25 - 39$	$12 - 15$
32	1.05	$12 - 15$	$10 - 13$
28	1.20	$10 - 13$	$9 - 11$
24	1.40	$9 - 11$	$7 - 9$
20	1.68	$7 - 9$	N/A
16	2.09	N/A	N/A

Table 5.1: $N_f = 2$ fitting ranges.

tuate time-slice by time-slice, are unstable for small τ and have the familiar high temperature issue of decreasing temporal extent with increasing temperature, the method to extract the potential was given careful consideration. The method chosen was to perform a time-wise correlated fit of the time-slice potential to a constant in a certain τ range for each quark separation. This generates a single value for the potential at each separation r. Ideally we would choose the τ range in which the time-slice data plateaued, but for the higher temperatures the data does not plateau. The next best option was deemed to be to fit the data in the τ ranges shown in the third column of Table 5.1. Potentials were also obtained from the τ ranges shown in the fourth column of the same table, these appear with triangular data points in subsequent plots and allow a fair comparison of potentials with that obtained for the temperature above. The end result of the analysis for the spin-independent potential is plotted in Figure 5.8. We see the potentials are quite spread in energy, the reason for this can be seen by studying the relevant spin-independent time-slice potentials shown in Appendix A. The data in these plots decreases with τ for each separation. For large τ the decrease is in unison and gradual and hence unproblematic, but for small to moderate τ the decrease is more rapid and at a noticeably different rate for each separation. This behaviour is problematic because as the temperature of an ensemble increases its temporal extent decreases and we are forced to fit for the potential between earlier τ values. Therefore the potentials obtained from higher temperature ensembles appear raised in energy. More importantly we must be aware that the data for each separation converges as we move from the largest available τ backwards in time to roughly $\tau/a_\tau = 4$. If we simply fitted the spin-independent time-slice potential of each temperature, say, over the largest four τ values available, then we would observe a flattening of the potential with temperature but this would not be a true temperature effect but a spurious one due to the behaviour of the data with τ. This point can also be seen by imagining the form of the spin-independent potential we would obtain by fitting the $0.42T_{\mathrm{C}}$ ensemble between, say, $\tau = 25 - 39$ and $\tau = 7 - 9$, the latter would be flatter for large r, and thus mimic the flattening we expect due to colour-Debye screening at high temperature. For this reason we emphasize that potentials at different temperatures can only be compared if they were obtained from the same τ range.

To compare the form of the spin-independent potentials in Figure 5.8, the data for each temperature are vertically shifted in Figure 5.9 such that the $r/a_s = 1$ data points coincide with that of the lowest temperature potential. The Cornell potential, see (2.17), is included for reference. The general form of the potential at low temperature agrees well with the zero-temperature literature. The potential clearly curves for small r and straightens for larger r in accordance with the Coulomb-plus-linear form expected from one-gluon exchange being dominant at small r and colour flux tubes developing at large r. In Figure 5.10, for each temperature, the triangular data points of Figure 5.9 are taken as the limit of a single asymmetric error bar originating from the corresponding circular (central) data point. These error bars appear slightly shifted to the right and account for the systematic uncertainty in the analysis. The statistical uncertainty associated with taking the ensemble average appears slightly shifted to the left. Potentials in Figure 5.10 should only be compared with the potential corresponding to the next highest temperature, according to the τ ranges in Table 5.1. Comparisons outside of this criterion are not valid since changes in the potential due temperature can not be separated from those due to τ range choice. Comparing the potentials in the necessary 'staggered' manner we see that between $0.42T_{\mathrm{C}}$ and $1.05T_{\mathrm{C}}$ the potential flattens by an amount greater than the systematic uncertainty. This is in agreement with the expectation that the spin-independent potential should flatten with increasing temperature due to colour-Debye screening. When comparing pairs of potentials higher in temperature the flattening of the potential is no more significant than the systematic uncertainty.

We obtain the spin-dependent time-slice potential for each available temperature by combining the pseudoscalar and vector time-slice potentials according to (4.13). Performing correlated fits on these time-slice potentials, as was done with the spin-independent time-slice plots, gives the spin-dependent potential as a function of quark separation. The end result of the analysis is plotted in Figure 5.11. To compare the form of the potentials more easily the higher temperature potentials are shifted in Figure 5.12 such that the $r/a_s = 1$ data points coincide with that of the lowest temperature potential. In Figure 5.13 the systematic error is included

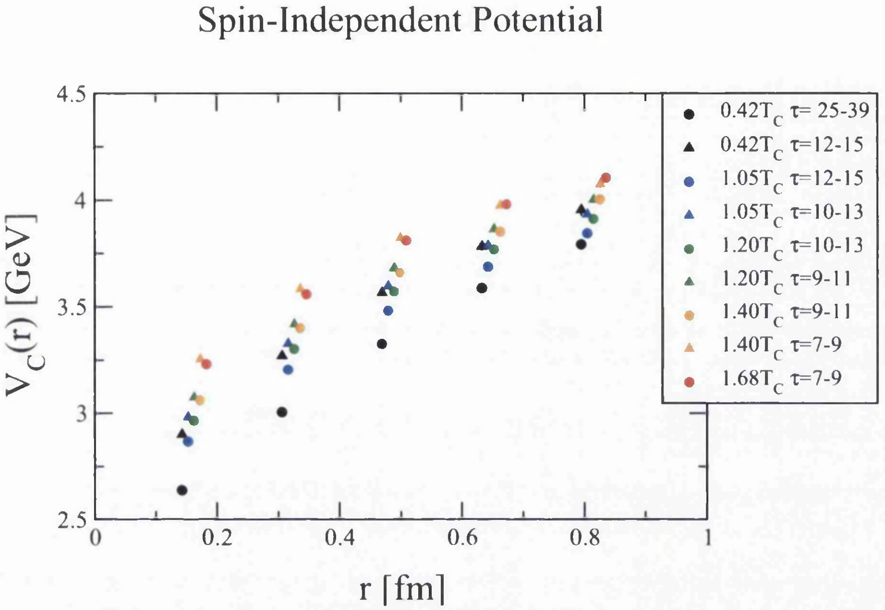

Figure 5.8: The spin-independent potential plotted for temperature range 0.42–$1.68T_C$.

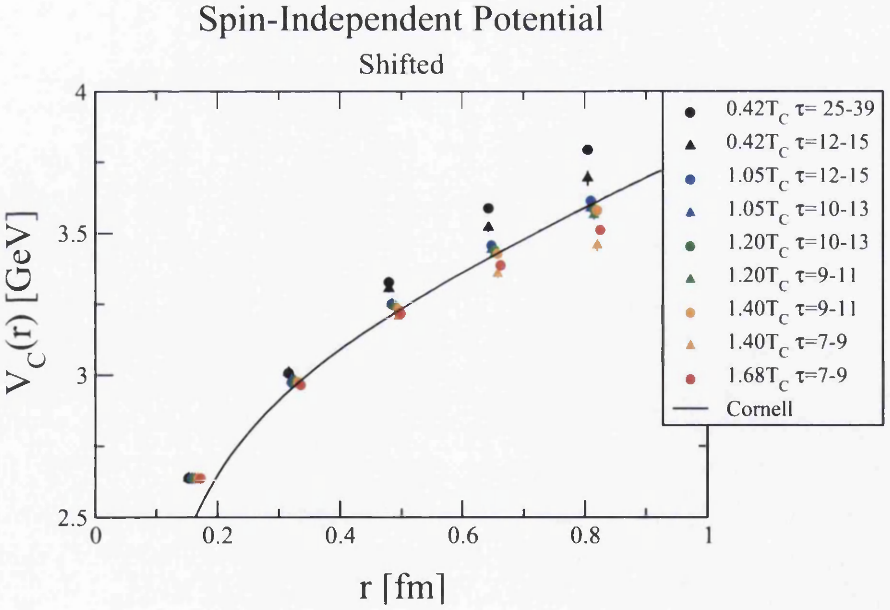

Figure 5.9: The spin-independent potential plotted for temperature range 0.42–$1.68T_C$. The potentials have been shifted vertically so that the $r/a_s = 1$ data points coincide with that of the $0.42T_C$ potential. The Cornell potential is plotted using (2.17) with $\kappa = 0.52$ and $a = 2.34\text{GeV}^{-1}$.

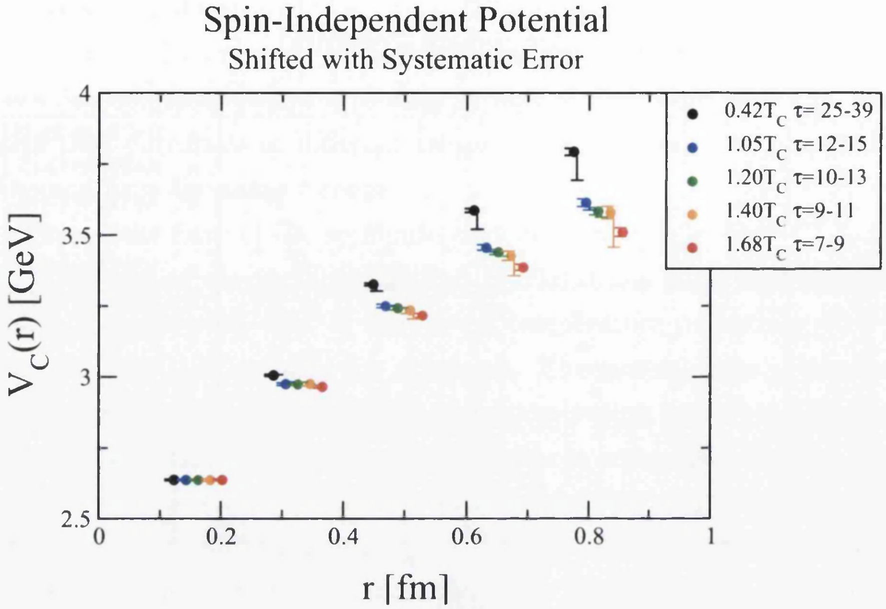

Figure 5.10: The spin-independent potential plotted for temperature range 0.42–1.68T_C. The potentials have been shifted vertically so that the $r/a_s = 1$ data points coincide with that of the 0.42T_C potential. Statistical error bars appear on the left while systematic appear on the right.

using the triangular data points of Figure 5.12 in the same manner as for the spin-independent case. The spin-dependent potential appears to have a repulsive core, flattening out for large separations and becoming attractive. A temperature effect is not deducible since the systematic uncertainty of the potentials is always more significant than the change seen in the potential of the next highest temperature.

In Figure 5.14 the $N_f = 2$ spin-independent potentials from the conventional fitting and time-dependent methods are compared. The results of the two methods do not agree. Therefore one or both of the methods fails to provide the correct result. The time-dependent results agree well with the Cornell potential, in contrast the conventional fitting results really lack a Coulomb-plus-linear form. Doubt is also cast over the conventional fitting results due to the large increase in the mass value with temperature obtained from fitting, see Table 4.3 and Table 4.4. As such we conclude that the time-dependent results are more reliable than the conventional fitting ones.

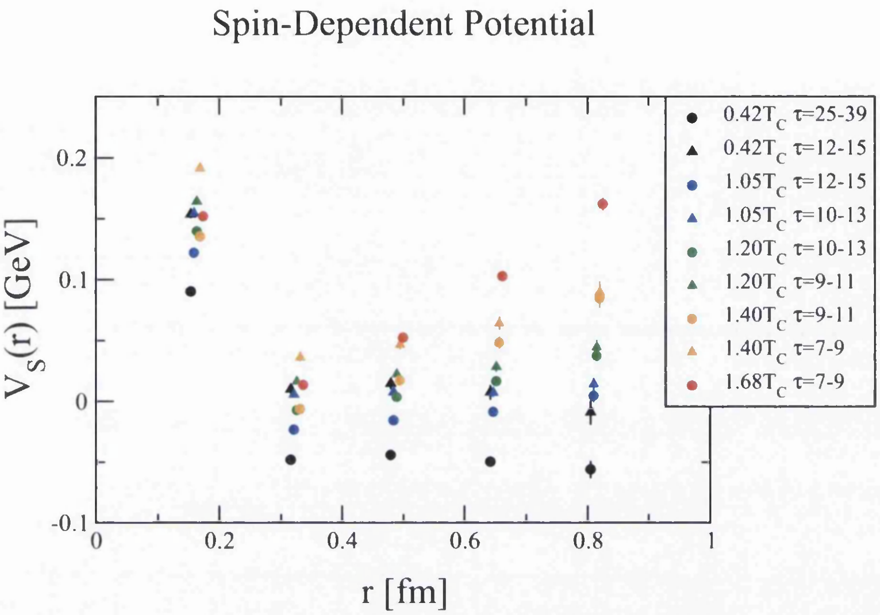

Figure 5.11: The spin-dependent potential plotted for temperature range 0.42–$1.68T_C$.

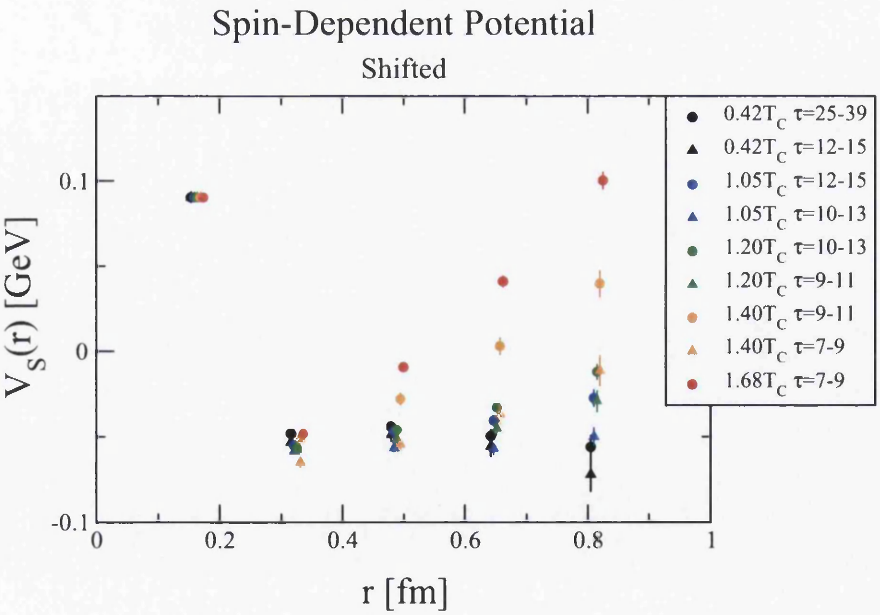

Figure 5.12: The spin-dependent potential plotted for temperature range 0.42–$1.68T_C$. The potentials have been shifted vertically so that the $r/a_s = 1$ data points coincide with that of the $0.42T_C$ potential.

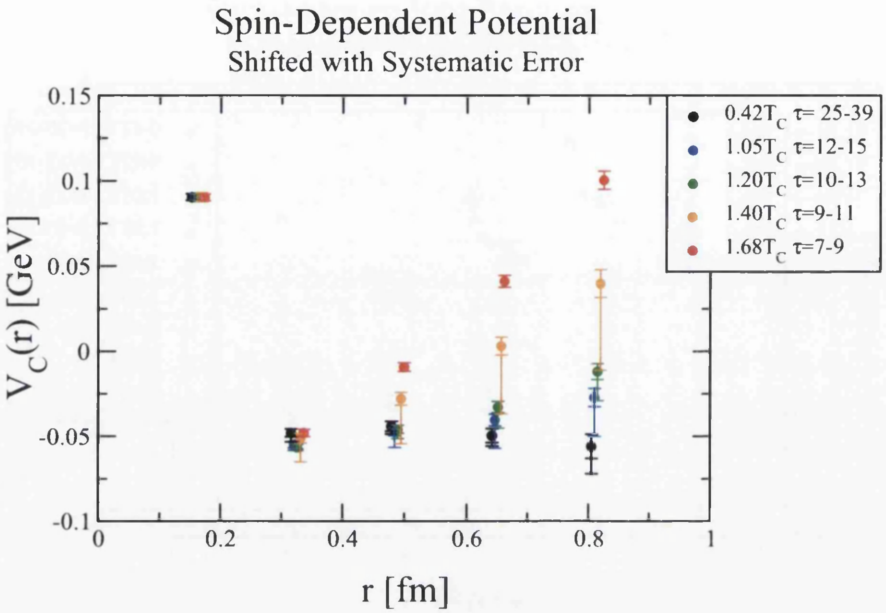

Figure 5.13: The spin-dependent potential plotted for temperature range 0.42–1.68T_C. The potentials have been shifted vertically so that the $r/a_s = 1$ data points coincide with that of the 0.42T_C potential. Statistical error bars appear on the left while systematic appear on the right.

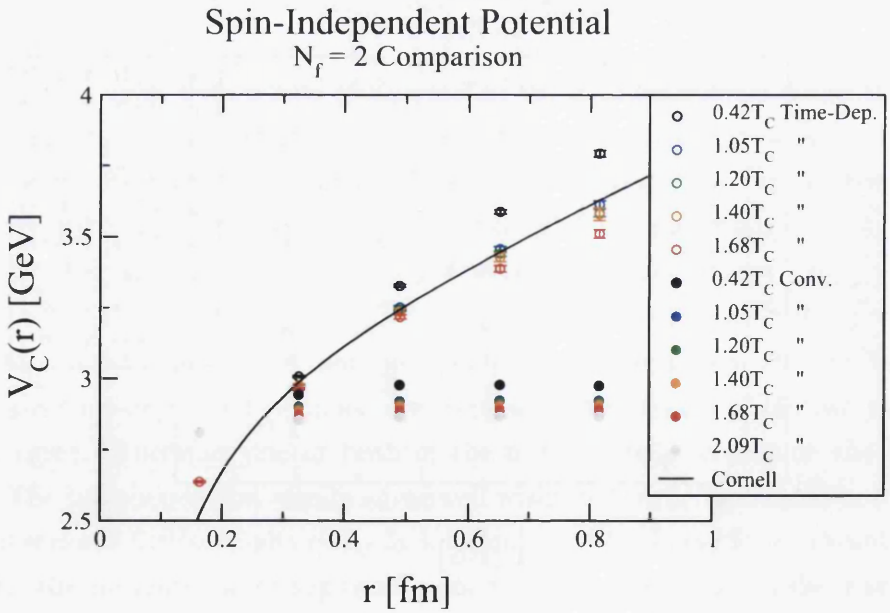

Figure 5.14: A comparison of the spin-independent potential obtained from conventional fitting, Figure 4.16, and the time-dependent method, Figure 5.9.

5.5 $N_f = 2+1$ Simulation Details

We now turn to a calculation of the charmonium potential using lattice ensembles with 2+1 dynamical flavours. The parameters of these ensembles are listed in Table 5.2. The simulation details of [111], repeated here for convenience, were followed exactly to obtain these ensembles:

In the gauge sector a Symanzik improved action was used,

$$S_G^{\xi}[U] = \frac{\beta}{3\xi_0}\left\{\sum_{x,s>s'}\left[\frac{5}{3u_s^4}\mathcal{P}_{ss'} - \frac{1}{12u_s^6}\mathcal{R}_{ss'}\right] + \sum_{x,s}\left[\frac{4}{3u_s^2u_\tau^2}\mathcal{P}_{s\tau} - \frac{1}{12u_s^4u_\tau^2}\mathcal{R}_{s\tau}\right]\right\}, \tag{5.31}$$

where $\mathcal{P}$ is the plaquette, $\mathcal{R}$ is the 2×1 rectangular Wilson loop, the coupling g appears in $\beta = 6/g^2$, ξ_0 is the bare anisotropy, and u_s and u_τ are the spatial and temporal gauge links respectively. This action has leading discretization errors of $\mathcal{O}(\alpha_s^4, a_\tau^2, g^2a_s^2)$.

In the fermion sector we employ an anisotropic clover action,

$$S_F^{\xi}[U,\bar{q},q] = a_s^3 a_\tau \sum_x \bar{q}(x)Qq(x), \tag{5.32}$$

where,

$$Q = \left[m_0 + \nu_\tau W_\tau + \nu_s W_s - \frac{a_s}{2}\left(c_\tau \sigma_{s\tau} G^{s\tau} + \sum_{s<s'} c_s \sigma_{ss'} G^{ss'}\right)\right]. \tag{5.33}$$

m_0 is the mass of the fermion, $\sigma_{\mu\nu} = \frac{1}{2}[\gamma_\mu\gamma_\nu]$, and the Wilson operator, $W_\mu = \nabla_\mu - \frac{a_\mu}{2}\gamma_\mu\Delta_\mu$, where ∇_μ and Δ_μ are the first and second lattice gauge-covariant derivatives respectively, the latter is written in (3.49). In terms of dimensionless variables, $\hat{q} = a_s^{3/2}q$, $\hat{m}_0 = a_\tau m_0$, $\hat{\nabla}_\mu = a_\mu^2\nabla$, $\hat{\Delta}_\mu = a_\mu\Delta$, $\hat{G}_{\mu\nu} = a_\mu a_\nu G_{\mu\nu}$ and the dimensionless 'Wilson operator', $\hat{W}_\mu \equiv \hat{\nabla}_\mu - \frac{1}{2}\gamma_\mu\hat{\Delta}_\mu$, the fermion matrix Q becomes,

$$Q = \left[a_\tau \hat{m}_0 + \nu_\tau \hat{W}_\tau + \nu_s \hat{W}_s - \frac{1}{2}\left(c_\tau \sigma_{s\tau}\hat{G}^{s\tau} + \sum_{s<s'} c_s \sigma_{ss'}\hat{G}^{ss'}\right)\right]. \tag{5.34}$$

From the field redefinition [112, 113], there is one redundant coefficient: either ν_τ or ν_s. There are two common choices to eliminate this redundancy: setting $\nu_s = 1$ (ν_τ-tuning) or $\nu_\tau = 1$ (ν_s-tuning). In this work ν_τ is set to unity and we define

N_s	N_τ	T(MeV)	T/T_c	N_{cfg}
24	128	'Zero'	'Zero'	250
24	40	141	0.76	500
24	36	156	0.84	500
24	32	176	0.95	1000
24	28	201	1.09	1000
24	24	235	1.27	1000
24	20	281	1.52	1000
24	16	352	1.90	1000
32	32	176	0.95	500
32	24	235	1.27	500

Table 5.2: The table shows the lattice size, (N_s, N_τ), the corresponding temperature, T, in units of MeV and T_C, and the number of configurations in each ensemble, N_{cfg}.

$\nu = \nu_s$. Then c_s and c_τ have the tree-level tadpole-improved values,

$$c_s = \frac{\nu}{\tilde{u}_s^3}, \quad c_\tau = \frac{1}{2}\left(\nu + \frac{1}{\xi}\right)\frac{1}{\tilde{u}_\tau \tilde{u}_s^2}, \tag{5.35}$$

where $\tilde{u}_s$ and $\tilde{u}_\tau$ are the spatial and temporal tadpole factors respectively, appearing with tildes to differentiate them from their gauge sector counterparts. The fraction $a_\tau/a_s = 1/\xi$ is set to the desired renormalized gauge anisotropy. In this work the gauge links in the fermion action are 3-dimensionally stout-link smeared gauge fields, see Section 3.7.

Configurations were sampled using the RHMC algorithm. The temporal and spatial lattice spacings were measured to be $a_s \simeq 0.123$fm and $a_\tau^{-1} \simeq 5.63$GeV, giving an anisotropy of $\xi = a_s/a_\tau \approx 3.5$. T_C was calculated from the inflection point of the renormalized Polyakov loop. Before measurement the configurations were fixed to the Coulomb gauge. A Fourier-accelerated gauge-fixing procedure several times faster than Chroma's in-house gauge-fixing routine was used, the details of which can be found in [114].

Charmonium correlators were calculated using a mass parameter set by tuning the pseudoscalar effective mass to the experimental η_c value at zero temperature [81]. A bespoke program written in C++ and QDP++ was used to Fourier transform coordinate-space propagators obtained from Chroma to momentum-space and to subsequently calculate correlators according to the equations outlined in Section 5.3.

The computing resources were provided by HPC Wales. The Cardiff HTC cluster,

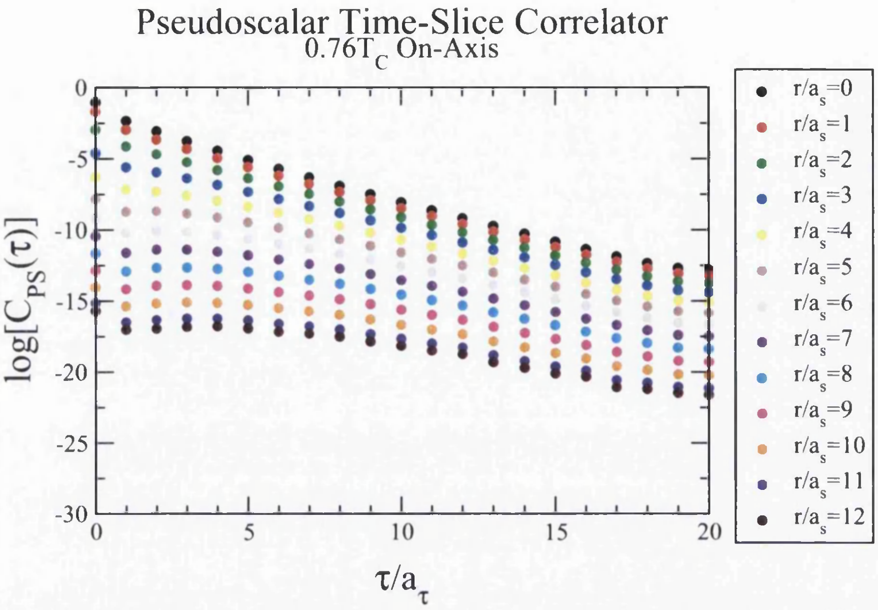

Figure 5.15: Local-extended charmonium correlators for all possible on-axis separations of the $0.76T_C$ ensemble.

consisting of 162 dual processor nodes, each having two six-core Intel Westmere Xeon X5650 2.67 GHz CPUs and 36GB of memory, was used.

5.6 $N_f = 2 + 1$ Results

Local-extended correlators corresponding to on-axis, face-diagonal and body-diagonal quark separations from the simulation outlined in Section 5.5 were obtained. Correlators corresponding to quark separations of the same magnitude were then averaged to give a set of 37 correlators, corresponding to the 37 separations of unique magnitude. The set of correlators for the $0.76T_C$ ensemble is shown in Figure 5.15, Figure 5.16 and Figure 5.17, separated into on-axis, face-diagonal and body-diagonal subsets. The local-local ($r/a_s = 0$) correlator is included in all three plots for reference. As one would expect the magnitude of the correlator signal varies inversely with the quark separation at the sink.

A significant benefit of working with the propagators in momentum space is the ease with which the local-extended correlators corresponding to off-axes separations can be computed. The speed of working solely in coordinate space with Chroma, versus working in momentum space with a bespoke Chroma/QDP++/C++ program, was compared on a 32^4 ($N_\tau = 32$, $N_s = 32$) lattice. The fermion matrix inversion is

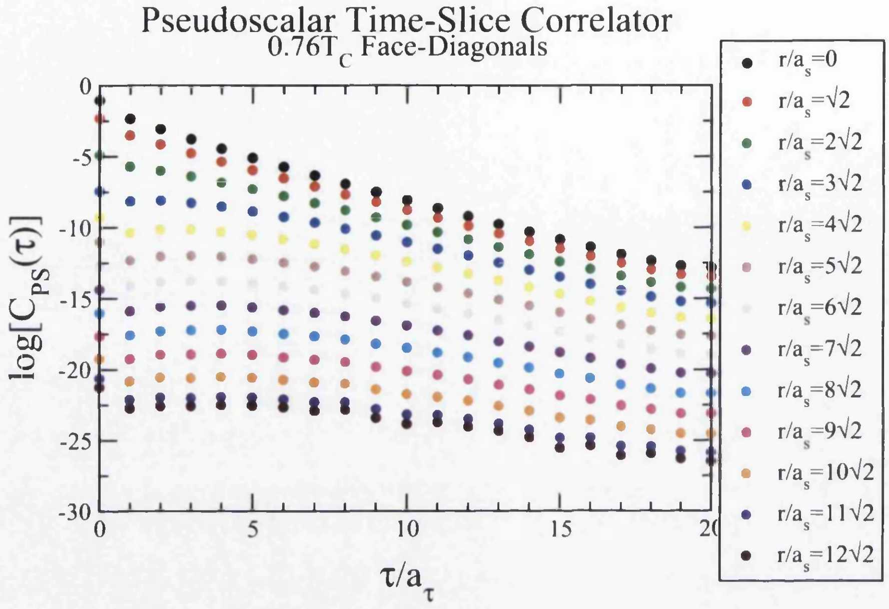

Figure 5.16: Local-extended charmonium correlators for all possible face-diagonal separations of the $0.76T_C$ ensemble.

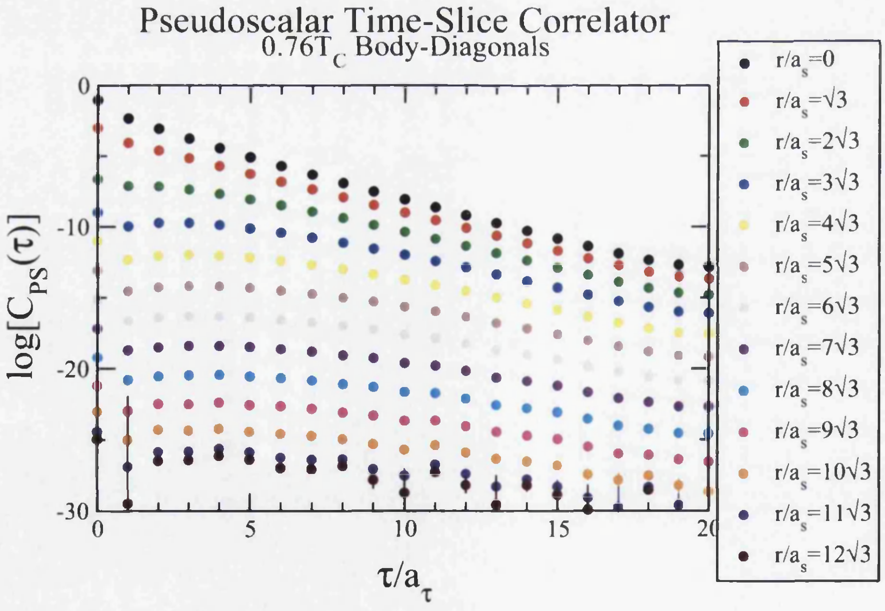

Figure 5.17: Local-extended charmonium correlators for all possible body-diagonal separations of the $0.76T_C$ ensemble.

an overhead common to both methods; a single lattice propagator was obtained in roughly 20720 core-seconds in each case, on 32 cores this takes about ten minutes. However, correlators were obtained faster using the momentum rather than coordinate space method. In each case the sixteen correlators corresponding to the sixteen possible γ-matrices were obtained for a total of 49 different quark separations — the 49 on-axis separations. In coordinate space using Chroma this took roughly 11780 core-seconds for each configuration; in momentum space using the bespoke program this took roughly 7890 core-seconds. On 32 cores this equates to roughly six and four minutes respectively. Therefore on a 32^4 lattice correlators are obtained using 33% fewer core-hours with the momentum space method. Taking into account the common overhead the saving is more modest, sixteen down to fourteen minutes, which represents a saving of approximately 12.5%. A saving of similar magnitude is observed on all lattice sizes, but will naturally increase with the lattice volume.

Local-extended correlators with quark separations along face- and body-diagonals provide potential data points at multiples of $a_s\sqrt{2}$ and $a_s\sqrt{3}$ respectively. It was hoped this would offer a way to interpolate potential data points from on-axis quark separations. However potentials calculated from correlators corresponding to on-axis, face-diagonal and body-diagonal type quark separations form distinct curves rather than interpolating each other. To demonstrate this behaviour the $0.76T_C$ pseudoscalar potential is shown in Figure 5.18 with the potential points for on-axis, face-diagonal and body-diagonal quark separations shown in different colours. The potential was calculated using (5.17), and here a time-wise correlated fit to a constant was performed on the on-axis, face-diagonal and body-diagonal time-slice potentials for each separation for $\tau = 15 - 19$. To better understand the behaviour exhibited in this plot the spatial and temporal derivative terms are plotted separately in Figure 5.19 and Figure 5.20 respectively. The spatial derivative term separates into three distinct curves depending on the type of separation. At large r the face- and body-diagonal data points decrease sharply, this behaviour is likely a finite volume effect. The temporal derivative term does not separate so distinctly into three curves. For values of r greater than 1.5fm the body data points diverge from the trend set by the on-axis and face-diagonal data points, but this behaviour is more than likely simply due to the correlator signal becoming very small, as one can see the errors on the body-diagonal data points become very large. We conclude the separation of the potential into three distinct curves could be due to one or both of the following issues: i) in the evaluation of the spatial derivative term a different lattice spacing appears in the denominator of the finite difference operator

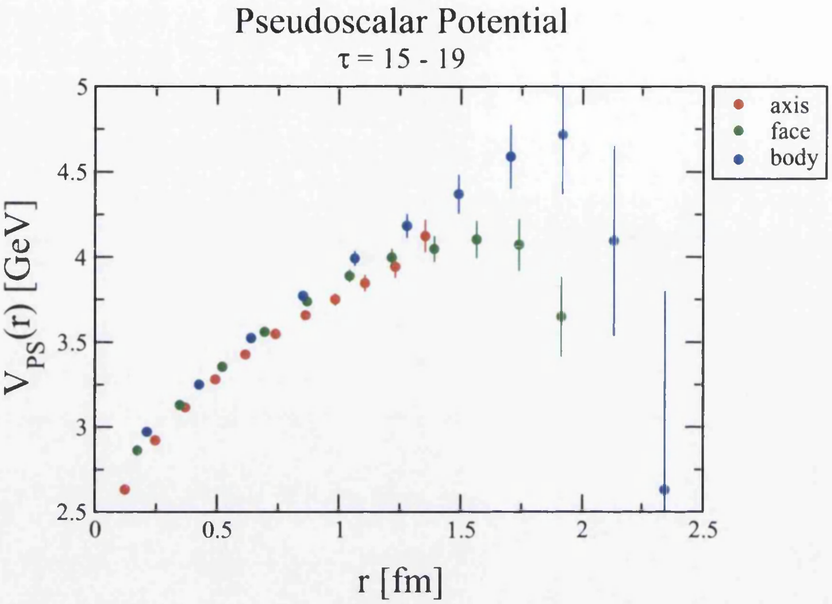

Figure 5.18: The $0.76T_C$ pseudoscalar potential for $\tau = 15 - 19$.

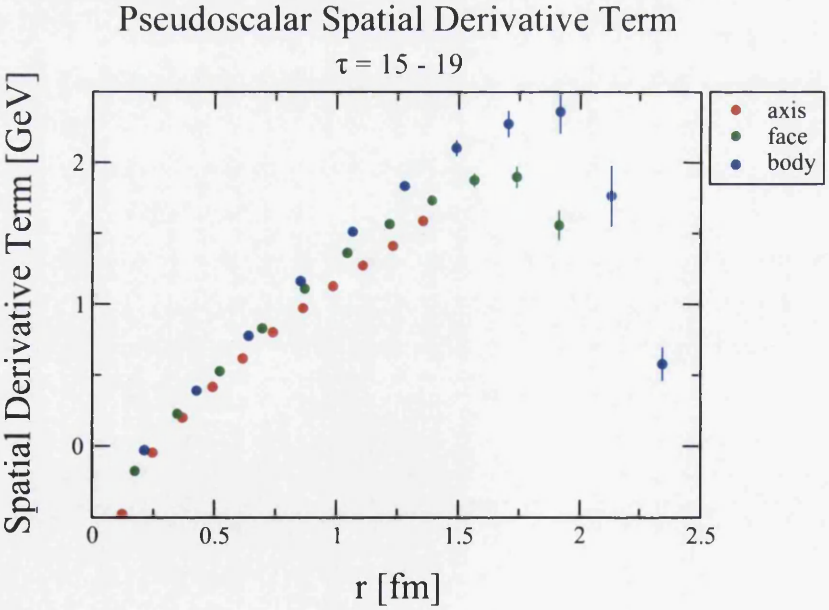

Figure 5.19: The $0.76T_C$ pseudoscalar spatial derivative term, $(1/C_\Gamma)(\nabla^2 C_\Gamma/2\mu)$, for $\tau = 15 - 19$.

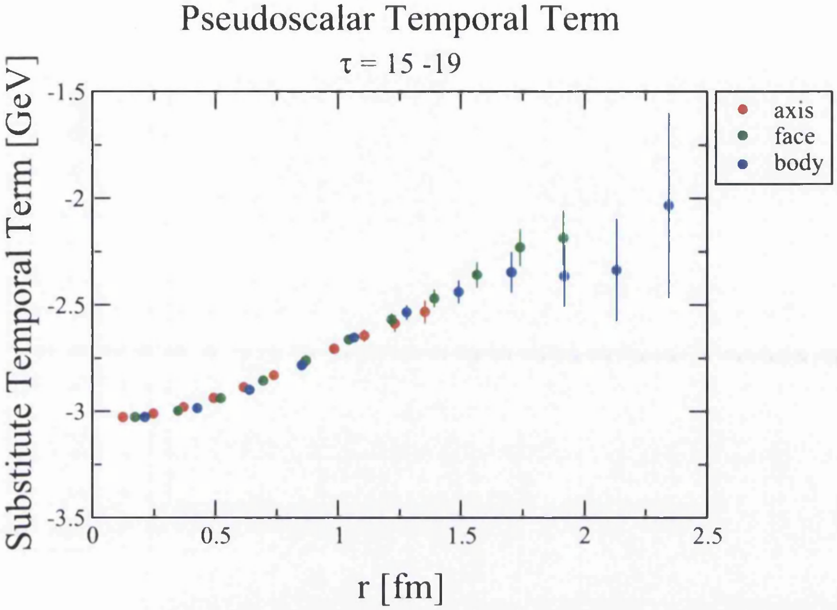

Figure 5.20: The $0.76T_C$ substitute temporal term, (5.16), for $\tau = 15 - 19$.

for each type of separation, $a_s \to a_s\sqrt{2}$ and $a_s \to a_s\sqrt{3}$, for face- and body-diagonal separations respectively. Effectively, the spatial lattice spacing, a_s, is the interval with which the dependence of the correlator on r is being sampled. Since this is relatively coarse to begin with, sampling the correlator at $a_s\sqrt{2}$ and $a_s\sqrt{3}$ in the face- and body-diagonal cases results in a data set with a slightly different form, this difference is amplified when the second derivative is taken; ii) contributions to the correlator due to the charmonium wave function spreading around the compact spatial dimensions add in a non-trivial manner, which could also be complicated by the discrete nature of the lattice.

There is no solution to i) that doesn't involve generating new configurations but a first thought towards solving problem ii) might be to derive a spatial version of (5.16). However unlike in the temporal case the functional form of the unaccounted contribution is unknown and actually the very quantity we are trying to calculate — the wave function. Another possibility is that the issue is a result of using spherical coordinates where Cartesian would be most appropriate. In any case, we do not use results from the correlators with face- or body-diagonal quark separations, deciding that the potentials obtained with the 'finest' lattice spacing should be the most accurate.

The $N_s = 32$ ensembles, listed in Table 5.2, provided a means to investigate the

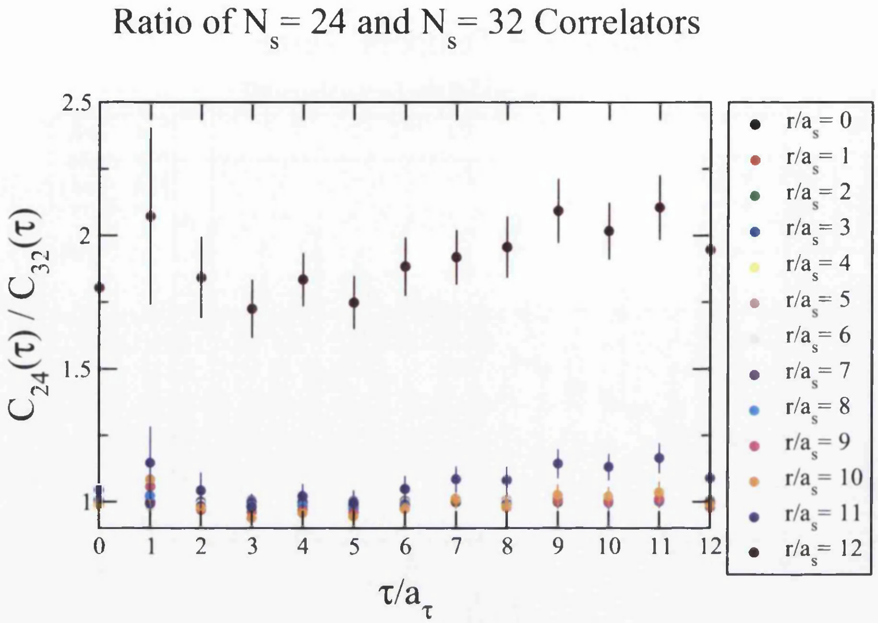

Figure 5.21: Ratio of local-extended correlation functions computed over lattices with $N_s = 24$ and $N_s = 32$. $N_\tau = 24$ for both lattices.

volume dependence of the correlators, and hence also that of the potentials. Figure 5.21 shows the result of taking the ratio of local-extended correlators computed over ensembles with $N_s = 24$ and $N_s = 32$, and $N_\tau = 24$ in both cases. There is no significant volume dependence for $r/a_s = 0$–9. This can be seen by studying Figure 5.21 and Figure 5.22. For $r/a_s = 10$–12, the ratio clearly deviates from unity with increasing severity. From this volume study we conclude there is no overall volume dependence, but the local-extended correlators with $r/a_s = 10$–12 are compromised by the use of periodic boundary conditions. This effect is similar to the issue regarding the temporal backward-mover in that it is due to the correlation at a space-time point on the lattice having contributions that travel opposite ways around a compact dimension. Again at first glance it may seem that we can account for this by deriving a spatial version of (5.16), but the key difference is the form of the functions depending on τ were known, in (5.3) these are the two exponential terms inside the parentheses. In this case we would need to know the form of the function we are essentially trying to calculate — the wave function. Consequently the potential values, $V_\Gamma(r/a_s = 9$–$11)$, are excluded from the results.

The pseudoscalar and vector time-slice potentials shown in Figure 5.23 and Figure 5.24 were obtained by applying (5.17) to the $0.76T_C$ on-axis correlators. Combining

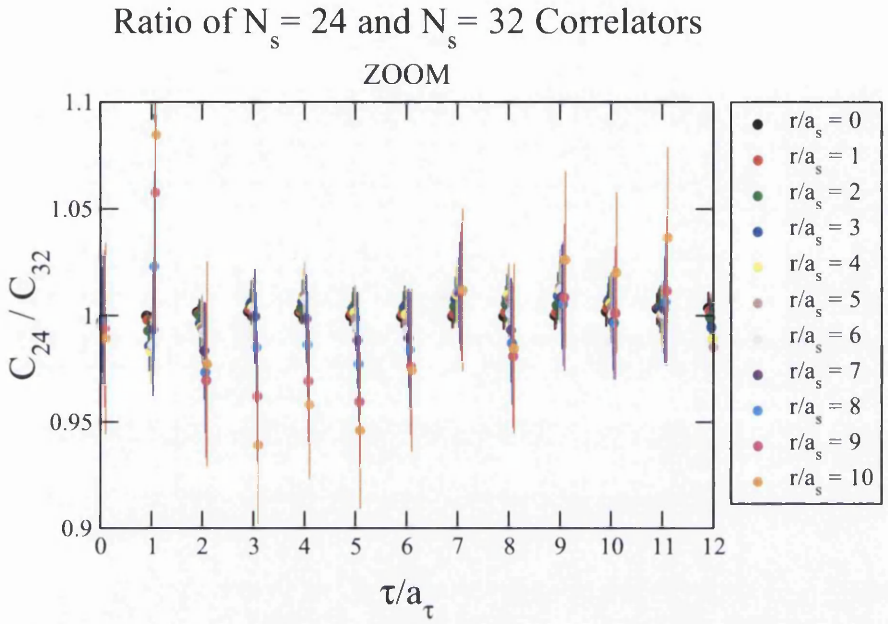

Figure 5.22: The same data as in Figure 5.21 but showing only $0 \le r/a_s \le 10$. Also the data points have been slightly horizontally shifted to make the error bars visible.

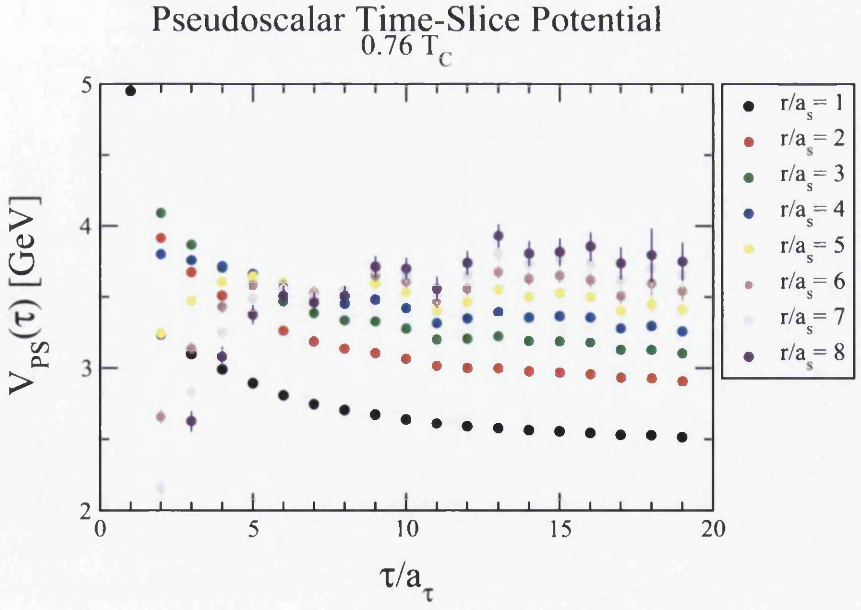

Figure 5.23: The $0.76T_C$ pseudoscalar time-slice potential plotted as a function of τ for each quark separation r, using (5.17).

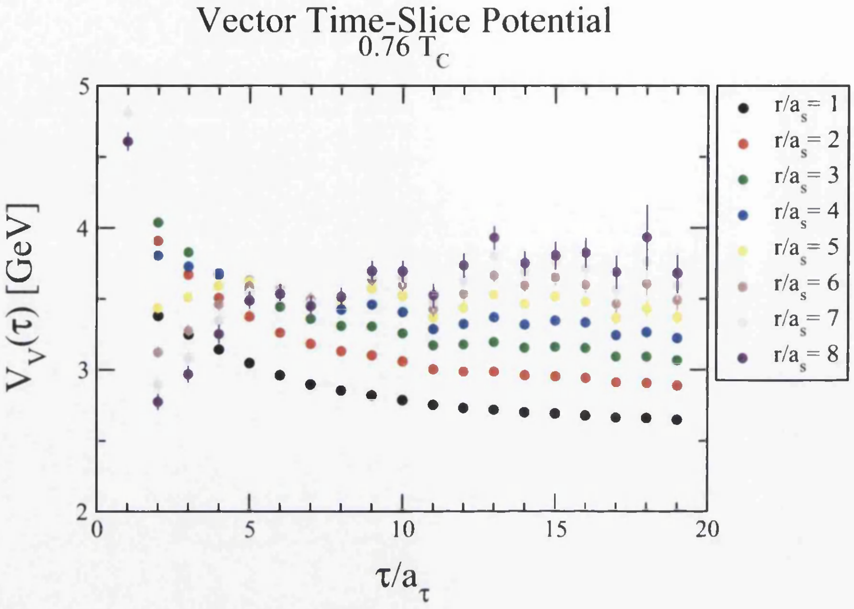

Figure 5.24: The $0.76T_C$ vector time-slice potential plotted as a function of τ for each quark separation r, using (5.17).

N_τ	T [T_C]	Central (Upper) Range	Lower Range
128	'Zero'	30 – 63	15 – 19
40	0.76	15 – 19	12 – 17
36	0.84	12 – 17	11 – 15
32	0.95	11 – 15	11 – 13
28	1.09	11 – 13	N/A

Table 5.3: $N_f = 2 + 1$ fitting ranges.

these time-slice potentials according to (4.12), the spin-independent time-slice potential shown in Figure 5.25 was obtained. The spin-independent time-slice potentials from all ensembles are shown in Appendix B. Out of these the $1.27T_C$, $1.52T_C$ and $1.90T_C$ spin-independent potentials are not considered any further due to them having no τ range in which the potential is stable. The other time-slice spin-independent potentials were fitted for the τ ranges shown in Table 5.3. In these τ ranges a time-wise correlated fit to a constant was performed on the time-slice potentials for each separation. This generated a single value for the potential at each separation r. The end result of the analysis for the spin-independent potential is shown in Figure 5.26. The potentials appear at very similar energies, much more so than in the $N_f = 2$

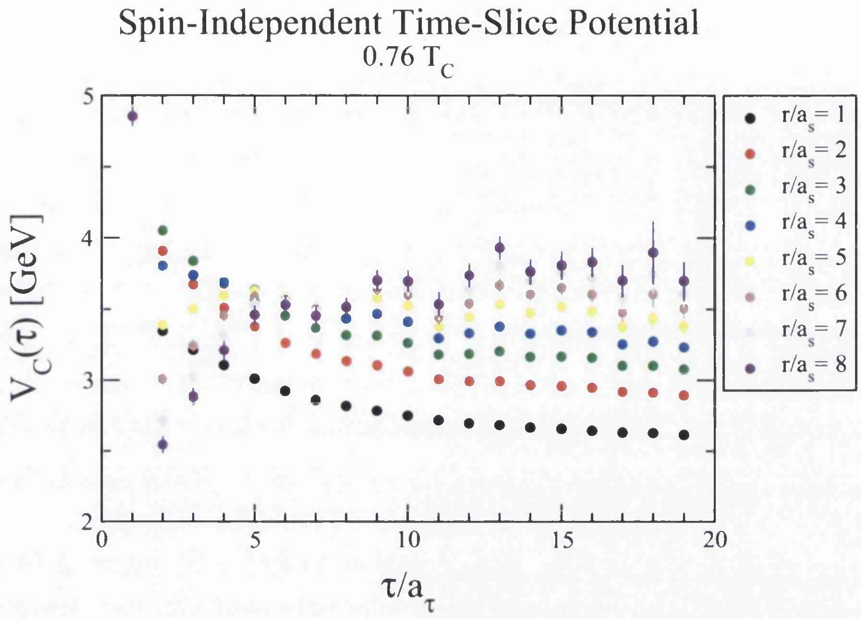

Figure 5.25: The $0.76T_C$ spin-independent time-slice potential plotted as a function of τ for each quark separation r.

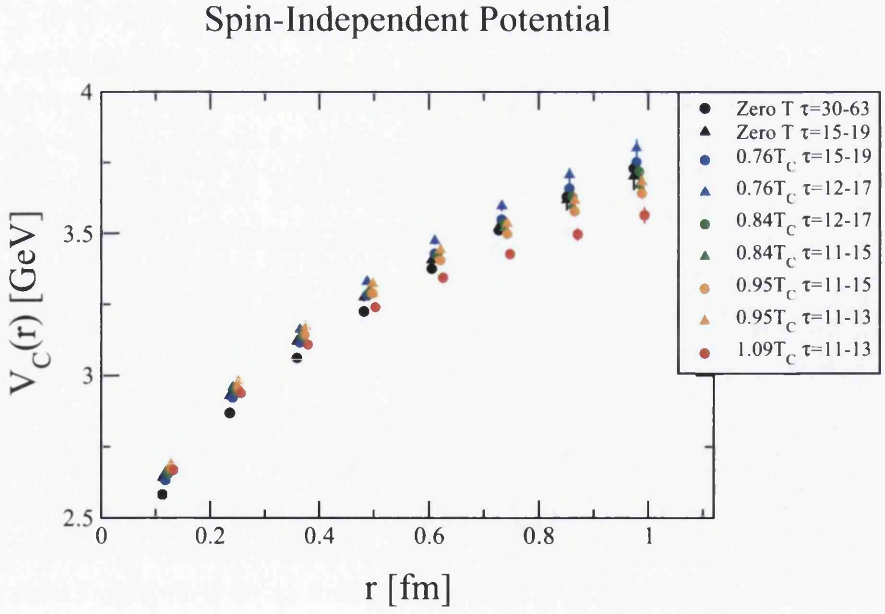

Figure 5.26: The spin-independent potential plotted for all τ ranges and temperatures.

case, see Figure 5.8. This is encouraging because it suggests the chosen τ ranges all overlap well with the stable plateau region.

Nevertheless to compare the form of the curves, the potentials are shifted in Figure 5.27 such that the $r/a_s = 1$ data points coincide with that of the 'zero' temperature potential. The Cornell potential is also included again; the potentials take a form that could clearly be built from a Coulomb and linear term. In this case it is particularly important that the potentials are observed to have a Coulomb-like form at small r because the configurations were stout-link smeared. If there was a complete lack of a Coulomb-like behaviour at small r, then it would be reason to believe the stout-link smearing procedure had corrupted the short-range information of the configurations. The divergence of potentials from the Cornell potential at small r could simply be a reflection of the true charmonium potential, or an artifact of the finite lattice spacing.

In Figure 5.28 the triangular data points in Figure 5.27 are used to form a systematic error bar on the corresponding circular data points for each temperature, as was done in the $N_f = 2$ case. According to the τ ranges in Table 5.3, potentials can only be compared with the potential corresponding to the next highest temperature. Comparing the potentials in a manner adhering to this criterion we do not see a significant temperature effect between zero temperature and $0.76T_C$ at large r. Between $0.76T_C$ and $0.84T_C$, and $0.95T_C$ and $1.09T_C$ the spin-independent potential flattens by an amount more significant than the systematic error. Between $0.84T_C$ and $0.95T_C$ the potential flattens by an amount that is on the limit of the systematic error.

At small r the zero temperature potential is lower than the $0.76T_C$ potential, contrary to what we expect due to colour-Debye screening. This is initially disappointing because the zero temperature result is the most reliable. However as so many more data points were available for the zero temperature case, it is not surprising that it takes a different form to the high temperature potentials. From Figure B.1 we see the data points continue to decrease significantly with time until roughly $\tau = 30$. As it is only for the zero temperature ensemble that we can fit the time-slice potentials above this τ value, the zero temperature spin-independent potential is the only one for which we obtain a result solely from a true plateau. For the higher temperatures the time-slice potentials are still 'settling', even for the largest available τ.

In parallel, the fact that the zero temperature potential does not lie above the $0.76T_C$ potential can be seen as a reasonable outcome based on colour-Debye screen-

T[T_C]	(σ [GeV])^2	a [GeV^{-1}]
'Zero'	0.4352	2.2978
'Zero'*	0.3975	2.5156
0.76	0.4167	2.4001
0.76*	0.4187	2.3886
0.84	0.3977	2.5146
0.84*	0.3643	2.7453
0.95	0.3561	2.8080
0.95*	0.3583	2.7908
1.09	0.3424	2.9206

Table 5.4: The results of performing a linear fit on the large r data of the spin-independent potentials shown in Figure 5.28. The string tension σ is equivalent to a^{-2}, displayed in alternative units. The values obtained for the string tension, with an asterisk on the associated temperature, can be compared to that of the next highest temperature in a fair manner, since they were extracted from spin-independent potentials obtained from the same τ range.

ing. As the temperature increases more and more colour-charges are produced from the vacuum, but the interquark potential is not modified significantly until the density of colour-charges is comparable to the interquark separation. From the results for $0.76T_C$ we could conclude that the density of colour-charges is such that the charmonium potential is unmodified up to this temperature.

To shed more light on the temperature dependence of the spin-independent potentials their associated string tensions were calculated by performing a linear fit on the $V_C(r/a_s = 5-8)$ data (see Table C.1) of Figure 5.28. The results of these fits are shown in Table 5.4. In general the string tension decreases as the temperature increases. It is only between zero temperature and $0.76T_C$ that the string tension increases against this trend significantly. The likely reasons for this are the same as those discussed above for the form of the potential. Interestingly, the value of the string tension extracted from the zero temperature ensemble, $(0.4352\text{MeV})^2$, is very close to the ubiquitous literature value of $(0.44\text{MeV})^2$, this is further evidence that the method is extracting the correct physics.

On the whole we conclude that the spin-independent potential flattens as the temperature increases, which is in line with our expectation that the interquark potential becomes colour-Debye screened at high temperature.

We also obtained the spin-dependent time-slice potentials for the different temperatures by combining the pseudoscalar and vector time-slice potentials from each

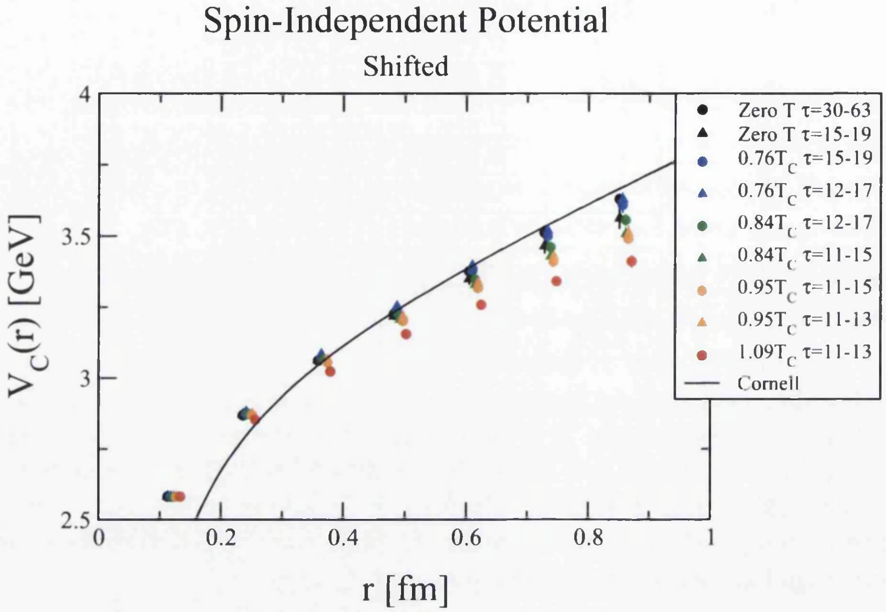

Figure 5.27: The spin-independent potential plotted for all τ ranges and temperatures. The potentials have been shifted. The Cornell potential is plotted using (2.17) with $\kappa = 0.52$ and $a = 2.34\text{GeV}^{-1}$.

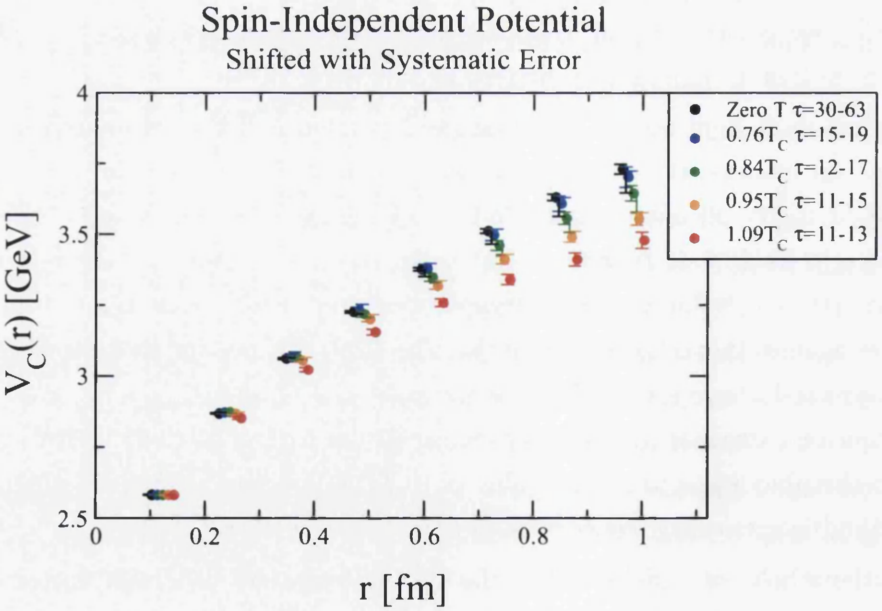

Figure 5.28: The spin-independent potential with systematic error plotted for all temperatures. Statistical error bars appear to the left and systematic ones to the right of data points.

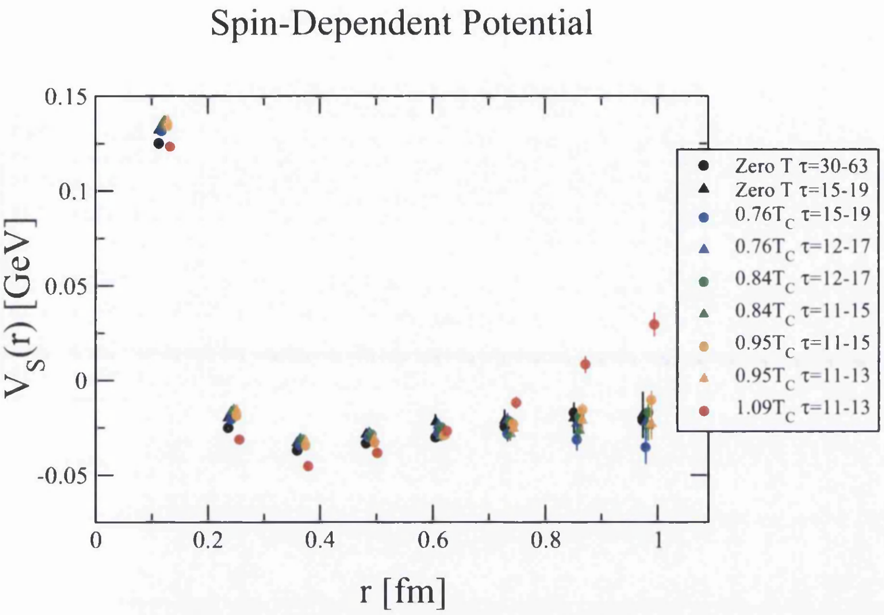

Figure 5.29: The spin-dependent potential plotted for all τ ranges and temperatures.

ensemble according to (4.13). These were analysed in the same way as the time-slice spin-independent plots to obtain Figure 5.29, Figure 5.30 and Figure 5.31. As for the $N_f = 2$ simulation the spin-dependent potential appears to have a repulsive core at small r but taking into account the uncertainty is quite constant for large r. A similar form for the spin-dependent potential has been found in another lattice study [23]. A temperature dependence is less apparent in the spin-dependent potential than in the spin-independent potential. The systematic error is typically larger than any change in the potential due to the temperature changing. One factor is simply that the spin-dependent potentials are a difference rather than sum of the pseudoscalar and vector potentials, meaning uncertainties are relatively larger.

In Figure 5.32 the spin-independent potentials obtained from the $N_f = 2$ and $N_f = 2 + 1$ simulations using the time-dependent method are compared. It is important to note that neither set of results has been shifted vertically from their positions in Figure 5.9 and Figure 5.27. It is encouraging that the potential data points interpolate each other at small r, especially given that the lattice parameters used in each simulation are quite different. For a given temperature the $N_f = 2 + 1$ spin-independent potentials are flatter at large r than those from the $N_f = 2$ simulation. This could be due to the inclusion of an extra sea quark that has the ability to screen the strong force between quarks, but it could also be an effect analogous

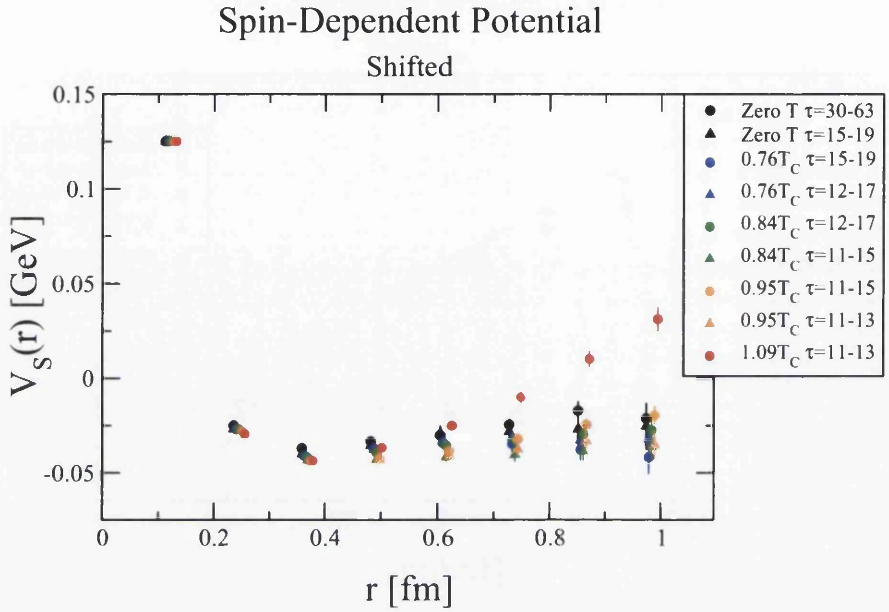

Figure 5.30: The spin-dependent potential plotted for all τ ranges and temperatures, but shifted vertically.

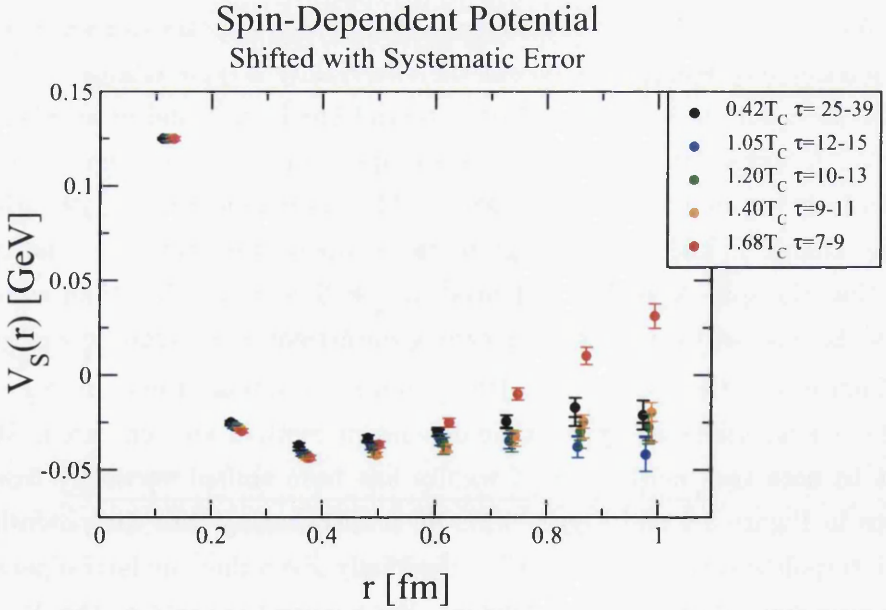

Figure 5.31: The spin-dependent potential plotted for all temperatures. Statistical error bars appear to the left and systematic ones to the right of data points.

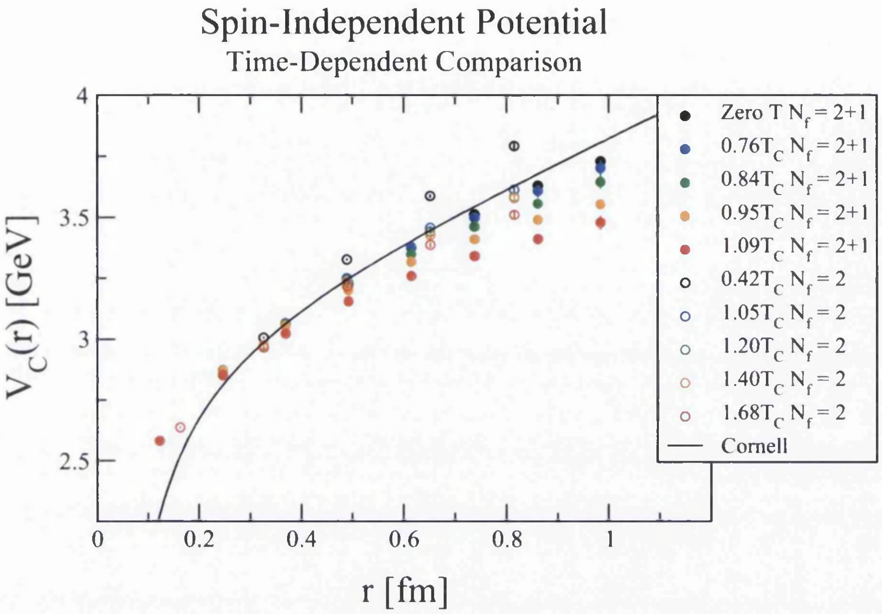

Figure 5.32: A comparison of the spin-independent potentials obtained from the $N_f = 2$ (Figure 5.9) and $N_f = 2 + 1$ (Figure 5.27) simulations using the time-dependent method.

to that seen in Figure 5.18. There we saw a divergence of the potential depending on the type of separation, but we can equivalently view this as a dependence of the potential on the spatial lattice spacing. In Figure 5.18 the relevant spatial lattice spacings are a_s, $a_s\sqrt{2}$ and $a_s\sqrt{3}$ for the on-axis, face-diagonal and body-diagonal type separations, where $a_s = 0.162$fm. There the potential appears to flatten at larger r as the spatial separation of neighbouring points decreases. In Figure 5.32 we see the same behaviour between the potentials obtained from the lattice with larger a_s, namely the $N_f = 2$ results, and the lattice with smaller a_s, namely the $N_f = 2 + 1$ results, where $a_s = 0.123$fm. Here the potentials also appear to flatten more for the smaller spatial lattice spacing.

In Figure 5.33 we compare the spin-independent potentials with the heavy quark free energies obtained in [115] — in this work the heavy quark free energy of a static quark-anti-quark pair in a colour singlet state separated by a distance r is defined by,

$$\frac{F_1(r,T)}{T} = -\log\left[\mathrm{Tr}\left(L_{\mathrm{ren}}(0)L_{\mathrm{ren}}(r)\right)\right], \tag{5.36}$$

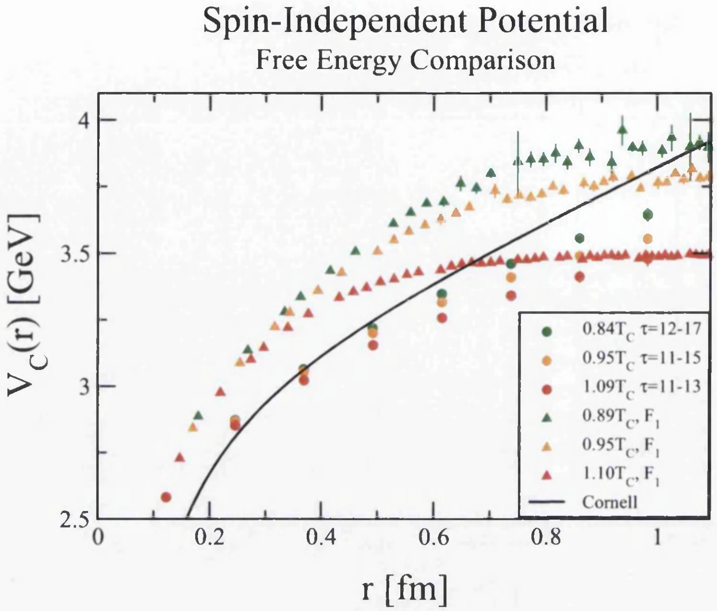

Figure 5.33: The spin-independent potential plotted against heavy quark free energies for comparable temperatures. The free energy data has been vertically shifted for the sake of comparison.

where L_{ren} is the renormalized Polyakov loop. The free energy curves in Figure 5.33 have been shifted vertically in energy from their position in [115] so that their form can be compared to the $N_f = 2 + 1$ spin-independent potentials. A more significant temperature effect is seen in the free energies than in the $N_f = 2 + 1$ potentials. However a direct comparison with the $N_f = 2 + 1$ potentials would not be reasonable because they have been calculated using a finite charm mass whereas the free energies were calculated for infinitely heavy charm quarks.

5.7 Conclusions

For both $N_f = 2$ and $N_f = 2 + 1$, the time-dependent method yields spin-independent potentials with the expected Coulomb-plus-linear form. This in itself is good evidence that the method is successfully extracting correct physics from the simulations. Furthermore in the $N_f = 2 + 1$ case this confirms that the stout-link smearing of the configurations is not interfering with the short-range physics.

The $N_f = 2$ spin-independent potentials do not exhibit a conclusive temperature dependence in agreement with colour-Debye screening, though one is seen between the $0.42T_C$ and $1.05T_C$ potentials. Observing a temperature dependence between higher temperatures was hindered by the correspondingly short temporal extents.

Overall the $N_f = 2+1$ spin-independent potentials do exhibit a conclusive temperature dependence, in agreement with colour-Debye screening. Taking into account the $N_f = 2$ and $N_f = 2+1$ results together we conclude that the time-dependent method is only applicable up to some limiting temperature, above which the effect of higher excited states and lattice artifacts prevents the method from being sensibly applied. For the lattice parameters used in this study, the maximum temperature at which the method has been sensibly applied is $1.09T_C$. Since the $N_f = 2+1$ lattice parameters were not chosen specifically for the time-dependent method it is safe to assume a more tailored choice of lattice parameters would allow the potential to be extracted for $T > 1.09T_\mathrm{C}$.

From Figure 5.18 and Figure 5.32 we note that the use of a coarser spatial lattice spacing may spuriously increase the gradient of the spin-independent potential at large r. Alternatively, the divergence of the on-axis, face-diagonal and body-diagonal potentials in Figure 5.18 may be reduced by using Cartesian rather spherical coordinates in the future. In any case, we assume that the finer lattice spacing provides the more correct result, as such the disagreement seen between the $N_f = 2$ and $N_f = 2+1$ results in Figure 5.32 brings into doubt the validity of the $N_f = 2$ results. Another issue with the $N_f = 2$ results is that the dimensionful spatial extent of the configurations is less than that of the $N_f = 2+1$ configurations. Consequently the volume dependence study done for the $N_f = 2+1$ configurations brings into question the validity of at least the $r/a_s = 5, 6$ data points. The unknown extent of boundary effects and the short temporal extents of the $N_f = 2$ results means the $N_f = 2+1$ results are favoured for their reliability.

Chapter 6

Conclusion

In this thesis charmonium potentials have been calculated using two different methods to analyse correlators obtained from dynamical simulations of QCD.

Conventional fitting techniques were applied to correlators obtained from a $N_f = 2$ simulation. Potentials could not be extracted from local-extended correlators because in this case some higher excited states contribute to the correlator with a negative sign. As a result the correlators do not have a functional form that is always decaying exponentially, which means fitting functions with a single exponential term for each correlator fail. We conclude that conventional fitting techniques should not be applied to local-extended correlators, or at least not on lattices with short temporal extents. In the extended-extended case fitting was more successful, higher excited states always contribute to the correlator with a positive sign, which is guaranteed by the symmetric source and sink operators. However the reliability of the potentials from this analysis is brought into question for the following reasons: i) higher excited states pollute the results for the ground state wave functions even at the largest available τ; ii) the mass values obtained from fitting increase very significantly with temperature; and iii) the spin-independent potentials do not have a Coulomb-plus-linear form. Consequently even though the analysis of extended-extended correlators using conventional fitting techniques yields a temperature dependent spin-independent potential, which flattens in agreement with the concept of colour-Debye screening, the result is deemed unreliable. The spin-dependent potential from conventional fitting was found to be repulsive at small quark separation and attractive at larger quark separation, but this result is as unreliable as the the spin-independent one.

The HAL QCD time-dependent method was applied to correlators obtained from

$N_f = 2$ and $N_f = 2+1$ simulations. In both cases the spin-independent potentials have a clear Coulomb-plus-linear form, which alone is good evidence that the method is extracting the correct physics from the simulations. In the $N_f = 2+1$ case this confirms that the short-range information of the configurations was not affected by stout-link smearing. From the $N_f = 2$ simulation a temperature dependence in the spin-independent potential cannot be concluded because the dependence on the τ range used to fit time-slice potentials is significant. This is more than likely a simple function of the relatively short temporal extent of the corresponding configurations. The $N_f = 2$ ensembles have a smaller temporal lattice spacing and in general have fewer temporal data points than the $N_f = 2+1$ ensembles. Due to the short temporal extent, the analysis is always being performed at a time that is too early for lattice artifacts and higher excited state effects to have abated, and these effects mask any underlying temperature dependence. However in the $N_f = 2+1$ case the temperature dependence is more significant than the effect of changing the τ range. Between $0.76\mathrm{T_C}$ and $1.09\mathrm{T_C}$, the spin-independent potential flattens at large r with increasing temperature, which is consistent with the expectation that the interquark potential becomes deconfining at high temperature due to colour-Debye screening. The change in the potential with temperature is quite gradual, in general and when compared to heavy quark free energies, but since the phase transition from hadronic matter to QGP is a cross-over, a rapidly changing potential is not expected. Spin-dependent potentials were also calculated. Like the $N_f = 2$ result, the $N_f = 2+1$ spin-dependent potentials were found to have little dependence on temperature and to be strongly repulsive at small quark separation, but at larger quark separation, with the exception of the $1.09T_C$ result, the potential is constant. The $N_f = 2+1$ time-dependent results are the most reliable in this thesis, therefore it is encouraging that out of the three results for the spin-dependent potential, the form of the $N_f = 2+1$ result agrees best with the existing literature.

An efficient method for calculating charmonium correlators from momentum space quark propagators was implemented as part of this work. This decreased the time taken to calculate correlators and allowed correlators corresponding to any quark separation, not just on-axis quark separations, to be computed. It was hoped that correlators corresponding to quark separations along face- and body-diagonals could be analysed to obtain potentials at an increased number of quark separations. However it was discovered that the spin-independent potential has a dependence on the spatial lattice spacing — the smaller the spacing, the more the potential flattens. This effect should be investigated further. If this effect is related to the resolution with which the correlator's dependence on the quark separation is known, then one would expect that below a certain value, all values of the spatial lattice spacing should give the same result.

The time-dependent method is limited by the lattice size and spacings of the ensemble to which it is being applied. A lattice with many points in the temporal extent with a fine temporal lattice spacing is required to accurately apply this method to higher temperatures. Furthermore a large spatial volume and a fine spatial lattice spacing is required to reduce boundary effects and help allow off-axis separations to be used. Configurations with many more lattice sites than the ones used in this work are now routinely generated, and with supercomputers improving every year these requirements can be realistically met, meaning the time-dependent method could definitely be used to calculate potentials accurately at temperatures below, around and significantly above T_{C} in the future. One may think anisotropic lattices are unnecessary, since both fine temporal and spatial lattice spacings are being called for, however anisotropic lattices are important for high temperature studies because they allow the spatial volume to be kept constant while varying the temperature, thus avoiding any dependence of the results on spatial volume. Ideally the number of temporal lattice points would be kept constant and large while the temporal lattice spacing was used to vary the temperature. At present this is not an option because every temperature would then correspond to a different anisotropy and tuning the bare input parameters of the action for just a single anisotropy value takes many personnel-hours. An automatic way to do this would be extremely valuable.

In this thesis the approximate rotational symmetry of the lattice was relied upon to evaluate the second derivative of wave functions or correlators in spherical coordinates. The advantage of using spherical coordinates was that only correlators corresponding to quark separations along the radial direction were required. However, due to the geometry of the lattice Cartesian coordinates are the most appropriate choice. Therefore the implementation of Cartesian coordinates is an obvious improvement that can be made in the future. For example in the context of the time-dependent method, the local-extended correlators corresponding to all possible quark separations could be obtained, then the second derivative in (5.17) could be evaluated using the Cartesian finite difference operator,

$$\frac{\delta_{x',x+a} - 2\delta_{x',x} + \delta_{x',x-a}}{a^2} + \frac{\delta_{y',y+a} - 2\delta_{y',y} + \delta_{x',y-a}}{a^2} + \frac{\delta_{z',z+a} - 2\delta_{z',z} + \delta_{z',z-a}}{a^2}, \qquad (6.1)$$

instead of (4.9) to obtain the potential at all lattice sites, assuming periodic boundary conditions are used. It would be interesting to see how using Cartesian coordinates affects the Coulomb section of the spin-independent potential and the divergence of the on-axis, face-diagonal and body-diagonal potentials in Figure 5.18.

The most obvious future application of the time-dependent method is to lattice QCD configurations that have been generated with the method in mind, but the method could also be applied to other systems where non-perturbative effects are of interest. For example the method could be used to calculate the electron-hole potential in graphene using a lattice model. Another effect that could be given attention is string breaking. In dynamical simulations the potential should become horizontal at roughly twice the mass of the quark in the bound state. If a larger spatial extent is used or the disparity between on-axis, face-diagonal and body-diagonal potentials is solved, then string breaking should be observable.

Appendix A

$N_f = 2$ Spin-Independent Time-Slice Potentials

In this appendix the spin-independent time-slice potentials calculated by applying (5.17) to the local-extended correlators obtained from the $\mathrm{N_f} = 2$ simulation (Section 4.4) are shown. The $1.05T_{\mathrm{C}}$ plot is shown again for convenience.

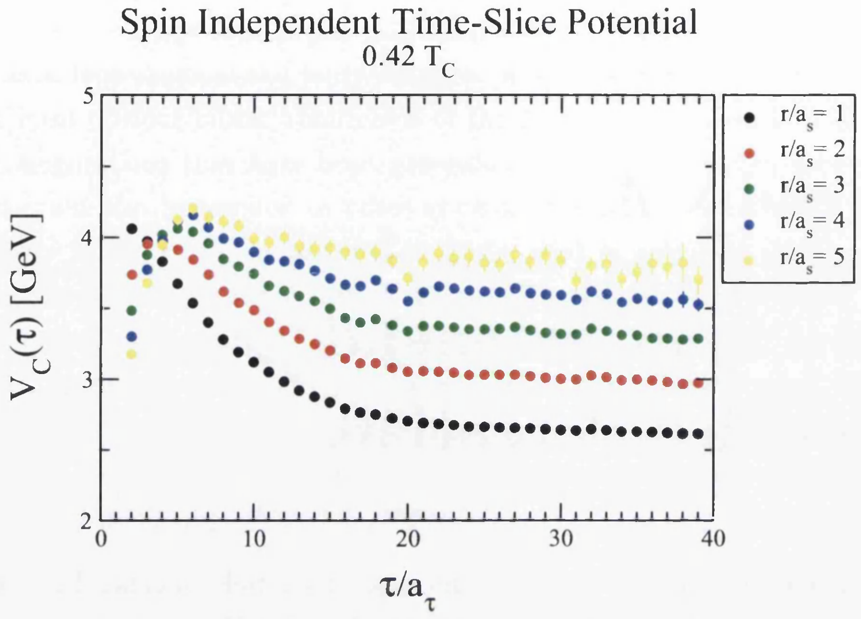

Figure A.1: $0.42T_C$ spin-independent potential plotted as a function of τ for each quark separation r.

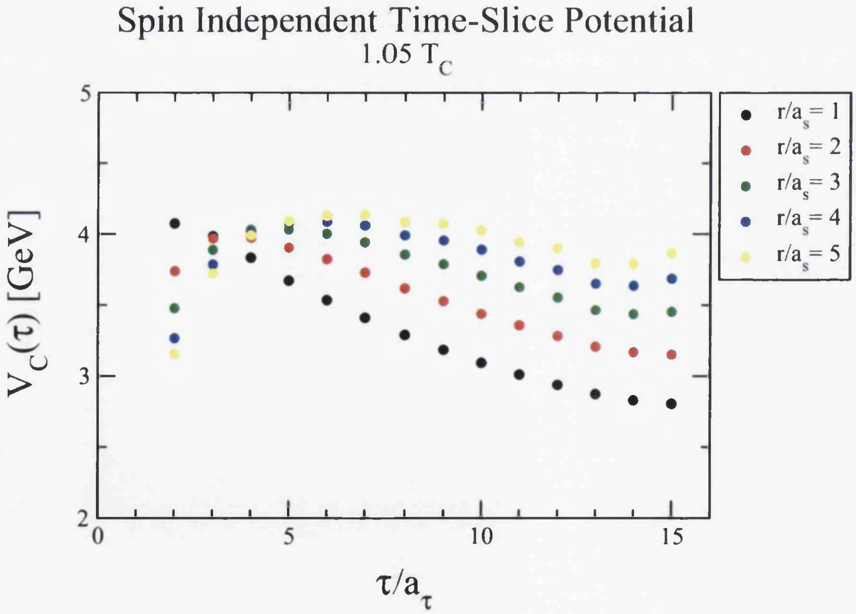

Figure A.2: $1.05T_C$ spin-independent potential plotted as a function of τ for each quark separation r.

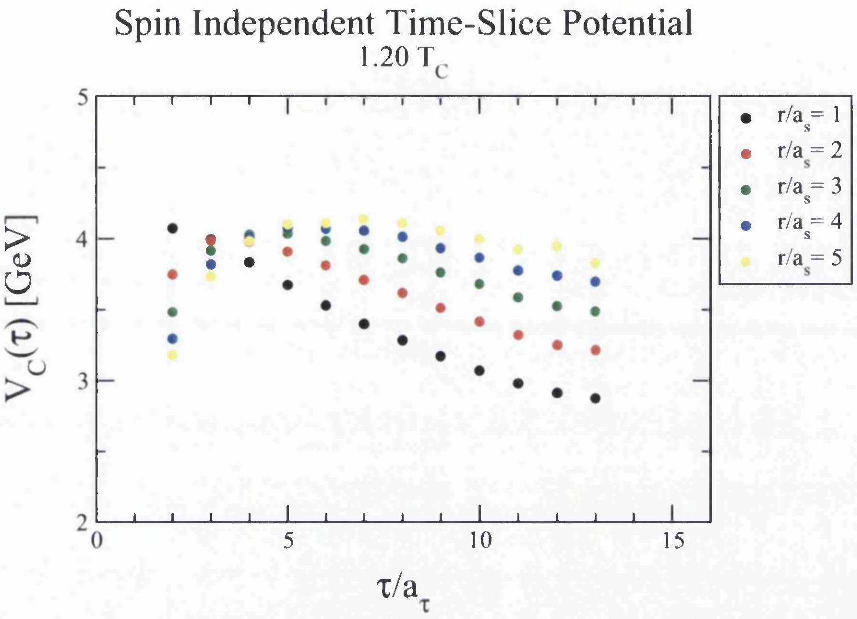

Figure A.3: $1.20T_C$ spin-independent potential plotted as a function of τ for each quark separation r.

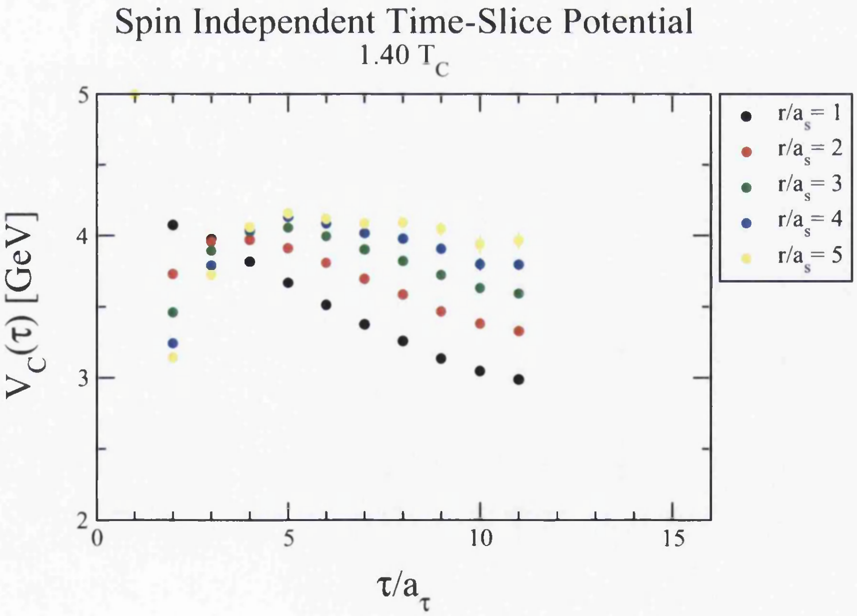

Figure A.4: $1.40T_C$ spin-independent potential plotted as a function of τ for each quark separation r.

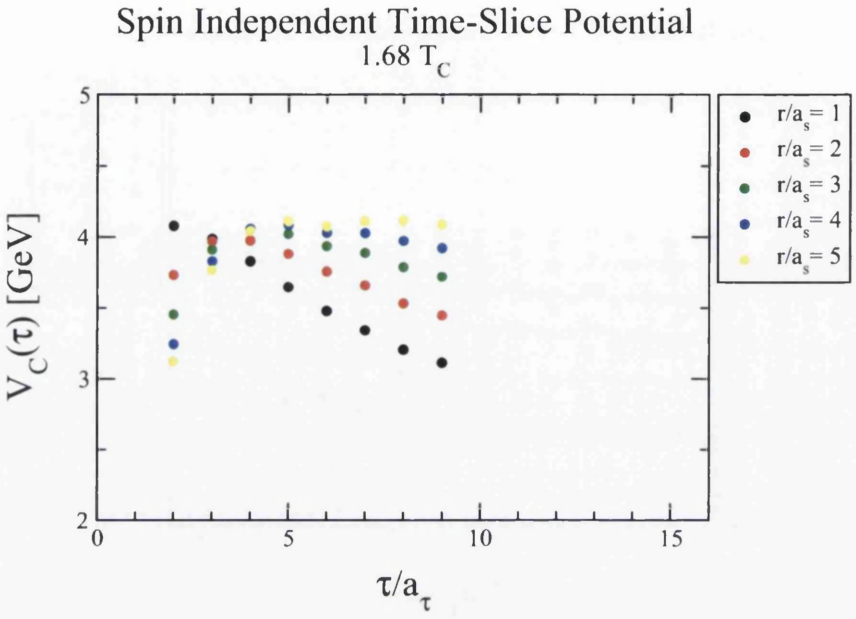

Figure A.5: $1.68T_C$ spin-independent potential plotted as a function of τ for each quark separation r.

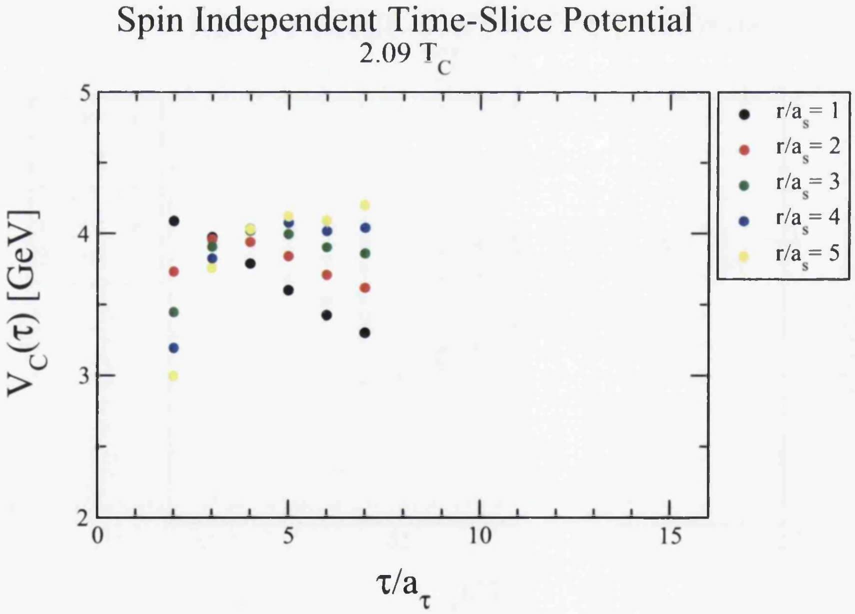

Figure A.6: $2.09T_C$ spin-independent potential plotted as a function of τ for each quark separation r.

Appendix B

$N_f = 2 + 1$ Spin-Independent Time-Slice Potentials

In this appendix the spin-independent time-slice potentials calculated by applying (5.17) to the $N_s = 24$ local-extended correlators obtained from the $\mathrm{N_f} = 2 + 1$ simulation (Section 5.5) are shown. The $0.76T_\mathrm{C}$ plot is shown again for convenience.

SWANSEA UNIVERSITY LIBRARY

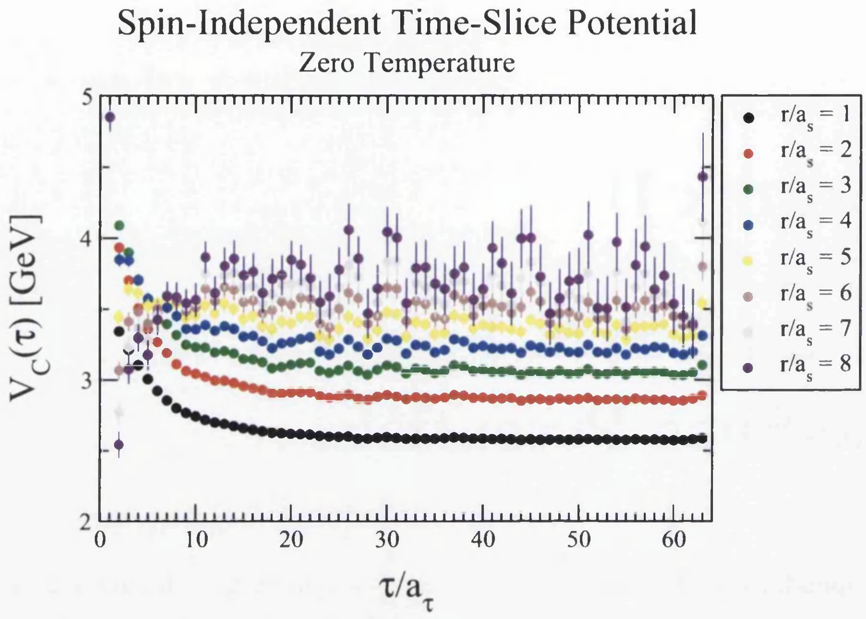

Figure B.1: Zero temperature spin-independent potential plotted as a function of τ for each quark separation r.

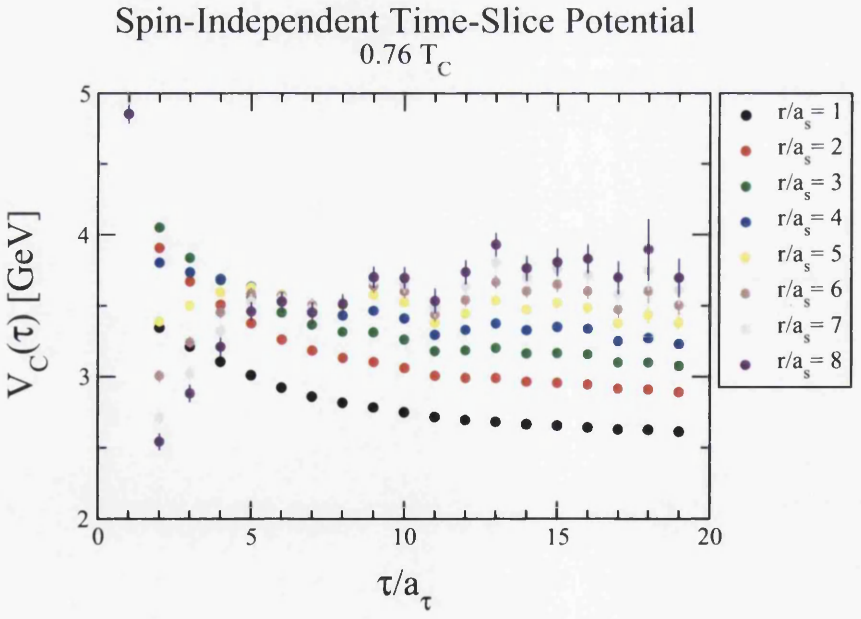

Figure B.2: $0.76T_C$ spin-independent potential plotted as a function of τ for each quark separation r.

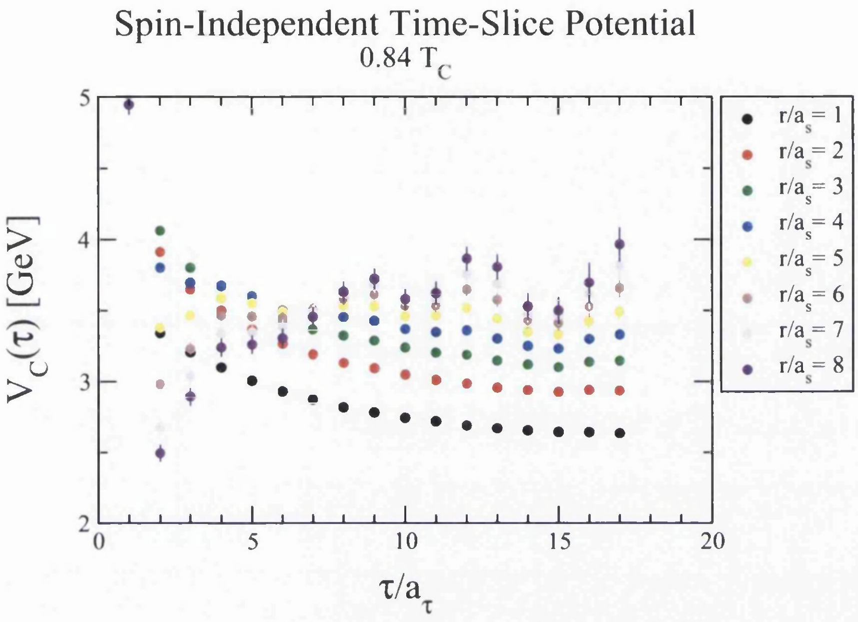

Figure B.3: $0.84T_C$ spin-independent potential plotted as a function of τ for each quark separation r.

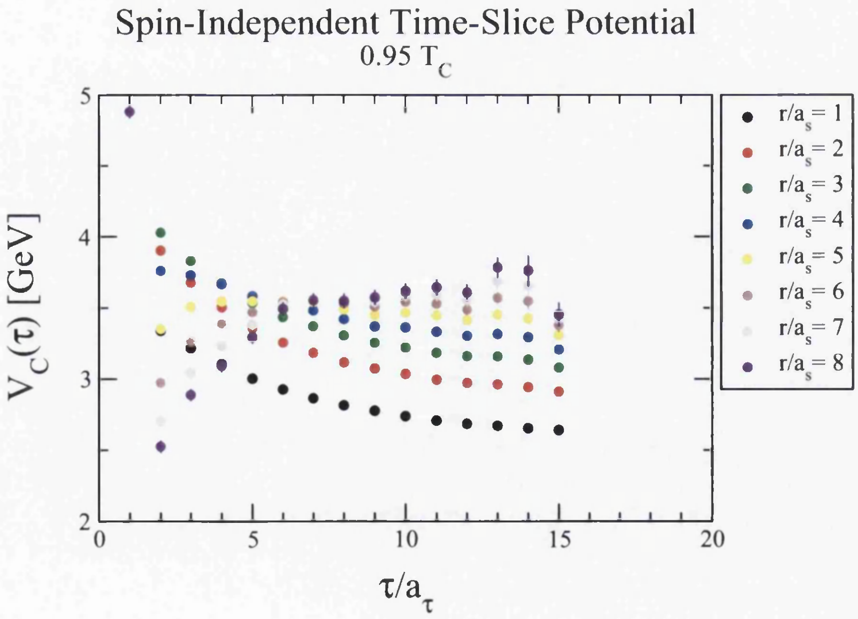

Figure B.4: $0.95T_C$ spin-independent potential plotted as a function of τ for each quark separation r.

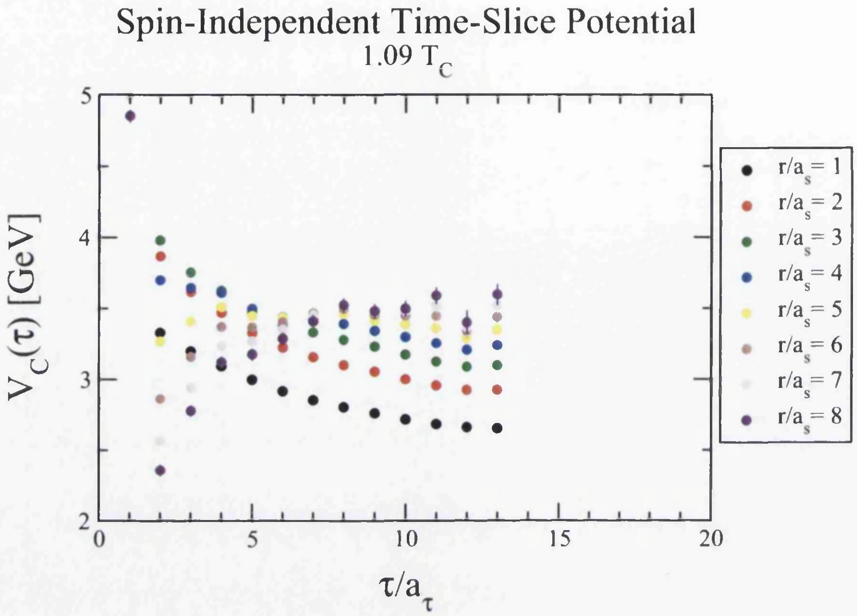

Figure B.5: $1.09T_C$ spin-independent potential plotted as a function of τ for each quark separation r.

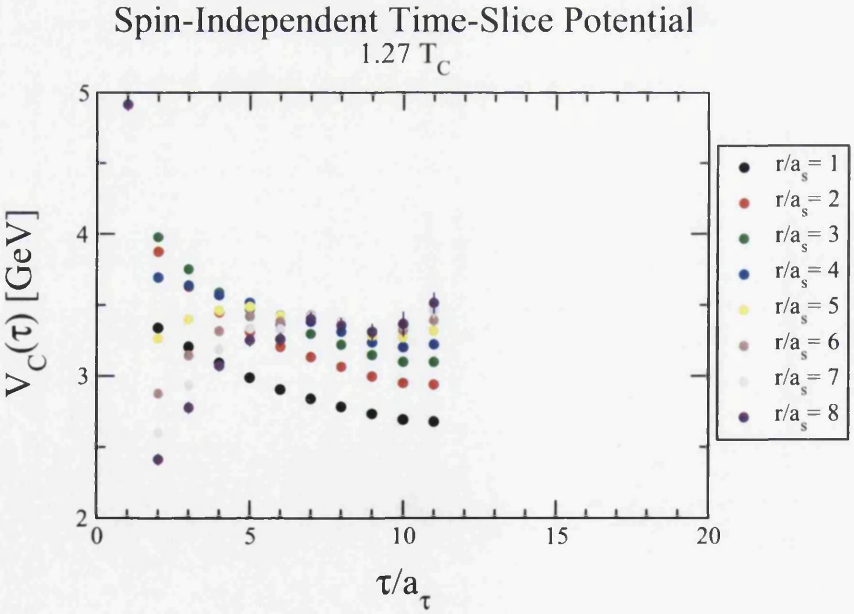

Figure B.6: $1.27T_C$ spin-independent potential plotted as a function of τ for each quark separation r.

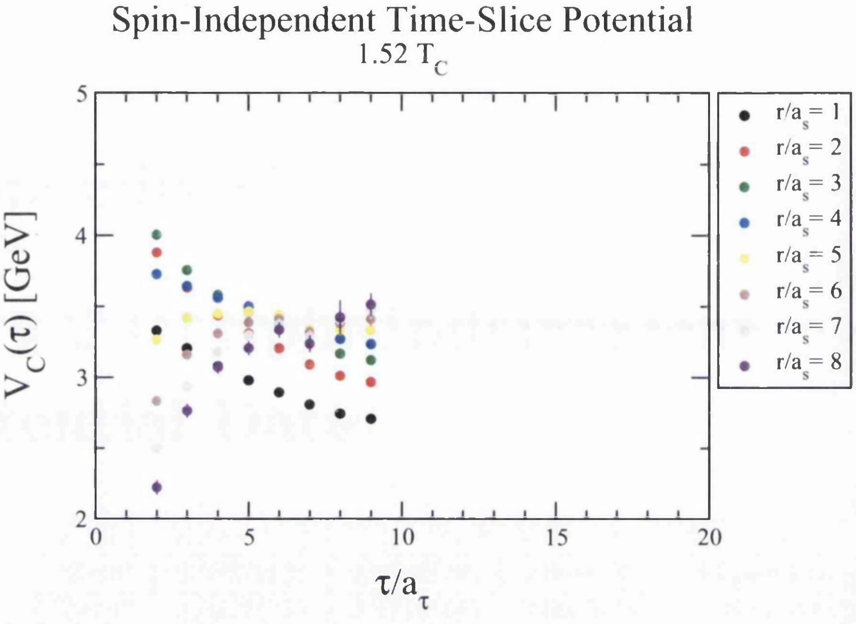

Figure B.7: $1.52T_C$ spin-independent potential plotted as a function of τ for each quark separation r.

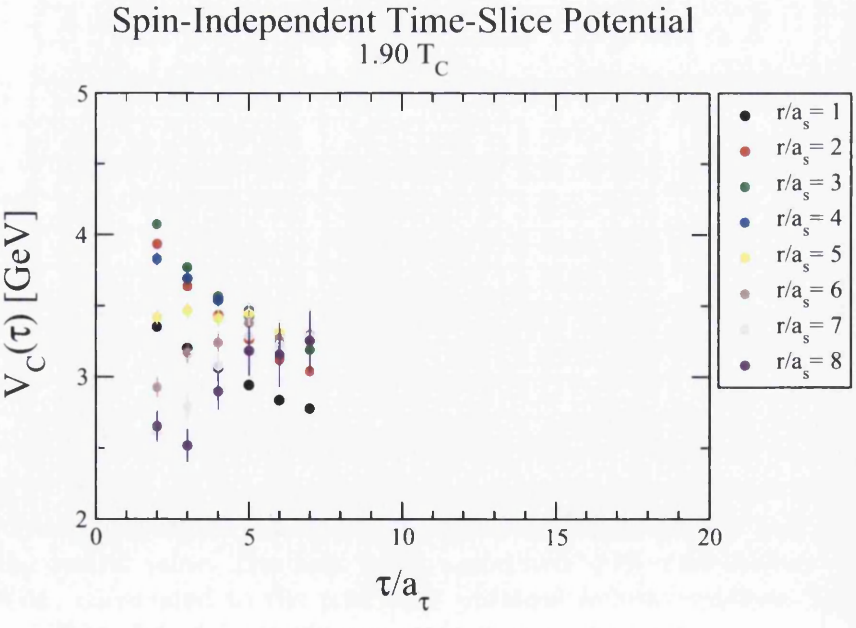

Figure B.8: $1.90T_C$ spin-independent potential plotted as a function of τ for each quark separation r.

Appendix C

$N_f = 2 + 1$ Spin-Independent Potential Data

T [T_C]	$V_C(r=1a_s)$	$V_C(r=2a_s)$	$V_C(r=3a_s)$	$V_C(r=4a_s)$	$V_C(r=5a_s)$	$V_C(r=6a_s)$	$V_C(r=7a_s)$	$V_C(r=8a_s)$
‘Zero’	2.5822(12)	2.8687(20)	3.0618(30)	3.2258(42)	3.3760(59)	3.5111(80)	3.6302(114)	3.7298(169)
‘Zero’*	2.5822(35)	2.8716(64)	3.0635(99)	3.2185(143)	3.3498(201)	3.4647(275)	3.5625(375)	3.6455(500)
0.76	2.5822(26)	2.8725(46)	3.0669(73)	3.2318(109)	3.3783(153)	3.4988(207)	3.6090(270)	3.7023(357)
0.76*	2.5822(26)	2.8821(46)	3.0854(70)	3.2527(102)	3.3970(141)	3.5192(190)	3.6304(249)	3.7241(321)
0.84	2.5822(25)	2.8736(46)	3.0655(73)	3.2192(103)	3.3482(135)	3.4611(170)	3.5567(214)	3.6450(270)
0.84*	2.5822(28)	2.8714(50)	3.0600(80)	3.2068(114)	3.3297(151)	3.4285(193)	3.5074(242)	3.5791(305)
0.95	2.5822(200)	2.8691(36)	3.0556(56)	3.2008(79)	3.317(105)	3.4097(134)	3.4899(168)	3.5539(211)
0.95*	2.5822(24)	2.8740(47)	3.0664(77)	3.2172(114)	3.3368(158)	3.4296(210)	3.5112(276)	3.5763(361)
1.09	2.5822(24)	2.8528(44)	3.0233(71)	3.1552(103)	3.2588(138)	3.3414(179)	3.4116(228)	3.4790(288)

Table C.1: The $N_f = 2 + 1$ spin-independent potential data of Figure 5.27. The statistical uncertainty in the data is located inside round parentheses and is symmetric about the central value. The data values associated to the temperature values with an asterisk, correspond to the potentials obtained for the τ ranges in the fourth column of Table 5.3. A linear fit was performed on the $V(r = 5 - 8a_s)$ data shown in the second tier of the table, to obtain the string tension for each temperature.

Bibliography

[1] T. Matsui and H. Satz, "J/ψ Suppression by Quark-Gluon Plasma Formation," *Phys. Lett.* **B178** (1986) 416.

[2] P. Braun-Munzinger and J. Stachel, "(Non)thermal aspects of charmonium production and a new look at J/ψ suppression," *Phys.Lett.* **B490** (2000) 196–202, `arXiv:nucl-th/0007059 [nucl-th]`.

[3] P. Braun-Munzinger and J. Stachel, "On charm production near the phase boundary," *Nucl.Phys.* **A690** (2001) 119–126, `arXiv:nucl-th/0012064 [nucl-th]`.

[4] Y.-p. Liu, Z. Qu, N. Xu, and P.-f. Zhuang, "J/ψ Transverse Momentum Distribution in High Energy Nuclear Collisions at RHIC," *Phys.Lett.* **B678** (2009) 72–76, `arXiv:0901.2757 [nucl-th]`.

[5] X. Zhao and R. Rapp, "Medium Modifications and Production of Charmonia at LHC," *Nucl.Phys.* **A859** (2011) 114–125, `arXiv:1102.2194 [hep-ph]`.

[6] M. Laine, O. Philipsen, P. Romatschke, and M. Tassler, "Real-time static potential in hot QCD," *JHEP* **0703** (2007) 054, `arXiv:hep-ph/0611300 [hep-ph]`.

[7] F. Karsch, M. Mehr, and H. Satz, "Color Screening and Deconfinement for Bound States of Heavy Quarks," *Z.Phys.* **C37** (1988) 617.

[8] Y. Burnier, M. Laine, and M. Vepsalainen, "Heavy quarkonium in any channel in resummed hot QCD," *JHEP* **0801** (2008) 043, `arXiv:0711.1743 [hep-ph]`.

[9] N. Brambilla, J. Ghiglieri, A. Vairo, and P. Petreczky, "Static quark-antiquark pairs at finite temperature," *Phys.Rev.* **D78** (2008) 014017, `arXiv:0804.0993 [hep-ph]`.

[10] A. Dumitru, Y. Guo, A. Mocsy, and M. Strickland, "Quarkonium states in an anisotropic QCD plasma," *Phys.Rev.* **D79** (2009) 054019, `arXiv:0901.1998 [hep-ph]`.

[11] O. Kaczmarek, F. Karsch, F. Zantow, and P. Petreczky, "Static quark anti-quark free energy and the running coupling at finite temperature," *Phys.Rev.* **D70** (2004) 074505, `arXiv:hep-lat/0406036 [hep-lat]`.

[12] **WHOT-QCD** Collaboration, Y. Maezawa *et al.*, "Heavy-quark free energy, Debye mass, and spatial string tension at finite temperature in two flavor lattice QCD with Wilson quark action," *Phys.Rev.* **D75** (2007) 074501, `arXiv:hep-lat/0702004 [hep-lat]`.

[13] A. Mocsy and P. Petreczky, "Quarkonia correlators above deconfinement," *Phys.Rev.* **D73** (2006) 074007, `arXiv:hep-ph/0512156 [hep-ph]`.

[14] Z. Fodor, A. Jakovac, S. Katz, and K. Szabo, "Static quark free energies at finite temperature," *PoS* **LAT2007** (2007) 196, `arXiv:0710.4119 [hep-lat]`.

[15] P. Petreczky, C. Miao, and A. Mocsy, "Quarkonium spectral functions with complex potential," *Nucl.Phys.* **A855** (2011) 125–132, `arXiv:1012.4433 [hep-ph]`.

[16] A. Bazavov and P. Petreczky, "On static quark anti-quark potential at non-zero temperature," *Nucl.Phys.A904-905* **2013** (2013) 599c–602c, `arXiv:1210.6314 [hep-lat]`.

[17] A. Bazavov and P. Petreczky, "Static quark correlators and quarkonium properties at non-zero temperature," `arXiv:1211.5638 [hep-lat]`.

[18] O. Kaczmarek and F. Zantow, "Static quark anti-quark interactions in zero and finite temperature QCD. I. Heavy quark free energies, running coupling and quarkonium binding," *Phys.Rev.* **D71** (2005) 114510, `arXiv:hep-lat/0503017 [hep-lat]`.

[19] A. Rothkopf, T. Hatsuda, and S. Sasaki, "Proper heavy-quark potential from a spectral decomposition of the thermal Wilson loop," *PoS* **LAT2009** (2009) 162, `arXiv:0910.2321 [hep-lat]`.

[20] A. Rothkopf, T. Hatsuda, and S. Sasaki, "Complex Heavy-Quark Potential at Finite Temperature from Lattice QCD," *Phys.Rev.Lett.* **108** (2012) 162001, `arXiv:1108.1579 [hep-lat]`.

[21] Y. Burnier and A. Rothkopf, "Disentangling the timescales behind the non-perturbative heavy quark potential," *Phys.Rev.* **D86** (2012) 051503, `arXiv:1208.1899 [hep-ph]`.

[22] Y. Ikeda and H. Iida, "The anti-quark–quark potential from Bethe-Salpeter amplitudes on lattice," *PoS* **LATTICE2010** (2010) 143, `arXiv:1011.2866 [hep-lat]`.

[23] T. Kawanai and S. Sasaki, "Interquark potential with finite quark mass from lattice QCD," *Phys.Rev.Lett.* **107** (2011) 091601, `arXiv:1102.3246 [hep-lat]`.

[24] C. Allton, W. Evans, and J.-I. Skullerud, "Charmonium potentials at finite temperature," *PoS* **LATTICE2012** (2012) 082.

[25] W. Evans, C. Allton, and J. I. Skullerud, "Ab Initio Calculation of Finite Temperature Charmonium Potentials," *Phys.Rev.* **D89** (2014) 071502.

[26] W. Evans, C. Allton, P. Giudice, and J.-I. Skullerud, "Charmonium Potentials At Non-Zero Temperature," *PoS* **LATTICE2013** (2013) 168.

[27] C. Allton, G. Aarts, A. Amato, W. Evans, P. Giudice, *et al.*, "Quark-gluon plasma phenomenology from the lattice," *J.Phys.Conf.Ser.* **509** (2014) 012015.

[28] W. Evans, C. Allton, P. Giudice, and J.-I. Skullerud, "Charmonium Potentials At Non-Zero Temperature," *to be submitted to JHEP* (2014) .

[29] R. S. Chivukula, "The Origin of mass in QCD," *eConf* **C040802** (2004) L010, `arXiv:hep-ph/0411198 [hep-ph]`.

[30] D. J. Gross and F. Wilczek, "Ultraviolet Behavior of Non-Abelian Gauge Theories," *Physical Review Letters* **30** (June, 1973) 1343–1346.

[31] **Particle Data Group** Collaboration, J. Beringer *et al.*, "Review of Particle Physics (RPP)," *Phys.Rev.* **D86** (2012) 010001.

[32] M. Gell-Mann, "A Schematic Model of Baryons and Mesons," *Physics Letters* **8** no. 3, (February, 1964) 214–215.

[33] G. Zweig, "An SU(3) Model for Strong Interaction Symmetry and its Breaking I," *CERN Report 8182/TH.401.* (January, 1964) .

[34] G. Zweig, "An SU(3) Model for Strong Interaction Symmetry and its Breaking II," *CERN Report 8418/TH.412.* (February, 1964) .

[35] I. Y. Pomeranchuk *Doklady Akad. Nauk. SSSR* **78** (1951) 889.

[36] H. Satz, "Phase transitions in QCD," *Nucl.Phys.* **A681** (2001) 3–21, `arXiv:hep-ph/0007209 [hep-ph]`.

[37] O. Philipsen, "Lattice QCD at non-zero temperature and baryon density," `arXiv:1009.4089 [hep-lat]`.

[38] Y. Aoki, Z. Fodor, S. Katz, and K. Szabo, "The QCD transition temperature: Results with physical masses in the continuum limit," *Phys.Lett.* **B643** (2006) 46–54, `arXiv:hep-lat/0609068 [hep-lat]`.

[39] B. Svetitsky and L. G. Yaffe *Nucl.Phys.* **B210** **[FS6]** (1982) 423.

[40] H. Satz, "The States of Matter in QCD," `arXiv:0903.2778 [hep-ph]`.

[41] D. R. Pisarski and F. Wilczek *Phys. Rev.* **D29** (1984) 338.

[42] F. Karsch, E. Laermann, and C. Schmidt, "The Chiral critical point in three-flavor QCD," *Phys.Lett.* **B520** (2001) 41–49, `arXiv:hep-lat/0107020 [hep-lat]`.

[43] S. Gavin, A. Gocksch, and R. D. Pisarski, "QCD and the chiral critical point," *Phys.Rev.* **D49** (1994) 3079–3082, `arXiv:hep-ph/9311350 [hep-ph]`.

[44] T. Hatsuda, Y. Miake, and K. Yagi, *Quark-Gluon Plasma.* No. 23 in Cambridge Monographs on Particle Physics, Nuclear Physics and Cosmology. Cambridge University Press, December, 2005.

[45] J. Bardeen, L. N. Cooper, and J. R. Schrieffer, "Theory of superconductivity," *Phys. Rev.* **108** (Dec, 1957) 1175–1204.

[46] M. G. Alford, A. Schmitt, K. Rajagopal, and T. Schfer, "Color superconductivity in dense quark matter," *Rev.Mod.Phys.* **80** (2008) 1455–1515, `arXiv:0709.4635 [hep-ph]`.

[47] E. Eichten, K. Gottfried, T. Kinoshita, J. B. Kogut, K. Lane, *et al.*, "The Spectrum of Charmonium," *Phys.Rev.Lett.* **34** (1975) 369–372.

[48] E. Eichten, K. Gottfried, T. Kinoshita, K. Lane, and T.-M. Yan, "Charmonium: The Model," *Phys.Rev.* **D17** (1978) 3090.

[49] E. Eichten, K. Gottfried, T. Kinoshita, K. Lane, and T.-M. Yan, "Charmonium: Comparison with Experiment," *Phys.Rev.* **D21** (1980) 203.

[50] M. Shifman, A. Vainshtein, and V. Zakharov, "QCD and Resonance Physics," *Nucl. Phys.* **B147** (1979) 385; 448.

[51] P. Colangelo and A. Khodjamirian, "QCD sum rules, a modern perspective," `arXiv:hep-ph/0010175 [hep-ph]`.

[52] J. M. Maldacena, "The Large N limit of superconformal field theories and supergravity," *Adv.Theor.Math.Phys.* **2** (1998) 231–252, `arXiv:hep-th/9711200 [hep-th]`.

[53] S. Gubser, I. R. Klebanov, and A. M. Polyakov, "Gauge theory correlators from noncritical string theory," *Phys.Lett.* **B428** (1998) 105–114, `arXiv:hep-th/9802109 [hep-th]`.

[54] E. Witten, "Anti-de Sitter space and holography," *Adv.Theor.Math.Phys.* **2** (1998) 253–291, `arXiv:hep-th/9802150 [hep-th]`.

[55] O. Aharony, S. S. Gubser, J. M. Maldacena, H. Ooguri, and Y. Oz, "Large N field theories, string theory and gravity," *Phys.Rept.* **323** (2000) 183–386, `arXiv:hep-th/9905111 [hep-th]`.

[56] O. Aharony, J. Marsano, S. Minwalla, K. Papadodimas, and M. Van Raamsdonk, "The Hagedorn - deconfinement phase transition in weakly coupled large N gauge theories," *Adv.Theor.Math.Phys.* **8** (2004) 603–696, `arXiv:hep-th/0310285 [hep-th]`.

[57] E. Witten, "Anti-de Sitter space, thermal phase transition, and confinement in gauge theories," *Adv.Theor.Math.Phys.* **2** (1998) 505–532, `arXiv:hep-th/9803131 [hep-th]`.

[58] G. Aarts, F. A. James, J. M. Pawlowski, E. Seiler, D. Sexty, *et al.*, "Stability of complex Langevin dynamics in effective models," *JHEP* **1303** (2013) 073, `arXiv:1212.5231 [hep-lat]`.

[59] G. Aarts and F. A. James, "Complex Langevin dynamics in the SU(3) spin model at nonzero chemical potential revisited," *JHEP* **1201** (2012) 118, `arXiv:1112.4655 [hep-lat]`.

[60] G. Aarts, F. A. James, E. Seiler, and I.-O. Stamatescu, "Complex Langevin: Etiology and Diagnostics of its Main Problem," *Eur.Phys.J.* **C71** (2011) 1756, `arXiv:1101.3270 [hep-lat]`.

[61] **AuroraScience** Collaboration, M. Cristoforetti, F. Di Renzo, and L. Scorzato, "New approach to the sign problem in quantum field theories: High density QCD on a Lefschetz thimble," *Phys.Rev.* **D86** (2012) 074506, `arXiv:1205.3996 [hep-lat]`.

[62] **ALICE** Collaboration, B. Abelev *et al.*, "Centrality determination of Pb-Pb collisions at $\sqrt{s_{NN}} = 2.76$ TeV with ALICE," *Phys.Rev.* **C88** no. 4, (2013) 044909, `arXiv:1301.4361 [nucl-ex]`.

[63] **NA38** Collaboration, C. Baglin et al. *Phys. Lett.* **B220** (1989) 471.

[64] H. Satz, "The SPS heavy ion programme," *Phys.Rept.* **403-404** (2004) 33–50, `arXiv:hep-ph/0405051 [hep-ph]`.

[65] **NA50** Collaboration, M. Abreu *et al.*, "Evidence for deconfinement of quarks and gluons from the J/ψ suppression pattern measured in Pb + Pb collisions at the CERN SPS," *Phys.Lett.* **B477** (2000) 28–36.

[66] **STAR** Collaboration, J. Adams *et al.*, "Experimental and theoretical challenges in the search for the quark gluon plasma: The STAR Collaboration's critical assessment of the evidence from RHIC collisions," *Nucl.Phys.* **A757** (2005) 102–183, `arXiv:nucl-ex/0501009 [nucl-ex]`.

[67] **PHENIX** Collaboration, K. Adcox *et al.*, "Formation of dense partonic matter in relativistic nucleus-nucleus collisions at RHIC: Experimental evaluation by the PHENIX collaboration," *Nucl.Phys.* **A757** (2005) 184–283, `arXiv:nucl-ex/0410003 [nucl-ex]`.

[68] I. Arsene, I. Bearden, *et al.*, "Quark-gluon plasma and color glass condensate at RHIC. The perspective from the BRAHMS experiment," *Nuclear Physics A* **757** no. 1-2, (2005) 1–27.

[69] B. Back, M. Baker, *et al.*, "The PHOBOS perspective on discoveries at RHIC," *Nuclear Physics A* **757** no. 1-2, (2005) 28–101.

[70] **ALICE** Collaboration, B. Abelev *et al.*, "J/ψ Suppresion at forward rapidity in Pb-Pb collisions at $\sqrt{s_{NN}} = 2.76$ TeV," *Phys. Rev. Lett.* **109** (Aug, 2012) 072301.

[71] **ALICE** Collaboration, K. Aamodt *et al.*, "Charged-particle multiplicity density at mid-rapidity in central Pb-Pb collisions at $\sqrt{s_{NN}} = 2.76$TeV," *Phys. Rev. Lett.* **105** (Dec, 2010) 252301.

[72] **ALICE** Collaboration, K. Aamodt and others., "Elliptic flow of charged particles in Pb-Pb collisions at $\sqrt{s_{NN}} = 2.76$TeV," *Phys. Rev. Lett.* **105** (Dec, 2010) 252302.

[73] **ALICE** Collaboration, K. Aamodt *et al.*, "Centrality dependence of the charged-particle multiplicity density at mid-rapidity in Pb-Pb collisions at $\sqrt{s_{NN}} = 2.76$TeV," *Phys. Rev. Lett.* **106** (Jan, 2011) 032301.

[74] **ALICE** Collaboration, K. Aamodt *et al.*, "Suppression of charged particle production at large transverse momentum in central Pb-Pb collisions at $\sqrt{s_{NN}} = 2.76$TeV," *Physics Letters B* **696** no. 1-2, (2011) 30–39.

[75] **ALICE** Collaboration, B. B. Abelev *et al.*, "Centrality, rapidity and transverse momentum dependence of J/ψ suppression in Pb-Pb collisions at $\sqrt{s_{NN}}$=2.76 TeV," *Phys.Lett.* **743** (2014) 314–327, `arXiv:1311.0214 [nucl-ex]`.

[76] **ALICE** Collaboration, B. Abelev *et al.*, "Measurement of charged jet suppression in Pb-Pb collisions at $\sqrt{s_{NN}} = 2.76$ TeV," *JHEP* **1403** (2014) 013, `arXiv:1311.0633 [nucl-ex]`.

[77] **ATLAS** Collaboration, A. Angerami, "Measurements of jet quenching and heavy flavor production with the ATLAS detector," *Nucl.Phys.* **A910-911** (2013) 12–19, `arXiv:1210.0138 [nucl-ex]`.

[78] **CMS** Collaboration, T. Dahms, "Upsilon suppression in Pb-Pb collisions at the LHC," `arXiv:1307.1795 [nucl-ex]`.

[79] C. Gattringer and C. Lang, *Quantum Chromodynamics on the Lattice - An Introductory Presentation.* Springer, 2010.

[80] K. G. Wilson, "Confinement of Quarks," *Phys. Rev. D* **10** (1974) 2445.

[81] **Hadron Spectrum** Collaboration, L. Liu *et al.*, "Excited and exotic charmonium spectroscopy from lattice QCD," *JHEP* **1207** (2012) 126, `arXiv:1204.5425 [hep-ph]`.

[82] **Fermilab Lattice, MILC, HPQCD** Collaboration, A. Kronfeld *et al.*, "Predictions from lattice QCD," *Int.J.Mod.Phys.* **A21** (2006) 713–719, `arXiv:hep-lat/0509169 [hep-lat]`.

[83] M. Clark, "The Rational Hybrid Monte Carlo Algorithm," *PoS* **LAT2006** (2006) 004, `arXiv:hep-lat/0610048 [hep-lat]`.

[84] C. Allton, "Gauge-invariant smearing and matrix correlators using Wilson fermins at β=6.2," *Physical Review D* **47** no. 11, (1993) 5128.

[85] S. Basak, I. Sato, S. Wallace, R. Edwards, D. Richards, *et al.*, "Combining quark and link smearing to improve extended baryon operators," *PoS* **LAT2005** (2006) 076, `arXiv:hep-lat/0509179 [hep-lat]`.

[86] C. Morningstar and M. J. Peardon, "Analytic smearing of SU(3) link variables in lattice QCD," *Phys.Rev.* **D69** (2004) 054501, `arXiv:hep-lat/0311018 [hep-lat]`.

[87] **APE** Collaboration, M. Albanese *et al. Phys. Lett.* **B192** (1987) 142.

[88] F. Knechtli and A. Hasenfratz, "Dynamical fermions with fat links," *Phys.Rev.* **D63** (2001) 114502, `arXiv:hep-lat/0012022 [hep-lat]`.

[89] A. Bazavov, T. Bhattacharya, M. Cheng, C. DeTar, H. Ding, *et al.*, "The chiral and deconfinement aspects of the QCD transition," *Phys.Rev.* **D85** (2012) 054503, `arXiv:1111.1710 [hep-lat]`.

[90] **Wuppertal-Budapest** Collaboration, S. Borsanyi *et al.*, "Is there still any T_C mystery in lattice QCD? Results with physical masses in the continuum limit III," *JHEP* **1009** (2010) 073, `arXiv:1005.3508 [hep-lat]`.

[91] C. Michael *Nucl. Phys.* **B259** (1985) 58.

[92] M. Lusher and U. Wolff. *Nucl. Phys.* **B339** (1990) 222.

[93] H. A. Bethe and E. E. Salpeter, "A Relativistic Equation for Bound State Problems," *Phys.Rev.* **84** (1951) 1232–1242.

[94] V. Sauli and P. Bicudo, "Excited charmonium states from Bethe-Salpeter equation," *PoS* **QCD-TNT-II** (2011) 043, `arXiv:1112.5540 [hep-ph]`.

[95] V. Sauli, "Intriguing solutions of Bethe-Salpeter equation for radially excited pseudoscalar charmonia," `arXiv:1207.2621 [hep-ph]`.

[96] Y. Ikeda and H. Iida, "Quark-anti-quark potentials from Nambu-Bethe-Salpeter amplitudes on lattice," *Prog.Theor.Phys.* **128** (2012) 941–954, `arXiv:1102.2097 [hep-lat]`.

[97] **UKQCD** Collaboration, P. Lacock, C. Michael, P. Boyle, and P. Rowland, "Orbitally excited and hybrid mesons from the lattice," *Phys.Rev.* **D54** (1996) 6997–7009, `arXiv:hep-lat/9605025 [hep-lat]`.

[98] X. Liao and T. Manke, "Excited charmonium spectrum from anisotropic lattices," `arXiv:hep-lat/0210030 [hep-lat]`.

[99] **HAL QCD** Collaboration, S. Aoki, "Hadron interactions in lattice QCD," *Prog.Part.Nucl.Phys.* **66** (2011) 687–726, `arXiv:1107.1284 [hep-lat]`.

[100] C. Morningstar and M. J. Peardon, "The glueball spectrum from novel improved actions," *Nucl.Phys.Proc.Suppl.* **83** (2000) 887–889, `arXiv:hep-lat/9911003v1`.

[101] **TrinLat** Collaboration, J. Foley, A. O'Cais, M. Peardon, and S. M. Ryan, "A Non-perturbative study of the action parameters for anisotropic-lattice quarks," *Phys.Rev.* **D73** (2006) 014514, `arXiv:hep-lat/0405030 [hep-lat]`.

[102] R. Morrin, A. O. Cais, M. Peardon, S. M. Ryan, and J.-I. Skullerud, "Dynamical QCD simulations on anisotropic lattices," *Phys.Rev.* **D74** (2006) 014505, `arXiv:hep-lat/0604021 [hep-lat]`.

[103] M. B. Oktay and J.-I. Skullerud, "Momentum-dependence of charmonium spectral functions from lattice QCD," `arXiv:1005.1209 [hep-lat]`.

[104] G. Aarts, C. Allton, M. B. Oktay, M. Peardon, and J.-I. Skullerud, "Charmonium at high temperature in two-flavor QCD," *Phys.Rev.* **D76** (2007) 094513, `arXiv:0705.2198 [hep-lat]`.

[105] **SciDAC, LHPC, UKQCD** Collaboration, R. G. Edwards and B. Joo, "The Chroma software system for lattice QCD," *Nucl.Phys.Proc.Suppl.* **140** (2005) 832, `arXiv:hep-lat/0409003 [hep-lat]`.

[106] CERN, "Program library," 2014. `http://cernlib.web.cern.ch/cernlib/`. [Online; accessed 23-July-2014].

[107] W. H. Press, S. A. Teukolsky, W. T. Vetterling, and B. P. Flannery, *Numerical Recipes in FORTRAN; The Art of Scientific Computing.* Cambridge University Press, New York, NY, USA, 2nd ed., 1993.

[108] **HAL QCD** Collaboration, N. Ishii, "Time-dependent effective Schroedinger-like equation for lattice nuclear potentials," *PoS* **LATTICE2011** (2011) 160.

[109] S. Durr, "Physics of η' with rooted staggered quarks," *Phys.Rev.* **D85** (2012) 114503, `arXiv:1203.2560 [hep-lat]`.

[110] S. Aoki, 2012. Private Communication.

[111] R. G. Edwards, B. Joo, and H.-W. Lin, "Tuning for Three-flavors of Anisotropic Clover Fermions with Stout-link Smearing," *Phys. Rev.* **D78** (2008) 054501, `arXiv:hep-lat/0803.3960`.

[112] K. Symanzik, "Continuum Limit and Improved Action in Lattice Theories. 1. Principles and ϕ^4 Theory," *Nucl.Phys.* **B226** (1983) 187.

[113] K. Symanzik, "Continuum Limit and Improved Action in Lattice Theories. 2. O(N) Nonlinear Sigma Model in Perturbation Theory," *Nucl.Phys.* **B226** (1983) 205.

[114] R. Hudspith, "Fourier Accelerated Conjugate Gradient Lattice Gauge Fixing," `arXiv:1405.5812 [hep-lat]`.

[115] O. Kaczmarek, "Screening at finite temperature and density," *PoS* **CPOD07** (2007) 043, `arXiv:0710.0498 [hep-lat]`.